Light-Activated Biomaterials for Soft Tissue Sealing and Wound Repair

by

Deepanjan Ghosh

A Dissertation Presented in Partial Fulfillment
of the Requirements for the Degree
Doctor of Philosophy

Approved November 2021 by the
Graduate Supervisory Committee:

Kaushal Rege, Chair
Abhinav Acharya
Julianne Holloway
David DiCaudo
Kai P. Leung

ARIZONA STATE UNIVERSITY

December 2021

ABSTRACT

Sutures, staples, and tissue glues remain the primary means of tissue approximation and vessel ligation. Laser-activated tissue sealing is an alternative approach that conventionally employs light-absorbing chromophores and nanoparticles for converting near-infrared (NIR) laser to heat. The local increase in temperature engenders interdigitation of sealant and tissue biomolecules, resulting in rapid tissue sealing. Light-activated sealants (LASE) were developed in which indocyanine green (ICG) dye is embedded within a biopolymer matrix (silk or chitosan) for incisional defect repair. Light-activated tissue-integrating sutures (LATIS) that synergize the benefits of conventional suturing and laser sealing were also fabricated and demonstrated higher efficacies for tissue biomechanical recovery and repair in a full-thickness, dorsal surgical incision model in mice compared to commercial sutures and cyanoacrylate skin glue. Localized delivery of modulators of tissue repair, including histamine and copper, from LASE and LATIS further improved healed skin strength. In addition to incisional wounds, histamine co-delivered with silk fibroin LASE films accelerated the closure of full thickness, splinted excisional wounds in immunocompetent BALB/c mice and genetically obese and diabetic db/db mice, resulting in faster closure than Tegaderm wound dressing. Immunohistochemistry analyses showed LASE-histamine treatment enhanced wound repair involving mechanisms of neoangiogenesis, myofibroblast activation, transient epidermal EMT, and also improve healed skin biomechanical strength which are hallmarks of improved healing outcomes. Benefit of temporal delivery was further investigated of a second therapeutic (growth factor nanoparticles) in modulating wound healing outcomes in both acute and diabetic wounds. The hypothesis of temporal delivery of second therapeutic around the ‘transition period’ in wounds further improved wound closure kinetics and biomechanical recovery of skin strength. Laser sealing and approximation, together with delivery of immunomodulatory mediators, can lead to faster healing and tissue repair, thus reducing wound dehiscence, preventing wounds moving towards chronicity and lowering incidence of surgical site infections, all of which can have significant impact in the clinic.

DEDICATION

I dedicate this thesis to Baba and Maa (my parents). I hope this achievement will fulfill the dreams you had many years ago when you chose to give me the best education you could

and

To Stuti, four years in distance and this year together, your continuous support and keep me going

ACKNOWLEDGEMENTS

First, and most importantly, I would like to acknowledge and thank my advisor and committee chair, Dr. Kaushal Rege, for his guidance and mentoring he provided thorough my graduate studies. His supportive approach and patience during the highs and the lows of research has helped instilled the confidence in me to successfully plan and execute studies. Our conversations regarding research, career opportunities ahead, and navigating life during this journey has been always thought-provoking and helped shape my perspective. I am confident he will continue to be my support system beyond this journey.

I would also like to acknowledge my dissertation committee, Dr. Abhinav Acharya, Dr. Julianne Holloway, Dr. David DiCaudo, and Dr. Kai P. Leung, for their guidance in successful completion of my dissertation.

I would like to give a special thanks to Dr. Russell Urie for his mentorship and guidance during the formative period of my graduate studies. My understanding of experimental design and statistical tests and its interpretation would not have been complete without the daily discussions with Dr. Jordan Yaron. His treasured support has been really influential in shaping my research and critiquing my results. GraphPad, FIJI/ImageJ, various biochemical analyses, the list is long.

I am very lucky to have had the support of Jacquelyn Kilbourne, Dr. Juliane Daggett-Vondras, Kenneth Lowe, and Dr. Dale DeNardo at Department of Animal Care and Technologies (DACT) available to me during my dissertation work. Their exemplary technical support and guidance with animal studies helped me in advancing my research. All other support staff at DACT, especially Randall Dalbey assisted with all needs thorough the duration of these studies.

I want to acknowledge the excellent students whom I have had the pleasure of mentoring, Victoria Tai, Michael Bejarano, and Shraddha Patil. Their excellent attitudes and skilled bench hands was the highlight of my mentoring experience and teamwork. Thanks to Fulton Undergraduate Research Initiative and other funding initiatives, I had the opportunity to mentor and

work with several stellar undergraduate students, including Andy Chang, Yvonne Chook, Michelle Tieu, Calvin Nguyen, Antara Sira, and May Nguyen.

During the course of my dissertation work, the former and current members of Rege Bioengineering Lab, Dr. Sudhakar Godeshala, Dr. Sheba Goklany, Dr. Karthik Pushpavanam, Rajesh Nitiyanandan, Sahil Inamdar, Inam Ridha, Subhadeep Dutta, and Harini Muralikrishnan were always around to answer my questions and gain helpful insights about this journey. Newer lab members, Dr. Raisul Abedin and Shubham Pallod also enriched my experience within few days of us working together. I consider each of them as my good friends and also my peers.

I also had the opportunity to collaborate with Prof. Russell Witte and Chris Salinas at University of Arizona, and Prof. Francois Berthiaume and Dr. Sunil Kumar at Rutgers University. Their expertise, helpful discussions, and support were a highlight of collaborative research.

I could not have succeeded without the support of the administration of the Biological Design Graduate Program: Dr. Antony Garcia and Laura Hawes when the program was under School of Biological and Health System Engineering (SBHSE) and at present Dr. Kaushal Rege and Tiffany Wingerson from School for Engineering of Matter, Transport, and Energy (SEMTE).

There are many employees that I would like to thank as well for their dedicated support, with day-to-day administrative support, procurement services, education and travel grant applications. I would like thank Jarrett Johnson, Shannon Pete, Miriah M. Kleijn, and Robert Booher from SEMTE for their continuous support. The continuous availability of Fred Pena and Philip Schultz for troubleshooting any research related equipment and methods guaranteed a seamless research experience.

Lastly, I want to thank my family for their support and encouragement.

TABLE OF CONTENTS

Page

APPENDIX

LIST OF FIGURES

Figure Page

Figure Page

LIST OF TABLES

Chapter 1: INTRODUCTION

1.1 TRAUMATIC WOUNDS

Skin injuries caused by surgical incisions or traumatic lacerations compromise skin's structural and protective integrity which possess risk of infections. Annually, more than fifty million surgical procedures are performed in the United States alone which results in need to incision closure and wound closure(Hall et al., 2017). In clinic, sutures and stapes remain the *go-to* and gold-standard method for wound closure. The global market value of traumatic wound care products comprising of sutures, staples and clips is projected to cross US $15 billion by 2024(Taboada et al., 2020). Additionally, the share of tissue adhesives and sealants are also increasing at a compound annual growth rate of 9.7%. The market size reported for 2020 was estimated to be US $2.7 billion and the projected revenue in 2025 is US $4.5 billion(Gallo et al., 2016; Taboada et al., 2020).

1.2. INCISIONAL WOUND MANAGEMENT

1.2.1. Mechanism of repair

In clinic surgical incisions or traumatic lacerations are treated by physically approximating the skin edges with an aim to physically connect the skin edges, prevent bleeding, obtain a fluid-tight barrier with an aim to restore the compromised skin barrier and obtain a functional and esthetic scar(Johal & Kreder, 2018; Singer et al., 1997). The process of wound healing starts immediately after the tissue sustains injury and the wound edges being approximated together. A direct relation was reported between the time of injury and closure of the laceration to minimize risk of infections, but the length of this "golden period" between injury and wound closure varies depending on the condition of the wound. For relatively clean wounds, the "golden period" was 19 hours between injury and closure for wounds to heal, beyond this window significant differences in healing

outcomes were observed. But for high risk wounds such as contaminated wounds, wound in poorly vascularized areas, wounds in immunocompromised patients, etc. should be ideally closed within 6 hour (Berk et al., 1988; Singer et al., 1997).

Since no significant amount of tissue is lost during surgical incisions or traumatic lacerations, repair of the injury occurs via primary intention. The primary intention repair process is prompt and re-epithelialization of the defect is achieved within 7-10 days. Hence, an ideal wound closure device meant for incisional repair should be resorbed within this time period or be physically removed from the wound site following achieving satisfactory healing. In instances where the wound is contaminated or infected, the wound edges are not approximated for healing immediately. The wound is left open, and the infection or contamination is first mitigated, and any viable tissue is removed further in the process. Once a clean wound can be achieved, then the wounded edges are approximated together for healing. This method of treatment and healing is referred to as healing by tertiary intention or delayed primary intention(Beldon, 2010).

1.2.2. Current wound closure devices

1.2.2.1. Sutures

Sutures are the most common method of surgical incisions and traumatic laceration closure. The choice of suture material can either be nonabsorbable or absorbable depending on the depth of the injury and also the intended function(Tajirian & Goldberg, 2010). Nonabsorbable suture materials like nylon, polypropylene, polyester, silk retain their tensile strength for ~45 – 60 days, provide good handling and knot security are primarily used for closing superficial lacerations where only the outer layer or epidermis is breached. Whereas absorbable sutures like polyglactin, polyglycolic acid, polydioxanone, chromic gut, etc. are used for closure deeper wounds involving subcuticular tissues(Campbell & Marks, 1985; Ratner et al., 1994). In case of multilayered sutures and deep sutures, absorbable sutures are preferred to decrease dead space and improve cosmetic outcomes of wounds. Although given the benefits of suturing, suture as a choice of wound closure

materials should be avoid in contaminated wounds as they can further wick bacteria at the wound site and also be avoided for approximating fat layers as they do not hold tension(Grimes & Hunt, 1993; Milewski & Thomson, 1980).

1.2.2.2. Staples and clips

Staple and clips were developed as an alternative closure device to sutures provides more uniform approximation and faster application compared to sutures(George & Simpson, 1985). Staples have reported lower rate of foreign body reaction and occurrence of infections compared to sutures. Staples are particularly the choice of closure for wounds in the areas of scalp, trunk, and extremities. In a controlled trial it was reported that staples can close 22.5 cm wound length per minute compared to 4.2 cm length per minute with sutures. On an average for a wound of 15-cm length, stapling saved up to ~3 minutes in wound closure time compared to suturing the incision(Gatt et al., 1985). Also, for the same length of wound closure, staples do cost slightly more than suture, but the speed and convenience associated with staples outweigh the additional cost associated with it. Although staples have quicker application times, pain associated with application and cosmetic outcomes are similar to that of sutures(Harvey & Logan, 1986). In a recent report comparing stapling vs suturing for skin closure following total knee arthroplasty, staples required lower wound closure times and showed lower complications following wound closure(Kim et al., 2017).

1.2.2.3. Tissue adhesives - Sealant and Glues

Following the revolutionary advancements of medical technologies in the past three decades, various bioadhesive have been developed for tissue sealing applications. Contrary to sutures and staples/clips where skin closure method depends on mechanical approximation of tissues, skin closure using tissue adhesives is obtained via chemical or biological crosslinking between the tissue and adhesive. Tissue adhesives allow wound closure without the need for further trauma or stress to the injured tissue as in case of sutures and staples. Tissue adhesives based on their

target tissue of application can either be classified as external adhesives (topical adhesives for skin wound closure, epidermal grafting, etc.) and internal adhesives (anastomoses of blood vessels, nerves, and gastrointestinal tract, dural sealing, hernia repair, etc.).

An ideal skin adhesive should have the following characteristics: (i) adhere rapidly to the tissue surface (ii) conform to the defect shape (iii) resist deformation from external mechanical stress (iv) preferably be bioresorbable (v) not invoke immune response or toxicity(Narayanan et al., 2020). Based on the composition of tissue adhesives they can be broadly classified into either biological adhesive such as fibrin sealants, bovine serum albumin-based sealants, etc. or synthetic adhesive such as cyanoacrylate glues, polyurethane based glues, etc. The various tissue adhesives for skin sealing which are either FDA-approved or under clinical trial at the time of writing are summarized in Table 1-1.

Table 1-1. List of FDA-approved or under clinical trial adhesives for skin defect repair

Name	Approval Year	Composition	Target tissue	Indication for use
Dermabond Ethicon Inc.	1998	2-Octyl cyanoacrylate	Skin closure	Topical application for skin closure of approximated skin edges from surgical incisions
Indermil Covidien LP	2002	n-Butyl-2-cyanoacrylate	Skin closure	Topical application for skin closure of laparoscopic and trauma-induced incisions
Histoacryl, Histoacryl Blue Tissue Seal LLC	2007	n-Butyl-2-cyanoacrylate	Skin closure	Topical application for skin closure in minimal-tension wounds
SurgiSeal Adhezion Biomedical	2009	2-Octyl cyanoacrylate (OctylFlex® Technology)	Skin closure	Topical application to close easily approximated skin from surgical incisions, lacerations and minimally invasive surgeries. Not a replacement for deep dermal sutures
Derma+Flex QS Clemence Medical Products	2010	2-Octyl cyanoacrylate	Skin closure	Topical application for skin closure in surgical incisions and trauma-induced lacerations. Use along with sutures but not

BondEase OptMed Inc.	2016	Methylidene malonate	Skin closure	as replacement for deep dermal sutures Topical application for skin closure in case of low tension and easily approximated wounds
Mar-CUTIS (Flix) Adhesys Medical GmbH	Undergoing clinical trial	Polyurethane	Skin closure	Topical application for approximation of skin approximation in conjugation with deep dermal sutures

Although sutures and staples and clips are the gold standard in clinic for repair of surgical incisions and traumatic lacerations for decades, these wound approximation and closure methods have a few limitations. Tissue adhesives and glues are recent additions to the wound closure devices either for use alone or in conjugation with sutures, they still have challenges which deter their adoption as suture replacements in the clinic. The positives and negatives of every skin incisional wound closure device is summarized in Table 1-2.

Table 1-2. Pros and cons of conventionally used wound closure devices for skin defect repair

Closure Device	Positives
Sutures and Staples	Excellent tissue approximation achieved Withstand mechanical loads which can reduce risk of wound dehiscence
Tissue adhesives: Sealants and Glues	Rapid polymerization in case of cyanoacrylate-based adhesives. Cyanoacrylate-based adhesives can achieve adhesive forces to keep wounds approximated under intrinsic and extrinsic forces Ease of use, Lower costs and infection rates
Closure Device	**Negatives**
Sutures and Staples	Suturing can be time consuming process in certain applications. Can result in bacterial wicking increasing risk of infections

	Suturing and staples further increases trauma to already damaged wound edges
	Post-operative removal of non-resorbable sutures and staples in case of skin wound applications
Tissue adhesives: Sealants and glues	Brittle nature of the adhesive post polymerization limits usage in small incisional wounds
	Exothermic polymerization with tissue surface, toxicity issue with degrading monomers (cyanoacetate, formaldehyde, etc.)
	Fail to match properties of the target tissue (viscoelastic properties) which can cause failure during high load-bearing applications
	Adhesion depends on interaction between sealant and tissue surface molecules or functional groups – this interaction can be compromised by tissue fouling by blood or other body fluids
	Degradation or biosorption timeline may not match target tissue healing timeline

1.2.2.4. Light-activated tissue sealing

Using light as modality for sealing tissues was first reported in 1979 for sealing of small blood in rats using a Neodymium-YAG laser as the source of light (Jain & Gorisch, 1979). The process of using laser energy to join or bond tissues was termed as laser tissue welding. Besides using different laser parameters and target tissues to evaluate laser tissue welding as a viable alternative method of tissue closure, several studies were being performed to understand the mechanism involved in laser tissue welding. The first study reported loosening of collagen triple helix and interaction between individual collagen bands in rat carotid arteries after Nd:YAG irradiation leading to collagen “bonding” which was responsible for laser welding (Schober et al., 1986). This observation was supported by another study looking into fusion of vein segments following argon laser welding where collagen-to-collagen and collagen-to-elastin bonding provides initial tensile strength following welding (White et al., 1988). The process of light-activated tissue sealing can be broadly classified into two approaches: (i) photochemical tissue bonding where a photosensitive dye like Rose Bengal, Riboflavin-5-Phosphate, etc. is applied to wound edges and exposed to light to induce covalent bonds between proteins at the surface of the tissue and (ii) photothermal tissue

bonding when a sealant material with a photosensitive dye like Indocyanine Green (ICG), methylene blue, fluorescein green, etc. absorbs the laser to produce a photothermal effect which then causes fusion of tissue collagenous protein at the wound site resulting in a robust “weld” between the incised sections(Al-Mubarak & Al-Haddab, 2013; Alvarez-López & Aguirre-Soto, 2021; Ark et al., 2016; Xu et al., 2015).

The first insight into mechanism of thermal tissue welding was obtained by heating of rat carotid artery using Nd:YAG laser and then evaluate electron micrographs of the irradiated collagen. Loosening of collagen triple helix and interaction between individual collagen strands or “bonding” was observed(Schober et al., 1986). Although significant number of studies over the past ~30 years have shown the efficacy of laser tissue sealing for sealing of skin, nerve, blood vessels, etc. but their translation into clinics has been limited due to data on thermal damage to the surrounding tissue(Li et al., 2020; Sriramoju & Alfano, 2011).

A recent report investigating effect of temperature on tissue sealing outcomes employing *ex vivo* porcine skin, bovine serum albumin as solder, and Nd: YAG laser observed highest welding strength of tissue was obtained at 55 °C and when welding was performed at elevated temperatures of 65 °C led to denaturation of tissue protein and impacting tensile strength negatively(Li & Wang, 2021).

Table 1-3. Pros and cons of light-activated sealing method for skin defect repair

Closure Device	Positives
Laser tissue sealing	Scope for tissue alignment and minimize tissue handling
	Needle-free approach resulting in no additional trauma during closure
	Rapid and immediate fluid-tight sealing obtained
	Improved re-epithelialization and healed skin strength obtained in the early phases of wound healing
	Minimized foreign body reaction and no follow-up needed for sealant removal
	Improved cosmetic outcomes and reduced hospital stays reducing costs in certain instances

Closure Device	Negatives
Laser tissue sealing	Better suited for small to medium sized wounds
	Excessive temperatures can negatively impact tissue repair and increase chances of thermal damage to surrounding tissue
	Limited availability and cost of equipment for routine use in clinic

1.3 UNMET NEEDS AND DESIGN CONSIDERATIONS

An in-depth understanding of tissue-specific properties is crucial for effective design of tissue adhesives with a potential for translation and addressing some of the concerns of the current approved tissue adhesives. Also, a one-size fits-all approach further complicates the design and use of tissue adhesives and is a major reason for failure of many promising tissue adhesives receiving approval for clinical use. In this section, I will focus primarily on tissue adhesives intended for skin wound closure use.

1. Skin sealants which not only focus on keeping skin edges approximated thorough the natural healing process but can be multifunctionalized by loading and delivery of bioactives that can modulate the wound microenvironment to promote tissue repair.
2. Skin tissue sealants which can match the mechanical and viscoelastic properties of the skin (example: elastic modulus of epidermis is 300 kPa). This consideration is critical to design skin sealants which are flexible, minimize delamination from defect area under mechanical loading and external stress, and conform the defect shape appropriately.
3. Physiochemical environment of the wound area is another important factor for designing effective sealants that will not impede the natural healing process. The pH of skin and subcutaneous tissue is in the range pH 4-6 and pH 6.7-7.1, respectively. This environment

can alter efficacy of sealants which rely on chemical reaction or polymerization for tissue sealing. Also, any degradation products from the sealant materials should ideally be non-toxic and not influence the intrinsic physiochemical properties of the healing area.

4. Combination of other successful approaches (negative pressure wound therapy, mechanical offloading of stress at the wound site, etc.) can be beneficial for long term healing outcomes like healed wound strength, improved tissue remodeling, reduced scarring, etc.

1.4 THESIS CONTRIBUTION

This dissertation evaluates various biomaterials, fabrication, and their design parameters for use as light-activated sealants for defect repair in soft tissues with a focus on improving healing outcomes. The primary contributions of this dissertation to the field of tissue adhesives for wound closure are:

1. Evaluation of biophysical (transepidermal water loss), biomechanical (tensile strength), structural (ultrasound and photoacoustic imaging), and histological parameters at intermediate timepoints during the course of healing to further assess healing in comparison to suturing.
2. Combining topical delivery of a bioactive (exogenous histamine) along with light-activated sealants (LASE) sealing to further enhance tensile strength of healing skin at earlier timepoints which could minimize risk of wound dehiscence.
3. The first fabrication of light-activated tissue integrating sutures (LATIS) synergizing the benefits of conventional suturing and light-activated tissue sealing and evaluate its efficacy in sealing skin incisional wounds.
4. Fabrication of second generation LATIS with ionic copper in lieu of gold nanorods with an aim for multi-functionality – absorb NIR laser and also act as a bioactive to modulate wound healing.

5. Evaluate the efficacy of silk fibroin-LASE along with a bioactive (exogenous histamine) for repair of full-thickness excisional wounds in acute and diabetic wound models in mice.
6. Elucidating mechanism of accelerated healing with the combination of silk fibroin and histamine involving neoangiogenesis, myofibroblast activation, transient epidermal EMT.
7. The identification of importance of temporal delivery while delivering multiple therapeutics for tissue repair. Temporal delivery of different bioactives to target different phases of healing can maximize the benefits of individual bioactives and minimize the need for higher or multiple dosage.
8. Additional development: Fabrication, testing design parameters, and screening adhesive behavior according to ASTM standards under simulated in vivo conditions of modified chitosan LASE as reinforcement devices to minimize anastomotic leakages following colorectal surgical procedures.

CHAPTER 2: LIGHT ACTIVATED SEALANTS(LASE)FOR INCISIONAL WOUND SEALING AND REPAIR VISUALIZATION AND CHARACTERIZATION OF LASE-TISSUE INTERFACE

2.1 INTRODUCTION AND BACKGROUND

Our group have previously reported the fabrication and use of light-activated sealants (LASE) for repair of murine skin incisional wounds. The LASE system comprises of three components: (i) a polymer matrix likely elastin-like polypeptides (ELP), collagen, or silk fibroin which acts as a scaffold for aiding repair (ii) a chromophore likely gold nanorods (GNRs) or FDA approved Indocyanine (ICG) dye for conversion of laser light to photothermal energy, and (iii) a hand-held near-infrared (NIR) laser tuned to 808nm. Laser irradiation of the LASE-tissue interface and the resultant photothermal response engenders interdigitation of LASE and tissue biomolecules, resulting in rapid tissue sealing. LASE has resulted in improved biomechanical skin properties in the earlier stages of healing compared to conventional sutures and skin glues(Urie, Guo, et al., 2018b; R. Urie et al., 2015). LASE also gives a scope for multifunctionality and loading of LASE with vancomycin helped in combating MRSA-induced surgical site infection in murine wounds while enhancing tissue repair(Urie et al., 2021).

In this study we probe various hallmarks of a healing wound using biophysical, biomechanical, imaging and histological techniques at intermediate timepoints during the course of healing to further elucidate how LASE enhances healing outcomes compared to conventional suturing of incisional wounds. Biophysical and biomechanical studies consist of transepidermal water loss (TEWL) levels and healed skin strength recovery, respectively. To better understand the wound bed and the LASE-tissue interface during healing, ultrasound and photoacoustic imaging was performed along with histological evaluation of the newly deposited tissue. Here, we report improved skin barrier function recovery and healed skin tensile strength compared to conventional suturing at early timepoint (day 2 post-wounding). Late into the healing period (Day 7 post-

wounding) no difference in TEWL levels or healed skin tensile strength was observed between the LASE and suture closed incisions. We also deliver histamine, a bioactive which has shown efficacy in skin wound healing along with LASE to evaluate the enhanced wound healing outcomes(Boyd & Smith, 1959; Dabrowski et al., 1975; Numata et al., 2006). No difference in barrier function property of healing skin as evidenced by TEWL levels was observed with the bioactive treatment but histamine treated wounds showed higher skin tensile strength. Taken together, our studies probe essential hallmarks of healing, and this could be useful for strategizing the translation of LASE to a larger pre-clinical animal model and also explore the multi-functionality aspect with a suitable bioactive or therapeutic agent.

2.2 MATERIALS AND METHODS

2.2.1 Materials

Silkworm (*Bombyx mori*) cocoons were purchased from Mulberry Farms, California, USA to obtain silk fibroin. Sodium carbonate (Na_2CO_3), lithium bromide (LiBr), and Histamine dihydrochloride ($C_5H_9N_3.2HCl$) were purchased from Millipore Sigma (St. Louis, MO) for silk fibroin extraction from silkworm cocoons. 3.5 kDa (MWCO) dialysis bags (Spectra/Por®) were purchased from Fisher Scientific for silk fibroin purification. Indocyanine green (ICG) dye was purchased from MP Biomedicals (#ICN15502050). All solutions were freshly prepared in nanopure water (NPW, resistivity ~ 18.2 MΩ-cm, Millipore filtration system, Darmstadt, Germany). Other reagents were stored at room temperature. BALB/c mice were purchased at ~10 weeks from Charles River Laboratories (Wilmington, MA, USA). Commercially-available 4-0 Monosof™ monofilament Nylon sutures (Medtronic, Minneapolis, MN) were purchased from esutures.com (Mokena, IL).

2.2.2 LASE fabrication

Silk fibroin was extracted from *Bombyx mori* silkworm cocoons according to previously described protocols(Rockwood et al., 2011; Urie, Guo, et al., 2018b). Briefly, silkworm cocoons

were degummed in a boiling 0.02M Na_2CO_3 (Sigma–Aldrich, St. Louis, MO) solution for 30 min, washed with distilled water three times, and dried at room temperature (RT). Degummed silk fibroin was dissolved in 9.3 M LiBr solution at 60 °C for 4 h, centrifuged to separate insoluble contents, and dialyzed for 72 h at 4 °C against a 3.5 kDa membrane to remove LiBr and impurities. Dissolved silk fibroin solution was centrifuged at 14000 rpm for 20 min to remove remaining impurities. Stock ICG solution (5mM dissolved in NPW) was added to aqueous silk fibroin solution (6 wt%) and homogenously mixed to obtain a final ICG concentration of 0.1mM. 500 μL of this solution was poured over 1cm*1cm square plastic coverslips and dried overnight at RT to obtain silk fibroin-ICG LASE films or simply LASE. LASE were stored at RT for further use.

2.2.3 LASE characterization

Absorbance spectra of ICG solution (0.1 mM), LASE as prepared, LASE after exposed to saline to form a viscous paste, and LASE after laser irradiation were recorded from 400 nm – 999 nm using UV-Vis absorption spectroscopy (Synergy 2 Multi-Mode Reader, BioTek Instruments; Winooski, VT). Absorbance spectra of NPW and silk fibroin film (LASE without ICG) was also recorded as controls for ICG solution and LASE, respectively.

A handheld, continuous wave near infrared (NIR) laser (LRD-0808, Laserglow Technologies, North York, Ontario, Canada), coupled with armored optical fiber with FC/PC connector (#AFF2001X, 1m length, and 200 μm core diameter), and tuned to 808 nm was used for laser irradiation. The fixed laser spot size was 2 mm. A FieldMate laser power meter used to measure the power of the laser beam and power density of the laser beam was calculated as the power of the laser beam/area of the laser beam. An A325sc infrared (IR) camera (FLIR, Nashua, NH) with 10 mm 45° lens measured the surface temperature of LASE during laser exposure.

2.2.4 ICG release from LASE

LASE were cut into 5 equal strips and each strip was individually laser irradiated with NIR laser tuned to 810 nm (laser power ~320 mW, power density ~0.64 W/cm^2) for 30 seconds; the length of films was similar to that used for laser sealing incisions in live mice described subsequently. Irradiated strips were individually incubated in 1mL with phosphate-buffered saline (PBS) at 37°C in a rotary shaker to investigate loss of ICG from films. At various pre-determined time points, 200 µL of the supernatant was collected and replaced with PBS. ICG was detected by absorbance analysis at 810 nm using UV-Vis spectroscopy (Synergy 2 Multi-Mode Reader, BioTek Instruments; Winooski, VT). A calibration curve was generated using different concentrations of ICG in PBS (0 - 0.07 mM ICG; the equation for the linear calibration curve was: y = 20.524x, where y = absorbance at 810 nm and x = concentration of ICG; R2 = 0.9987) and is shown in (Figure 2-1). Absorbance values of the supernatants were used in concert with this calibration curve to quantify ICG release from S-ICG films. All ICG release studies from LASE were carried out with four independent LASE films (n = 4). Release from LASE films without laser irradiation and pristine silk films (pS) were carried out as controls. *This experiment was performed, and the data reported has already been reported in this report(Urie et al., 2021).*

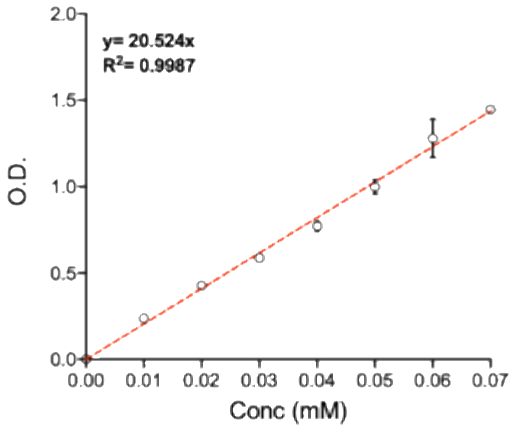

Figure 2-1. Calibration curves for quantifying ICG dye release from LASE.
Calibration curve of absorbance at 810 nm vs. concentration of ICG dye (0-0.07 mM) solution in 1x PBS. This curve was used for quantifying release of ICG dye from LASE following incubation in 1x PBS at 37 ºC placed in rotary shaker over a 72-hour time period. Data shown are mean ± standard error of mean of n = 2 experiments. *This experiment was performed, and the data reported has already been reported in this report(Urie et al., 2021).*

2.2.5 Sealing of murine incisional wounds

BALB/c mice (10-12 weeks, weighing ~22-25 g, Charles River Laboratories, Wilmington, MA) were used in this study and were housed in groups of five until surgery. All animal care and procedures were performed in strict compliance with protocol (#21-1830R) approved by the Institutional Animal Care and Use Committee (IACUC) at Arizona State University. Prior to surgery, mice were anesthetized with 120 mg/kg ketamine and 6 mg/kg xylazine (100 µL cocktail) by intraperitoneal injection. Dorsal hair was clipped, and the skin was prepped using three alternating swabs of chlorohexidine gluconate and 70% isopropyl alcohol. Two, 1-cm full thickness incisions were made side-by-side on the back of each mouse spaced roughly 2 cm apart using sterile scalpel blades (#15, Integra Miltex)(Ghosh et al., 2019). In case of suture closed incisions, four evenly spaced simple interrupted knots were used to close a 1-cm incision using 4-0 nylon suture (#SN5699G, Medtronic, Monosof Black 18" P-13 cutting). For LASE closed incisions, 10 µL of 1x phosphate buffered saline (PBS, pH 7.4) was topically applied and a 1.2 cm * 0.5 cm LASE was applied over the incision. LASE quickly dissolved into a viscous paste, the incision edges with the viscous paste in between were approximated using a forceps, and the incised edges were aligned prior to laser sealing. The LASE-tissue interface (incision line) was irradiated at a rate of 0.5 mm/second with the NIR laser tuned to 808 nm (CW) for 1 minute while keeping the incision line approximated using forceps. The laser was applied at an angle between 60° and 80° to the skin at a power density of ~5.1 W/cm^2 (~160 mW power output, ~2mm laser beam diameter), corresponding to temperatures in the range of 50-60 °C at the skin−LASE surface(Urie et al., 2021). Closure of left and right incisions with sutures or LASE were randomized. The mice were recovered on heating pads until mobile and they were housed individually to prevent removal of sutures or LASE. Incisions were assessed everyday up to 7 days post wounding for any signs of infection, suture removal, or wound dehiscence and mice with any of these conditions were removed from the study.

In case of histamine treatment along with LASE sealing, 10 µL of histamine (~40mM or 3.4 mg/kg dose dissolved in 1x PBS) was topically applied in between the incised skin edges and a

1.2cm * 0.5 cm LASE section was applied over the incision. In a similar fashion as described above, LASE section quickly dissolves into a paste, LASE-skin edges were approximated, laser irradiated for 1 minute, and recovered.

2.2.6 LASE imaging upon skin sealing

NIR fluorescence imaging, using a LiCOR Pearl Impulse (LI-COR Biosciences, Lincoln, NE) small animal imaging system, was carried out to visualize the persistence of LASE in the surgical incision area prior to and at pre-determined time points following sealing of skin incisions in live mice. Following anesthesia under isoflurane, mice were imaged in the LiCOR imager using default white, 700 nm and 800 nm channels. A region of interest (ROI) was identified around the incision area and the fluorescence from the 800 nm channel (excitation is 785 nm and emission is 820 nm) was determined from a region of the same size over the incision area for three different mice using the Image Studio Lite software (LI-COR Biosciences, Lincoln, NE) and reported in relative fluorescence units (RFU). *This experiment was performed, and the data reported has already been reported in this report.*

2.2.7 Measurement of transepidermal water loss (TEWL) of healing wounds

Transepidermal water loss (TEWL) as a function of time is used to assess the quality of skin barrier. TEWL was measured on Day 2, 4, 7 post-wounding and closure of incisions using LASE and suture using a portable, closed chamber VapoMeter device (#SWL5580, Delfin Technologies, Kuopio, Finland). The VapoMeter was fitted with a small adapter (4.5 mm diameter, ~16 mm^2 surface area) and close chamber condition was created on skin contact during the duration of measurement (~ 9-15 seconds). Ambient relative humidity and temperature (°C) were recorded during every measurement using a room sensor (#RHD1367) supplied along with the VapoMeter. For every TEWL reading, 3 consecutive measurements were taken along non-overlapping regions over an incision area and the chamber was passively ventilated between every measurement(Dini et al., 2014; Fluhr et al., 2006). Control measurements of TEWL were taken on

unwounded skin on the same days on sham mice. TEWL values were recorded using the DMC software (Delfin Technologies, Kuopio, Finland) and all values are displayed as mean ± standard error of mean from six independent mice (n = 6).

2.2.8 Mechanical recovery of healed skin strength

Following euthanasia, rectangular section of the healed skin (~2cm * 1cm) were excised around the incision area on Day 2 and 7 post-wounding for skin biomechanical analyses. In case of suture closed incisions, sutures were removed prior to tensile strength measurement to get strength of the healed skin alone. Excised healed skin samples were secured in clamps and stretched until failure stretched at a rate of 2 mm/s under constant tension using TA.XT Plus texture analyser (Texture Technologies Corp., Hamilton, MA). Ultimate tensile strength was determined from the maximum force of the tissue prior to failure, where the maximum force (F) and cross-sectional area of the tissue sample (A, length of skin sample 1cm and tissue thickness 500 μm) determined the ultimate tensile strength (σ, kPa) of healed skin (σ = F/A). The tensile strength of unwounded skin (~2cm length * 1cm) was also tested for comparison. All tensile strengths are displayed as mean ± standard error of mean from six independent experiments (n = 6).

$$\text{UTS of healed skin (in MPa)} = \frac{\text{Maximum force at skin ruptre (in N)}}{\text{Cross} - \text{sectional area of skin (in } m^2, \text{length} * \text{thickness)}}$$

% intact skin strength for healed skin were calculated as a difference between ultimate tensile strength for each group either at Day 2 or 7 post-wounding from unwounded skin strength, with the difference then converted to a percentage.

$$\%\ \text{intact skin strength} = \frac{\text{UTS of healed skin at Day 3}}{\text{UTS of unwounded skin (no incision control)}} \times 100$$

2.2.9 Ultrasound and photoacoustic imaging of LASE-tissue interface

Similar to skin mechanical strength recovery studies, rectangular section of the healed skin (~2cm * 1cm) were excised around the incision area on Day 2 and 7 post-wounding, collected in

biopsy cassettes, and stored in ice-cold 1x PBS for prior to ultrasound and photoacoustic imaging. Healed skin specimens were imaged within ~4 hours of necropsy and skin collection.

High-resolution ultrasound (US) and photoacoustic imaging (PAI) was performed with the MX550D (50MHz) linear array transducer, fiber bundle and motor setup of the Vevo 3100 + LAZR-X (VisualSonics). A transducer jacket (VisualSonics) was used to combine the transducer and fiber bundle, allowing the laser light to focus down to a region 7mm away from the transducer head. Skin specimens were removed from 1x PBS, excess buffer was blotted, and embedded in a 1.5% agarose (Millipore Sigma, #A9539, low EEO) within an in-house 3D printed tray. The outer section of the tray was filled with deionized water to have the agarose layer submerged under deionized water. The transducer with jacket was lowered into the water bath achieving proper opto-acoustic coupling for PAI with a standoff of approximately 7mm (Figure 2-4).

For 3D scanning of skin, the transducer with jacket was incremented at a 150-µm step size across the length of each skin sample. For each skin specimen, PA data is obtained at 8 wavelengths (40-nm increments from 680-960nm) for each depth/width cross-section of the 3D scan, along with a standard US image. A center slice for each sample is chosen for full PA spectrum characterization (5-nm increments from 680-960nm). Furthermore, length/width sample cross-sections are compiled from the 3D dataset in image post processing.

Spectral unmixing was performed on the obtained PA signal to discern the tissue constituents. Control skin has a relatively weak and flat PA spectrum across the wavelength band, implying that the strong ICG absorption at 800nm can be used to recognize LASE within the samples (Figure 2-4). The VevoLAB software (VisualSonics) is utilized for such spectral unmixing, where 3 wavelength components (680, 800, 960nm) are used to discern LASE signal from that of the weakly-absorbing normal skin. Multi-wavelength unmixing for ICG content done via the Vevo system has been shown previously to produce accurate results(Forbrich et al., 2017; Ratto et al., 2019). In order to isolate ICG content that is still bound to LASE (not leached out of the LASE over time) a threshold is applied on all subsequent images to only display the strongest 25% of the predicted ICG content. A similar technique is used to discern signal from sutures (Nylon 4-0) from

that of normal skin; given that the black suture is very strongly absorbing, a 10% threshold is applied to a raw PA image taken at 680nm. This thresholder signal is then expected to originate from the suture as opposed again to the weakly-absorbing skin. *These studies were conducted at University of Arizona under the supervision of Prof. Russell S. Witte and was performed by Chris Salinas.*

2.2.10 Tissue collection and processing

Following euthanasia, healed tissues were carefully excised, flattened between two foam biopsy sponges in a tissue cassette, and fixed by submersion in 10% neutral-buffered formalin (#HT501128, Sigma Aldrich, St. Louis, MO) for a minimum of 72 hours at room temperature. Tissues were dehydrated thorough a graded alcohol series and paraffin embedded with Paraplast Plus (#19217, EMS Diasum, Hatfield, PA) by manual processing (Appendix). Individual 5-micron sections were cut with an Accu-Cut® SRM™ 200 Rotary Microtome (Sakura Finetek USA, Torrance, CA) and captured on charged glass slides (Hareta, Springside Scientific, Durham, NC) in a floating water bath (XH-1003, IHC World, Ellicott City, MD). Slides were dried overnight at 37 °C and stored at room temperature until use.

2.2.11 Haematoxylin and Eosin (H&E) staining

Dried sections on charged glass were deparaffinized and rehydrated thorough xylene and graded alcohols into tap water. Rehydrated sections were submerged in a solution of Hematoxylin (Gill No. 2, #GHS232, Sigma Aldrich, St. Louis, MO) for 3 minutes, differentiated by 6-12 quick dips in acid alcohol (0.3% hydrochloric acid in 70% ethanol), and blued in a solution of ammonium water (0.2% ammonium hydroxide in distilled water) for 30 seconds. Slides were further submerged in a solution of 0.5% Eosin Y (#318906, Sigma Aldrich, St. Louis, MO) in distilled water (acidified with 0.2% glacial acetic acid) for 4 minutes followed by dehydration thorough an abbreviated 90% and absolute ethanol series, further dehydrated in xylene and mounted in CytoSeal XYL (Richard-Allan/Thermo Fisher Scientific, Kalamazoo, MI). Samples were imaged on an Olympus BX43

upright microscope equipped with an Olympus DP74 CMOS camera operated by cellSens Standard software (Olympus Corporation, Center Valley, PA).

2.2.12 Picrosirius Red staining

Dried sections on charged glass were deparaffinized and rehydrated thorough xylene and graded alcohols into tap water. Rehydrated sections were submerged in a 0.1% solution of Picrosirius Red composed of Direct Red 80 (#365548, Sigma Aldrich, St. Louis, MO) in a saturated aqueous solution of picric acid (#P6744, Sigma Adlrich, St. Louis, MO) for 1 hour at room temperature to achieve stain saturation. Slides were washed twice in acidified water (0.5% glacial acetic acid in distilled water) for 2 minutes each. Slides were dehydrated thorough an abbreviated 90% and absolute ethanol series, further dehydrated in xylene and mounted in CytoSeal XYL (Richard-Allan/Thermo Fisher Scientific, Kalamazoo, MI). Brightfield images were collected on an Olympus BX43 upright microscope equipped with an Olympus DP74 CMOS camera operated by cellSens Standard software (Olympus Corporation, Center Valley, PA). Polarized images were collected on a Revolve microscope (Echo, San Diego, CA).

2.2.13 Image analyses

Morphometric features of healing were assessed in ImageJ/FIJI. Images were calibrated according to magnification. Epidermal gap was measured as the linear distance between the two epidermal faces of the wound edges and identified by canonical appearance of the epidermis via H&E staining on Days 2 and 7 post-injury. Histological scar area was measured as the area weakly stained by Picrosirius Red and bounded by the basement of the epidermis and above the hypodermis, and the edges of the mature collagen in peri-wound tissue strongly stained by Picrosirius Red on Day 7 post-injury(Gurtner et al., 2011).

2.2.14 Statistical Analyses

Data from absorbance, TEWL, and skin ultimate tensile strength are presented as mean ± standard error of the mean (SEM). Differences between groups were assessed using two-way analysis of variance (ANOVA) followed by Fisher's LSD test using GraphPad Prism version 9.2.0 (GraphPad, USA). A p-value < 0.05 was considered statistically significant.

2.3 RESULTS

2.3.1 Generation and characterization of LASE

The fabricated Light-activated sealant (LASE) (Figure 2-2A) comprising of silk fibroin protein and Indocyanine green (ICG) dye displayed a characteristic absorbance similar to ICG dye (Figure 2-2B). LASE upon exposure to saline dissolves to form an adhesive viscous paste ideal for tissue sealing and it maintains its absorbance in the NIR window as to a dry LASE film. This viscous adhesive paste was irradiated using a handheld continuous wave laser tuned to 808 nm under conditions similar to in vivo skin sealing and following laser irradiation no significant shift in the absorbance profile of LASE was observed (Figure 2-2B). This warrants the use of absorbance based visualization methods for probing LASE following tissue sealing.

We also investigated the photothermal response of fabricated LASE to a continuous wave handheld near-infrared (NIR) laser tuned to 808 nm irradiated in a 15 s laser "on" and 15 s laser "off" cycle for a total of three cycles. For the photothermal response studies, a LASE section was applied to an ex vivo porcine skin where the LASE section turned into a viscous paste upon contact with the skin and the surface temperature was recorded using an infrared (IR) camera. Upon irradiation with laser, a rapid increase in surface temperature of the LASE-tissue interface was observed due to efficient photothermal conversion of the embedded ICG dye in the LASE matrix. This photothermal response was reproducible over three cycles and varied using different laser power densities (1.6 to 2.4 W/cm^2) (Figure 2-2C). Irradiation of porcine skin alone and LASE without ICG even at the higher laser power density tested (2.4 W/cm^2) did not result in any

photothermal response (red and blue dotted line, respectively, Figure 2-2C). Surface temperatures in the range of 50–60 °C (shown using blue shaded region) optimal for tissue sealing was achieved by modulating the laser power density (Figure 2-2C).

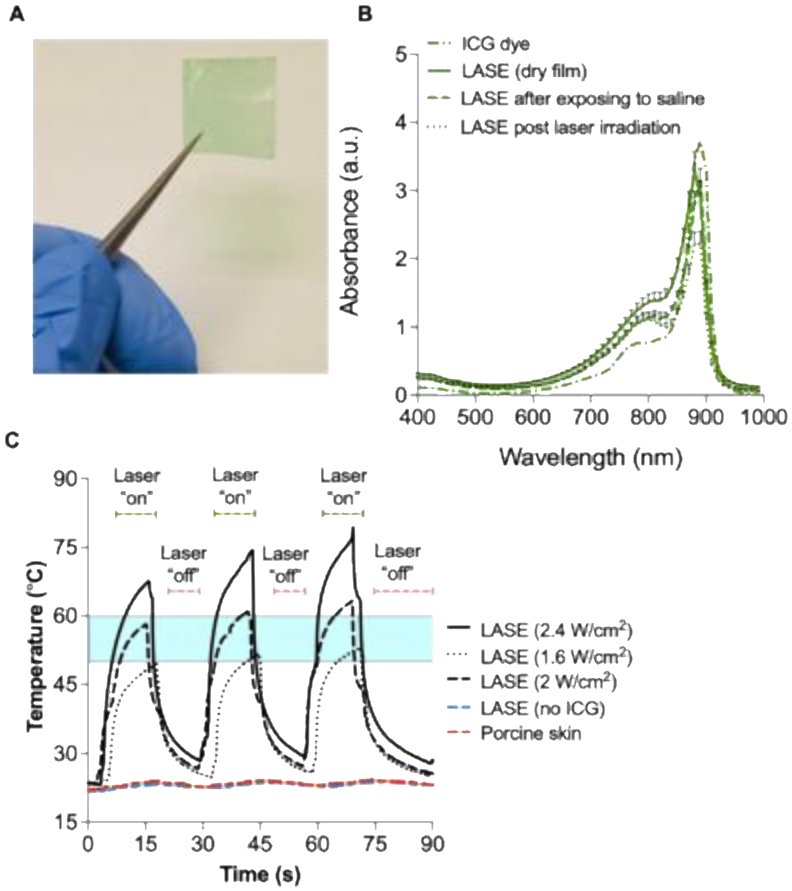

Figure 2-2. Light-activated sealant (LASE) fabrication and characterization.
(A) Representative image of a 2cm*2cm LASE film fabricated from silk fibroin and indocyanine green (ICG) dye. (B) Absorbance spectra of ICG dye alone (dashed and dotted line), LASE film - as it is fabricated (solid green line), in a viscous paste form after exposure to saline mimicking wound bed moist environment (dashed green line), and post laser irradiation in the paste form (dotted green line). Data shown are mean ± standard error of the mean of n = 4 independent LASE sections. (C) Photothermal response of LASE on ex vivo porcine skin irradiated using a continuous wave NIR laser tuned to 808 nm at varying laser power density from 1.6 W/cm2 to 2.4 W/cm2 in a 15 s “on” and 15 s “off” cycle (3 cycles total). Photothermal response of LASE (with no ICG dye added, red dashed line) and porcine skin (blue dashed line) to 2.4 W/cm2 is indicated as baseline. The blue shaded region (50°C to 60°C) indicates the optimal temperature window for laser tissue sealing. Each photothermal response curve is a mean of n = 3 independent experiments.

2.3.2 ICG release from LASE

Release studies were carried out with LASE to determine loss of the ICG dye from these biosealants. The release profile of ICG dye can possibly be a surrogate for estimating the release pattern of a bioactive of similar molecular weight and chemical property as ICG dye.

An initial burst of ICG was seen from the LASE, but no further loss was seen over 72 h. Laser irradiation of LASE reduced the loss of ICG likely because of structural changes to the silk fibroin matrix. It is likely that the ICG dye is retained in LASE and the wound site over longer periods of time, which can facilitate reliable photothermal sealing and visualization, respectively.

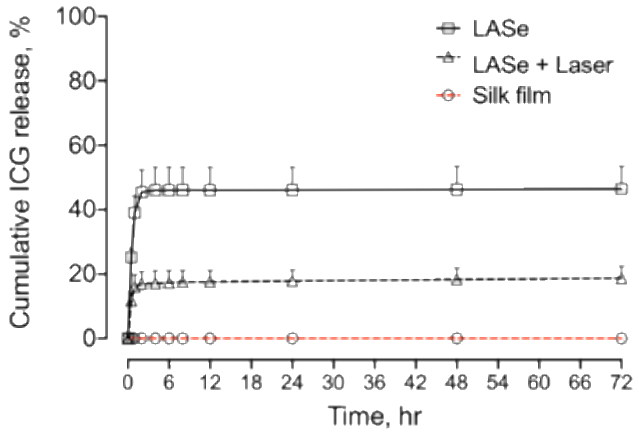

Figure 2-3. Release characterization of LASE.
Cumulative ICG release from LASE following laser irradiation (laser power ~320 mW, power density ~0.64 W/cm^2) for 30 seconds and incubated in 1x PBS at 37°C for the duration of the study. Release from LASE films without laser irradiation and pristine silk films (pS) were carried out as controls. The line joining individual data points is shown only for visualization. Data indicate mean ± standard error of mean of n = 4 experiments carried out with four independent LASE films. *This experiment was performed, and the data reported has already been reported in this report(Urie et al., 2021).*

2.3.3 Murine incisional skin sealing: Barrier function recovery and healed skin strength

Full thickness incisional dorsal skin wounds in BALB/c mice, 1-cm in length, were sealed using LASE and 4-0 Nylon sutures. In case of LASE closed incisions, the LASE-tissue interface

(incision line) was irradiated for 1 minute at a power density of ~5.1 W/cm^2 (~160 mW power output, ~2mm laser beam diameter), corresponding to temperatures in the range of 50-60 °C at the skin−LASE surface. Mice were recovered and representative images of incisions at day 0, 2, 4, 7 are shown. Mice without incisions were surgically prepped, recovered in a similar manner, and were used as controls in subsequent studies (Figure 2-3A).

Following wounding and closure of skin incisions, barrier function recovery of healing skin section was probed in a non-invasive manner using transepidermal water loss (TEWL). TEWL is a marker of skin permeability which measures water loss thorough the stratum corneum layer and is one of the standard methods to evaluate barrier function of skin. Any damage or trauma to the skin barrier leads to an increase in TEWL levels(Fluhr et al., 2006). TEWL levels of both LASE and suture closed incisions were measured on days 2, 4, and 7 post wounding. For an 1-cm long incision, TEWL measurements were collected from three non-overlapping regions (shown by white arrows) over the incision line for suture, LASE and control groups (Figure 2-3B).

LASE and suture closed incisions during the course of the healing period showed gradual decrease in TEWL values. At day 2 post wounding, the average TEWL value for incisions closed with LASE (29.53 ± 1.94 g/m^{2}h) was significantly lower than sutured incisions (41.58 ± 4.39 g/m^{2}h, p-value 0.0001). On Day 4 and 7 post wounding, TEWL levels of LASE closed incisions were lower on compared to suture (20.62 ± 0.62 g/m^{2}h vs 25.53 ± 0.72 g/m^{2}h, p-value 0.0893 and 17.30 ± 1.12 g/m^{2}h vs 21.23 ± 1.74 g/m^{2}h, p-value 0.0893), but no significant difference in TEWL levels between the two closure methods was observed. Average TEWL values of an unwounded skin on Day 2, 4, and 7 post wounding was considered as baseline (Figure 2-3D).

Mice were euthanized on Day 2 and 7 post wounding to evaluate biomechanical properties of healing skin both at an early and late healing point. At an earlier healing timepoint (Day 2 post wounding), LASE closed incisions had higher ultimate tensile strength (0.87 ± 0.13 MPa) compared to sutured incisions (0.47 ± 0.08 MPa, p-value 0.0464). The ultimate tensile strength of unwounded (no incision control) skin of BALB/c mice of the same age range was determined to be 2.67 ± 0.17 MPa and was used to compare the efficacy healing using sutures and LASE. Incisions closed with

sutures and LASE resulted in a recovery of approximately 20.4 ± 2.6 and 35.4 ± 3.6 % in UTS, respectively, relative to that of intact skin at Day 2 post wounding (shown in secondary axis) (Figure 2-3E). Our results indicate improved efficacy in healed skin tensile strength at an earlier timepoint with LASE and we also observed similar improvement in healing in our previous study using silk fibroin-gold nanorod sealant for incisional skin repair(Urie, Guo, et al., 2018b).

At the late healing timepoint (Day 7 post wounding), ultimate healed skin strength of LASE and suture closed incisions increased to 1.15 ± 0.23 MPa and 1.11 ± 0.16 MPa, respectively (ns, p-value 0.8720). At this timepoint, sutures and LASE resulted in a recovery of approximately 41.6 ± 4.9 and 43.1 ± 7.1 % in UTS, respectively, relative to that of intact skin (shown in secondary axis) (Figure 2-3E). Mouse skin wounds heal by contraction and an earlier timepoint is a better representation for evaluating sealing efficacy and biomechanical recovery between sealing methods. The reduction in evaporative water loss (TEWL levels) and improved tensile strength at Day 2 post wounding can be indicative of early recovery of skin barrier function, which can help prevent wound dehiscence, combating infections, etc.

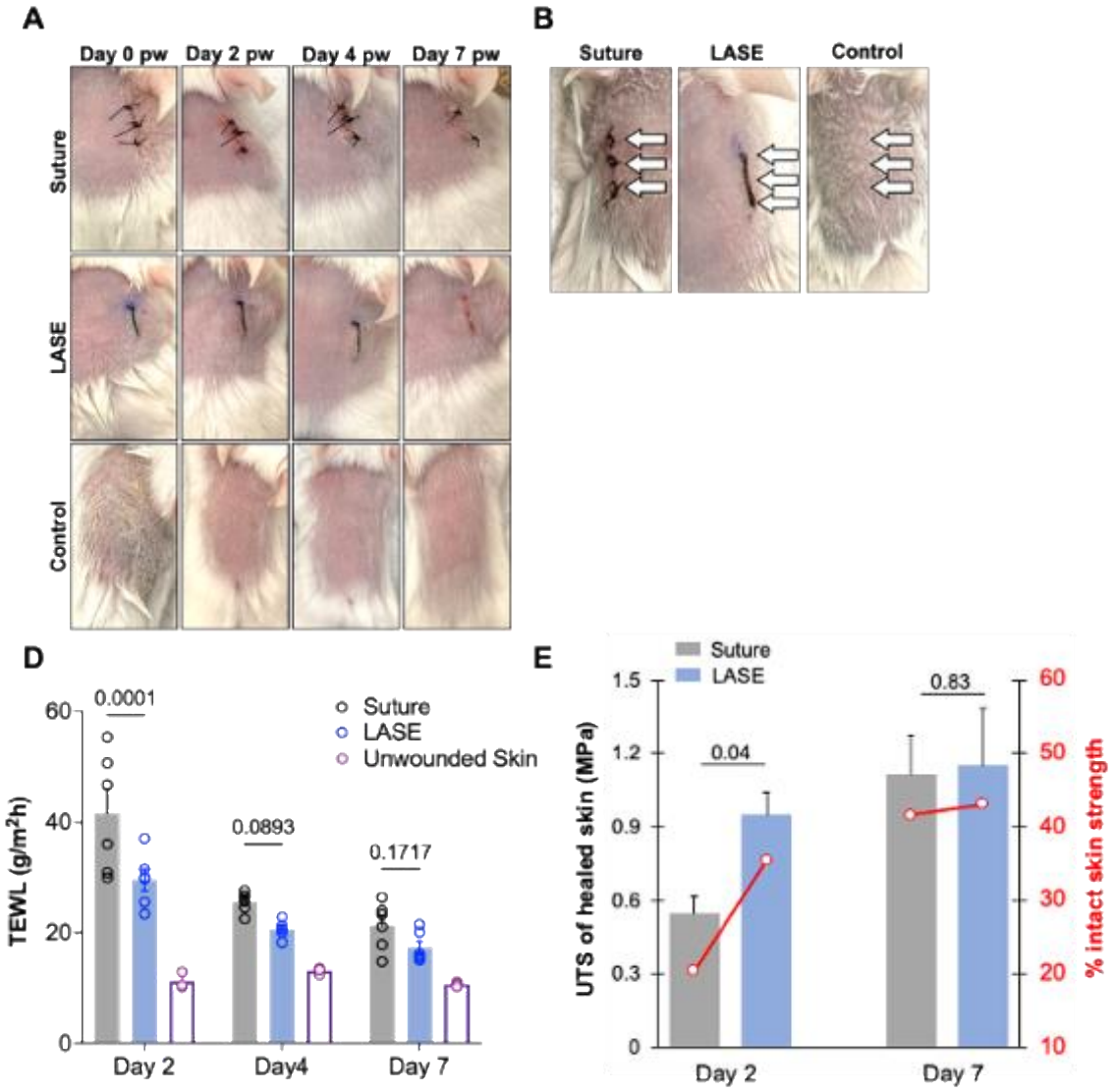

Figure 2-4. Incisional skin sealing and characterization of healing skin.
(A) Representative images of 1-cm long skin incisions closed with four simple interrupted 4-0 nylon sutures or LASE at Day 0, 2, 4, and 7 post wounding; control is unwounded skin surgically prepared similar to incised skin (B) Representative image showing three locations at which TEWL measurements were carried out (white arrows) for each type of closure method. (C) (D) Transepidermal water loss (TEWL) of healed skin and unwounded control skin on Day 2, 4, and 7 post wounding. TEWL value (in g/m^2h) for each incision type is the average TEWL measurement from three non-overlapping spots over the incision line. Data shown are mean ± standard error of the mean of n = 6 mice. (E) Ultimate tensile strength (UTS) and % intact skin strength (secondary axis shown in red) of healed skin at Day 2 and 7 post wounding for suture and LASE closed incisions. Data shown are mean ± standard error of the mean of n = 6 mice. Statistical significance was determined using two-way ANOVA followed by Fisher's LSD test and individual p-values are shown and p-value < 0.05, which was considered statistically significant.

2.3.4 Persistence of LASE in the incision area following sealing

Following incision closure using LASE, the incision area was visualized using digital photography, white light, and fluorescent imaging (800 nm channel) at pre-determined timepoints from 6 hours to day 10 following sealing (Figure 2-4A). Imaging of skin incision prior to application of LASE was performed and no autofluorescence signal was observed from the 800 nm channel. Visualization of the incision area indicated persistence of LASE at the wound site for 5-7 days post sealing after which, the LASE likely sloughed off from the skin of the mice (Figure 2-4B). The relative fluorescence units (RFU) of each timepoint gradually decrease over the course of healing and reached basal levels as LASE sloughed off the healing incision area (Figure 2-4C-D). This method of tracking the persistence of LASE in the wound bed has a limitation as ICG dye is not chemically conjugated to the silk fibroin and leaching of ICG dye could possibly affect visualization. As a part of a future follow-up study, ICG dye chemically conjugated to silk fibroin will be used to fabricate LASE and used for visualization studies.

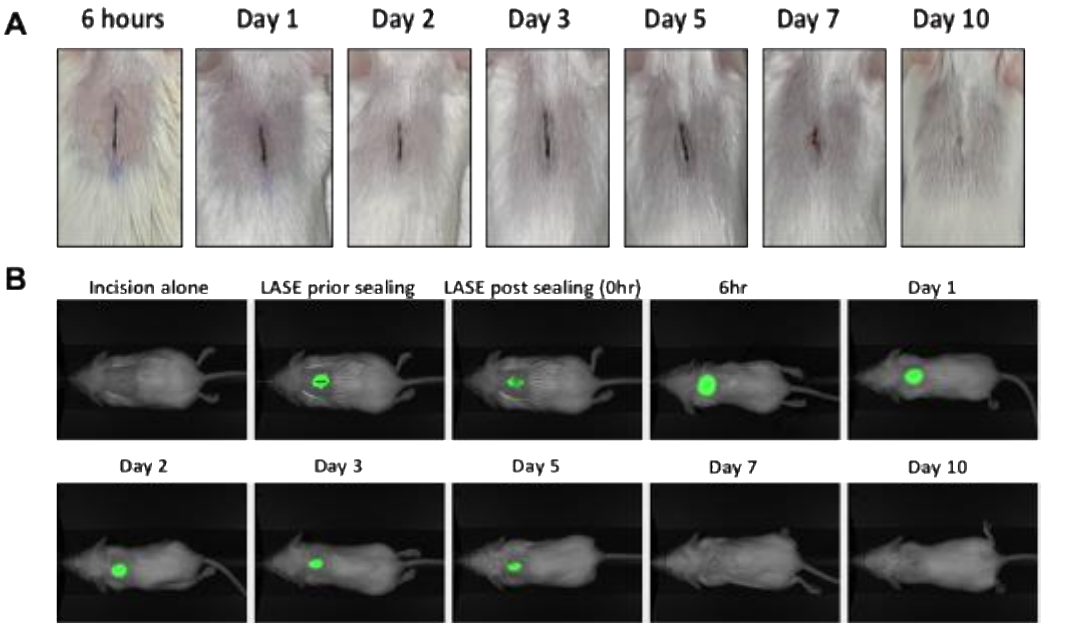

C

Timepoints	RFU @ 800nm channel		
	Mouse 1	Mouse 2	Mouse 3
0 hour	18700	4650	6560
6 hours	38900	26900	15100
Day 1	19800	17500	11700
Day 2	12400	8790	9560
Day 3	11000	10800	7420
Day 5	9560	9830	7790
Day 7	601	9130	957
Day 10	554	726	833

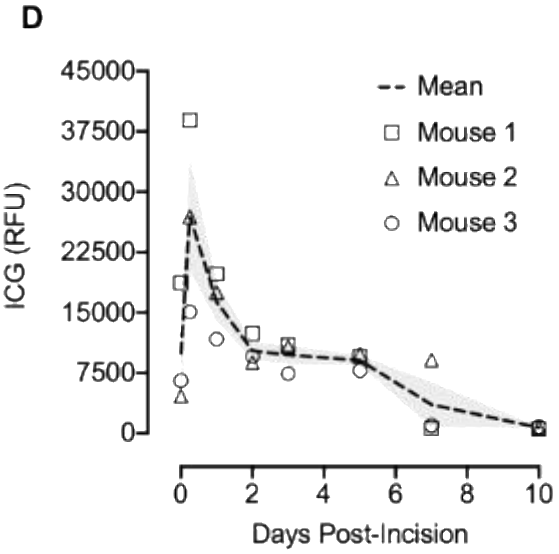

Figure 2-5. Persistence of LASE following incision sealing.
Representative digital images of 0.75 cm-long incisions in BALB/c mice closed using LASE at various timepoints following sealing. (B) Fluorescent images (800 nm channel) overlaid on white channel of the same incision at similar timepoints. Incision alone image shows no significant fluorescent signal from mice skin alone. (C) Fluorescence intensity (RFU at 800 nm channel) of ICG in three mice used for investigating the persistence of LASE over a period of 10 days. (D) Quantitative analysis of fluorescence intensity of the incision site over 10 days, where the grey shaded region represents mean ± standard error of mean of n = 3 experiments. *This experiment was performed, and the data reported has already been reported in this report(Urie et al., 2021).*

2.3.5 Ultrasound and Photoacoustic Imaging

Excised ex vivo skin sections were embedded into 1.5% agarose (low EEO) gel inside a 3D printed tray. The outer section of the tray was filled with deionized water to achieve proper opto-acoustic coupling for US and PAI imaging with a standoff of approximately 7mm between skin samples and the transducer jacket (figure 2-6A, B). For photoacoustic signal, full spectrum photoacoustic scan between 680-980 nm with a 5-nm increment was performed for a representative center slice of every skin sample. Spectral unmixing of the photoacoustic signal was performed to detect absorbance of LASE, suture, and skin constituents (Figure 2-6C). The average photoacoustic signal was further normalized. In case of control skin, no peak absorbance was observed at these wavelengths and in case of LASE sealed skin samples intense signal is observed at 800nm which is expected from the characteristic ICG dye absorbance embedded in the LASE matrix (Figure 2-6D).

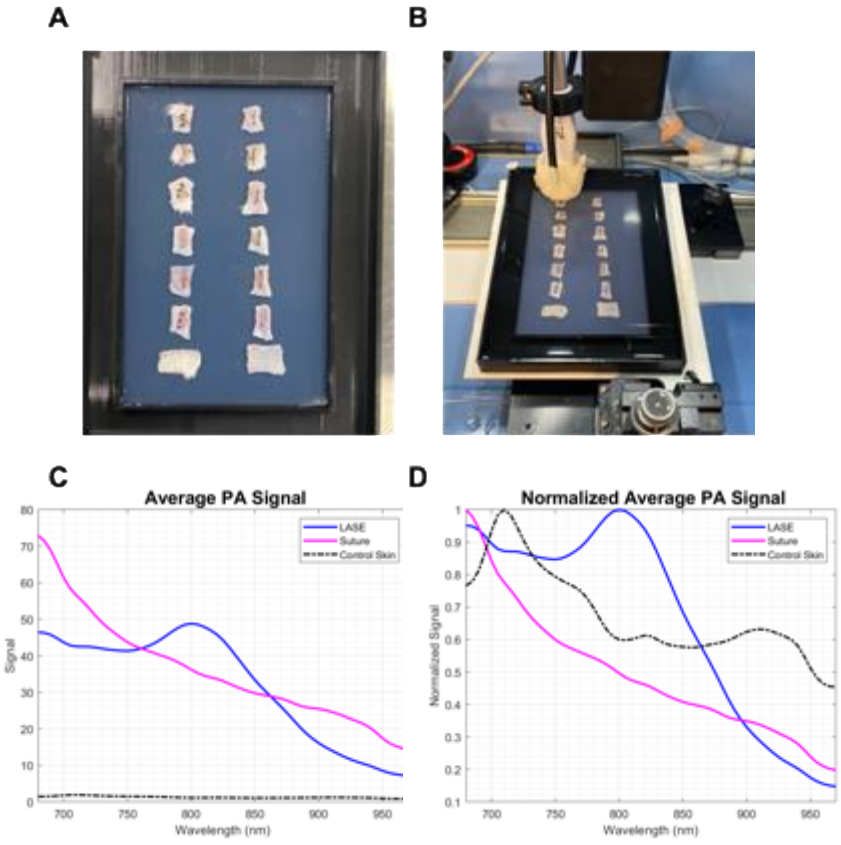

Figure 2-6. Setup for ultrasound (US) and photoacoustic imaging (PAI).
(A) Prior to imaging, excised skin samples were removed from ice cold 1x PBS and placed over a layer of 1.5% agarose (low EEO) cooled to room temperature in a 3D printed sample tray. Following this, another layer of agarose solution (~30 °C) was poured over the skin samples to completely embed the skin samples within an agarose layer. The sample tray was then filled with deionized water to form a layer over the agarose layer. (B) Scanning of skin samples using a MX550D (50MHz) linear array transducer. The transducer is lowered into the sample tray covered with water to achieve proper opto-acoustic coupling with an approximately 7mm standoff from the skin samples.

Depth and width (x/y) cross-sections of the normalized photoacoustic signal with unmixed wavelengths of 680 nm, 800 nm, and 960 nm of control skin (no incision), LASE sealed skin incisions at day 2 post-wounding, and LASE sealed skin incisions at day 7 post-wounding are shown (Figure 2-7A). In case of control skin, no peak absorbance was observed at these wavelengths and in case of LASE sealed skin samples intense signal is observed at 800nm which is expected from the characteristic ICG dye absorbance embedded in the LASE matrix (Figure 2-7B, C). It is evident that there will be minimal background interference from skin and the 800nm signal can be used for probing LASE in the skin during the course of the healing process.

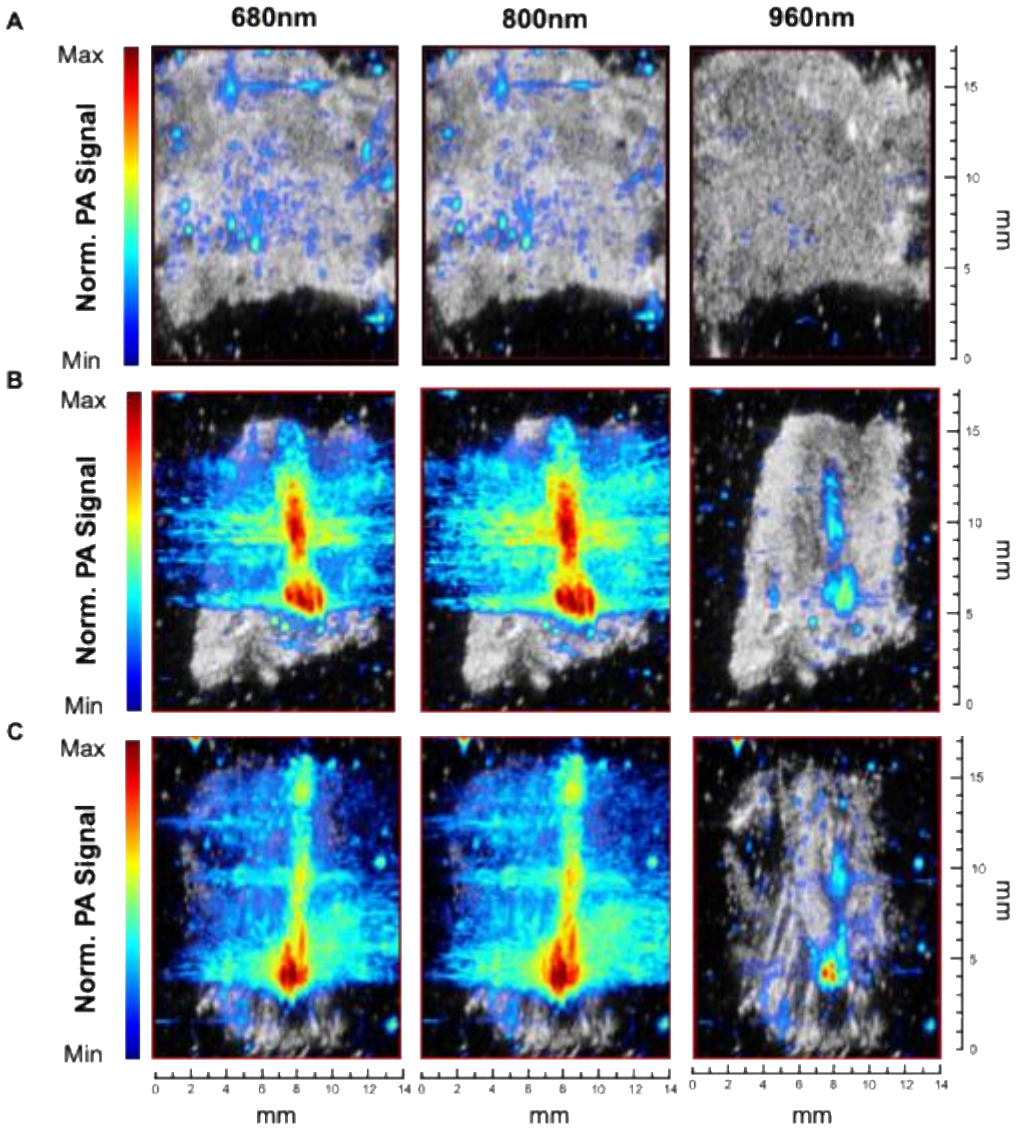

Figure 2-7. Wavelength unmixing and normalized PA signal.
Computed lateral slices of B-mode scans overlaid with normalized PA signal at 680nm, 800nm, and 960nm for (A) control skin without any incision surgically prepped similar to skin samples with incisions (B) skin incisions sealed using LASE at day 2 post-wounding and sealing (C) skin incisions sealed using LASE at day 7 post-wounding and sealing. All the cross-sectional slices were recorded at the near surface level at approximately 500 µm sub-surface depth.

It was qualitatively observed that there was a considerable drop in normalized PA signal at 800nm on day 7 post-wounding compared to day 2 post-wounding. This is further shown by spectral unmixing; thresholder LASE signal identified by the spectral unmixing technique at both day 2 and 7 post-wounding. The maximum depth penetration of LASE signal in the wound bed from four independent LASE sealed skin incisions was calculated from the normalized PA signal overlaid on individual B-mode images at both the timepoints (Figure 2-8). The average depth of LASE signal in the wound bed was 1.40 ± .21 mm and 0.60 ± 0.45 mm on day 2 and day 7 post-wounding samples, respectively (Figure 2-8A, B). These profiles depth can be indicative of persistence of LASE in the wound bed as the healing of the incisional wound progresses over time.

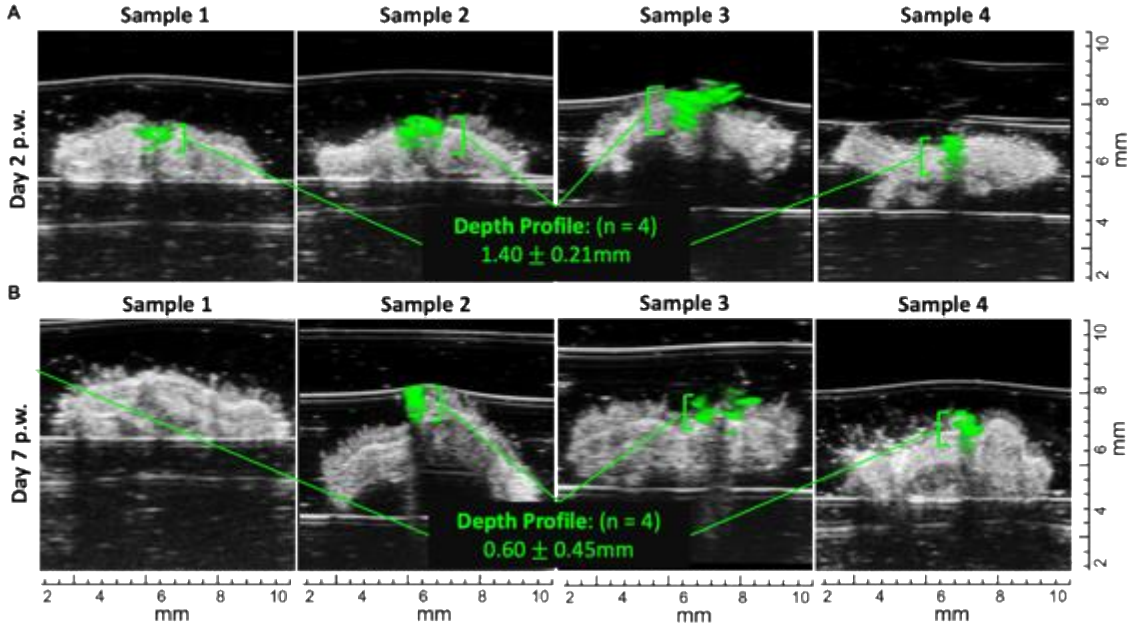

Figure 2-8. Depth profile of LASE in wound bed.
Axial slices of B-mode scans with overlaid normalized PA signal from LASE at 800nm shown in green for samples at (A) day 2 post-wounding and (B) day 7 post-wounding. The depth profiles are represented as mean ± standard error of mean of n = 4 LASE-sealed skin samples at each timepoint.

Further *in vivo* studies to track the persistence of LASE in the same mouse will be beneficial and help minimize any differences arising between sealed skin samples from different mice at each

timepoints. Additionally, we are working on reporting a volumetric profile of PA signal from LASE (green signal in Figure 2-8 A, B) will be calculated as a ratio to each individual tissue area.

2.3.6 Histological evaluation of healing skin sections

During wound healing, re-epithelialization is a crucial step and prevent exposure to pathogens leading to surgical site infections(Pastar et al., 2014). At day 2 post-wounding, suture closed skin incisions had a lower epidermal gap compared to LASE closed incisions. By day 7 post-wounding, no significant difference in epidermal gap was observed between the two groups. We also evaluated the histological scar area observed thorough picrosirius staining to see if there is a difference in initial scarring during the healing period in incisions closed with suture or LASE. Incisional wounds had a histological scar area of 0.07 ± 0.01 mm^2 and 0.08 ± 0.01 mm^2 ($p > 0.05$) with closed three-interrupted knots of Nylon 4-0 suture and LASE, respectively at day 7 post-wounding.

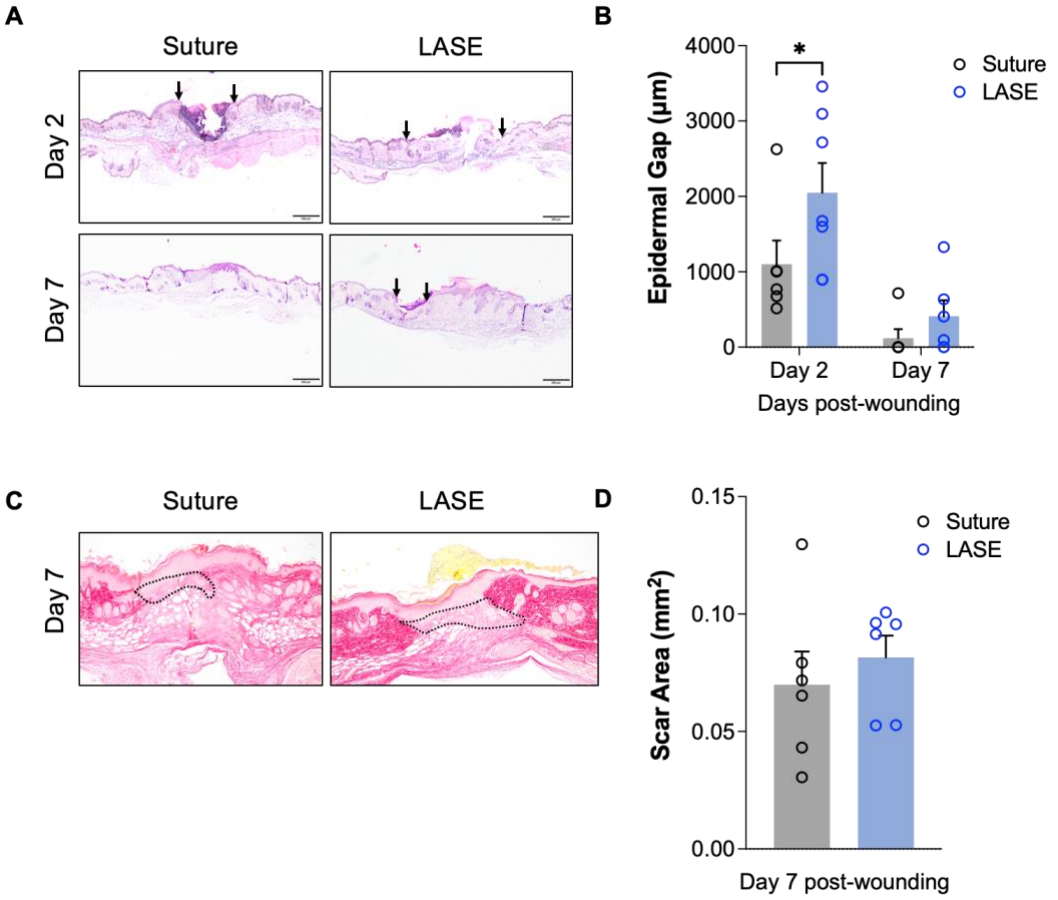

Figure 2-9. Histological evaluation of skin sections during the course of healing.
(A) Representative hematoxylin and eosin (H&E) stained micrographs of the wound sections (4x magnification) showing the epidermal gap (black arrows) at day 2 and 7 post wounding (scale bar = 200 µm). (B) Quantification of epidermal gap in skin sections (in µm) closed with suture and LASE at day 2 and 7 post-wounding. (C) Representative picrosirius red stained micrographs of the wound sections (10x magnification) showing the scar area in the granulation tissue (black dotted line area) at day 7 post wounding. (D) Quantification of histological scar area (in mm^2) in skin sections closed with suture and LASE at day 7 post-wounding. Data shown are mean ± standard error of mean of n = 6 mice per group. Statistical significance was determined using two-way ANOVA (for epidermal gap quantification) and one-way ANOVA (for scar area quantification) with Fisher's LSD post-hoc analysis. *$p < 0.05$ is considered significant.

We will be conducting additional staining of healed skin samples with various immune cell markers (Ly-6G, iNOS, and Arg-1) to assess immune cell infiltration and activity at the suture-tissue or LASE-tissue interface. Myofibroblast activity (αSMA) and neoangiogenesis (CD31) levels will also be evaluated for further comparing healing outcomes between the suture and LASE group.

2.3.7 Combining bioactive with LASE: Barrier function recovery and healed skin strength

We also investigated the effect of a bioactive delivery on repair and healing outcomes prior to sealing incisions with LASE. As the first bioactive, histamine dihydrochloride (10 µL of 40.8 mM or 7.5 mg/mL in 1x PBS) was topically applied in the wound bed after the incision was made and then LASE was applied (LASE-His). The LASE section turned into a viscous adhesive paste upon contact with the wound bed and the histamine dihydrochloride solution. The incisions were sealed in a similar manner and similar laser irradiation parameters (laser power density ~5.1 W/cm^2, 1 minute irradiation, and temperatures in the range of 50-60 °C at the skin−LASE surface) as described above in case of LASE alone skin sealing. Mice were recovered and representative images of incisions at day 0, 2, 4, 7 are shown. Mice without incisions were surgically prepped, recovered in a similar manner, and were used as controls in subsequent studies (Figure 2-10A).

TEWL levels was measured on days 2, 4, and 7 post wounding to assess the barrier function of the healing skin and effect of topical histamine treatment on barrier function. Similar to skin incisions closed with LASE, a gradual decrease in TEWL values was observed on days 2, 4, and 7 post wounding in LASE-His closed incisions. At day 2 post wounding, the average TEWL

value for incisions closed with LASE and LASE-His were 29.53 ± 1.94 g/m^{2}h and 30.88 ± 1.52 g/m^{2}h, respectively ($p > 0.05$). On Day 4 and 7 post wounding, TEWL levels of LASE and LASE-His closed incisions were 20.62 ± 0.62 g/m^{2}h vs 22.89 ± 0.55 g/m^{2}h, p-value 0.18 and 17.30 ± 1.12 g/m^{2}h vs 18.48 ± 0.44 g/m^{2}h ($p > 0.05$, Figure 2-10B). Average TEWL values of an unwounded skin on Day 2, 4, and 7 post wounding was considered as baseline. During the course of healing, addition of bioactive prior to application of LASE did not alter the barrier function recovery compared to skin sealing using LASE alone.

To evaluate the efficacy of a bioactive treatment, mice were euthanized on Day 3 and 7 post wounding to evaluate biomechanical properties of healing skin both at an early and late healing point. At an earlier healing timepoint (Day 3 post wounding), topically delivery of histamine in the wound bed prior to LASE application and sealing (LASE-His group) resulted in higher ultimate tensile strength (1.21 ± 0.09 MPa) compared to LASE sealing (0.94 ± 0.04 MPa, $p< 0.05$). LASE and LASE-His closed incisions resulted in a recovery of approximately 35.28 ± 1.7 and 45.37 ± 2.9 % in UTS, respectively, relative to that of intact skin at Day 3 post wounding (shown in secondary axis) (Figure 2-10C). This indicates improved efficacy in healed skin tensile strength at an earlier timepoint by combining bioactive with LASE compared to sealing using LASE alone. At the late healing timepoint (Day 7 post wounding), ultimate healed skin strength of LASE and LASE-His incisions increased to 1.15 ± 0.23 MPa and 1.47 ± 0.05 MPa, respectively ($p > 0.05$). At this timepoint, LASE and LASE-His resulted in a recovery of approximately 43.1 ± 7.1 % and 55.12 ± 1.8 % in UTS, respectively, relative to that of intact skin (shown in secondary axis) (Figure 2-10C). Our results corroborates to a previous finding which reported incisional wounds in rats treated with histamine (i.p. injections) 10-days prior to surgery and every day post-surgery till endpoint of the study (day 5 or 10 post-wounding) higher skin tensile strength at day 5 post-wounding and histologically improved healing outcomes but the differences were not significant at day 10 post-wounding (Boyd & Smith, 1959). Another study reported histamine application (0.1 mg of Histamine/animal for 6 days post-wounding delivered thorough implanted subcutaneous sponges)

along with compound 48/80 and ATP had stimulatory effect on wound healing and skin tensile strength of healing rat incisional wounds(Dabrowski et al., 1975).

Additional staining of healed skin samples with various immune cell markers (Ly-6G, iNOS, and Arg-1), myofibroblast activity (αSMA), and neoangiogenesis (CD31) for further assessing healing outcomes due to addition of histamine as bioactive for incisional wound healing.

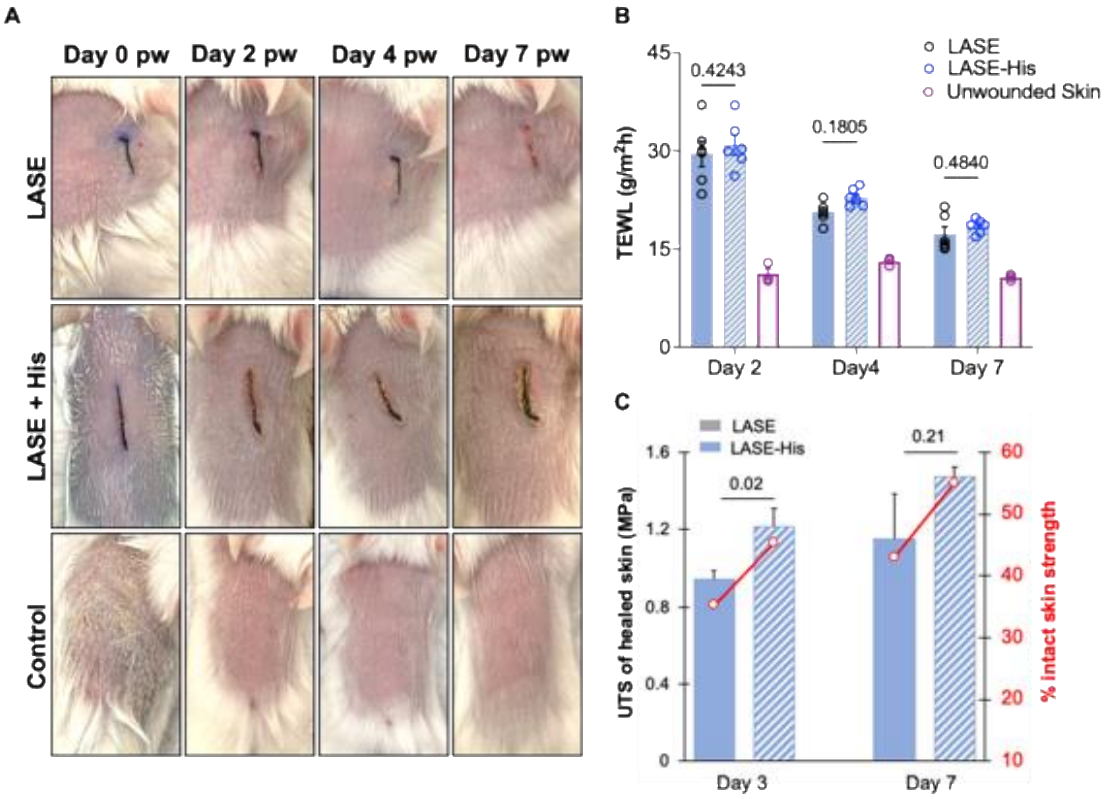

Figure 2-10. Incisional skin sealing using LASE combined with bioactive delivery and characterization of healing skin.
(A) Representative images of 1-cm long skin incisions closed with LASE or wounds topically treated with histamine and then sealed using LASE (LASE-His) at Day 0, 2, 4, and 7 post wounding; control is unwounded skin surgically prepared similar to incised skin. (B) Transepidermal water loss (TEWL) of healed skin and unwounded control skin on Day 2, 4, and 7 post wounding. TEWL value (in g/m^2h) for each incision type is the average TEWL measurement from three non-overlapping spots over the incision line. Data shown are mean ± standard error of the mean of n = 6 mice. (C) Ultimate tensile strength (UTS) and % intact skin strength (secondary axis shown in red) of healed skin at Day 3 and 7 post wounding for LASE and LASE-His closed incisions. Data shown are mean ± standard error of the mean of n = 4 mice (n=6 for LASE day 7 p.w.). Statistical significance was determined using two-way ANOVA followed by Fisher's LSD test and individual p-values are shown and p-value < 0.05, which was considered statistically significant.

2.4 CONCLUSIONS

Tissue adhesives are an alternative and effective method of skin closure following surgical incisions, traumatic lacerations, etc. Here, we demonstrate the efficacy of silk fibroin-ICG based LASE for rapid sealing of skin incisional wounds in mice compared to conventional suturing. We evaluated healing outcomes at pre-determined timepoints based on skin barrier function recovery, skin mechanical strength recovery, and histological evaluated of healing skin. Our results indicate that skin defects sealed with LASE had earlier recovery of skin barrier function as depicted by lower transepidermal water loss rate at an earlier timepoint compared to suturing of incision. At the same timepoint significant improvement in healed skin strength recover was also observed. These are significant as better healed skin strength and barrier function can prevent dehiscence of wounds early in the healing period and susceptible to risk of surgical site infections. Histological analyses of healed skin at the end of the healing period in our study (day 7 post-wounding) showed no difference in epidermal gap and scar area compared to suture closed incisions which can be indicative of no excessive scarring or fibrosis in using LASE as a skin closure method. Addition of a bioactive along with LASE sealing further improved healing outcomes; enhancing skin tensile strength but no effect on transepidermal water loss due to addition of histamine was observed. Our findings suggest that LASE without or with the combination of right therapeutic bioactive can be a viable skin closure methods for rapid sealing and repair of incisional wounds. Also, additional large animal studies (porcine skin incisional model) will be helpful in evaluating the translation of LASE as a skin closure device for potential clinical use in the future.

CHAPTER 3: LIGHT-ACTIVATED TISSUE-INTEGRATING SUTURES AS SURGICAL NANODEVICES

3.1 INTRODUCTION AND BACKGROUND

Lacerations account for up to 12% of the visits to emergency care units every year in the United States alone, and sutures are still the primary choice of wound closure material in these cases(Zehtabchi et al., 2012). The surgical suture market was valued at $3.46 billion in 2016 and is anticipated to reach $5.84 billion globally by 2023. Simple interrupted or running sutures can be used for general tissue approximation in most clean wounds, depending on the location and dimension of the laceration. An ideal suture material demonstrates high and uniform tensile strength in tissue throughout the healing period, uniform diameter, sterility, ease of handling and knot security, minimal tissue reactivity and predictable performance(Al-Mubarak & Al-Haddab, 2013; Celeste & Stashak, 2008; Hussey & Bagg, 2011). However, despite widespread application, suturing does not create an immediate seal in approximated tissues, which can result in suture line leakages and infections(Schrock et al., 1973). Staples, adhesive tapes, bioinspired adhesives inspired by mussels, sandcastle worms and geckos(Bré et al., 2013), cyanoacrylate(Bruns et al., 1996; Singer et al., 2008) and fibrin glues(Currie et al., 2001; Gibble & Ness, 1990) have also been investigated for soft tissue repair. However, these devices are brittle, inhibit cell migration, and/or demonstrate low adhesion or strength, which limits their application to mostly superficial and low-tension lacerations(Dong et al., 2015; Jeon et al., 2015; Shapiro et al., 2001; Yeung et al., 2016).

Laser-activated tissue repair is an alternative approach for tissue approximation and anastomosis without the use of sutures, staples, or skin adhesives(Esposito et al., 2013; Hoffman et al., 2003; Urie, Ghosh, et al., 2018; Urie & Rege, 2015). In this approach, plasmonic nanoparticles(Huang et al., 2011), embedded in sealant biomaterials, absorb NIR laser light and convert it to heat, which causes tissue proteins to undergo local denaturation(Constantinescu et al., 2007; Matteini et al., 2007). Subsequent annealing is thought to facilitate the interdigitation of

tissue proteins and the sealant biomaterial. Studies on second-harmonic generation microscopy for visualizing laser-welded corneal stroma indicated three related processes: breakdown of interfibrillar proteoglycan bridges at 45-50°C, unfolding of proteins and contraction of fibrils at 55-60°C, and loss of protein network at temperatures higher than 80°C(Matteini et al., 2012). Spatiotemporal modeling enabled prediction of temperature profiles in tissues follower laser irradiation of the nanosealant; associated sealing strengths and potential tissue damage were also studied(Mushaben et al., 2018). A wide variety of sealant biomaterials including elastin-like polypeptides (ELPs), silk and collagen(Huang et al., 2013; Urie, Guo, et al., 2018a; R. Urie et al., 2015) can be interfaced with photothermal convertors, including gold nanorods (GNRs), for rapid sealing of soft tissues following laser activation. This approach can reduce operation and healing times, infection, and scarring compared to conventional modes of tissue repair(Khatri et al., 2011; Matteini et al., 2009; Sriramoju & Alfano, 2011) and can protect the tissue from desiccation and peripheral heat damage(Mushaben et al., 2018).

Motivated by the widespread use and surgeon compliance associated with sutures, here we describe the development of laser-activated tissue integrating sutures (LATIS) as novel nanodevices for soft tissue approximation and repair. These nanodevices were designed to synergize the benefits associated with conventional suturing with the added benefits of rapid sealing and tissue integration associated with laser-activated tissue repair. LATIS fibers were generated by incorporating gold nanorods within collagen, which is the principal structural component in tissues and is a key component in wound healing(Shoulders & Raines, 2009; Steinstraesser et al., 2010). Our studies demonstrate that laser activation of collagen-GNR fibers as LATIS nanodevices results in greater tissue integration, improved recovery of tissue mechanical properties, and faster repair and healing of acute wounds.

3.2 MATERIALS AND METHODS

3.2.1 Materials

Cetyltrimethyl ammonium bromide (CTAB), chloroauric acid trihydrate ($HAuCl_4.3H_2O$), ascorbic acid, sodium borohydride ($NaBH_4$), hydrochloric acid (HCl), and silver nitrate ($AgNO_3$) were purchased from Millipore Sigma (St. Louis, MO) for gold nanorods (GNRs) synthesis. Acetic acid (glacial), sodium chloride, sodium phosphate, sodium hydroxide, and citric acid were purchased from Millipore Sigma for collagen extraction and purification. All solutions were freshly prepared in nanopure water (resistivity ~ 18.2 MΩ-cm, Millipore filtration system, Darmstadt, Germany). To maintain reagent integrity: $HAuCl_4 \cdot 3H_2O$ was kept at 0°C, $NaBH_4$ and $AgNO_3$ solids were stored under vacuum, $HAuCl_4$ and $AgNO_3$ solutions were kept at 4°C, and CTAB solutions were maintained at ~30°C and 100 rpm. Other reagents were stored at room temperature. BALB/c mice were purchased at 6-8 weeks from Charles River Laboratories (Wilmington, MA, USA). Commercially-available 6-0 polyglycolic acid (PGA) sutures were purchased from CARA Life, Inc. (Rancho Cucamonga, CA) and 6-0 silk sutures from Ethicon (Edinburgh, United Kingdom). All suture sizes are reported based on those in the United States Pharmacopeia.

3.2.2 Rat tail tendon collagen extraction

Rat tails for tendon extraction were obtained from the ASU Department of Animal Care Technologies (DACT). Tendons were removed from humanely collected rat tails, and type 1 collagen was extracted by acid/pepsin solubilization(Habermehl et al., 2005; Kato et al., 1989; Navneeta et al., 2007). Briefly, the tendons were removed from the rat tail and washed in alternating solutions of 30% isopropanol (in nanopure water) and acetone three times. The washed tendons were air dried, cut into small segments and washed once in acetone. The tendons were stirred in 10% NaCl, then citrate buffer (pH 4.5), and then 0.05M Na_2HPO_4 (pH 9.0) all at 4°C for 24 hours in order to induce swelling and dissolve non-collagenous proteins. The swollen tendons were then dissolved in 0.5M acetic acid at 4°C for two days. Pepsin (50 mg /gm tendon) was added to the

solution, and the solution was stirred for another 48 hours. Collagen was precipitated by adding an equal volume of 10% NaCl, followed by centrifugation at 5,000g for 15 minutes. The collagen pellet was collected and re-dissolved in 0.5 M acetic acid. This salt precipitation was repeated two additional times. Finally, the collagen solution was dialyzed against 0.02M Na_2HPO_4 using a membrane with a MWCO of 10 kDa for 24 hours at 4°C. The purified collagen solution was frozen, lyophilized, and stored at room temperature until use.

3.2.3 Gold Nanorods (GNRs) Synthesis

GNRs were synthesized according to a seedless growth method, which results in the formation of gold nanorods stabilized by a cetyltrimethyl ammonium bromide (CTAB) bilayer(Ali et al., 2012; Huang et al., 2009; Nikoobakht & El-Sayed, 2003; Xu et al., 2014). Briefly, 5 mL of 1 mM $HAuCl_4.3H_2O$ were added to 5 mL of 0.2 M CTAB and gently mixed followed by addition of 8 µL of 12.1 M HCl (37% w/w). $AgNO_3$ (200 µL) was then added to this solution and gently mixed. Freshly dissolved ascorbic acid (70 µL of 78.8 mM) was added, and the solution was slowly mixed until it turned colorless. Cold $NaBH_4$ (15 µL, 10 mM) was then added immediately to this solution. The solution was incubated at ~30°C for 16-18 hours. This synthesis procedure results in GNRs that demonstrate a peak absorbance of ~800 nm, as determined by a Biotek Synergy 2 plate reader. The GNRs were centrifuged at 14,000 rpm for 10 minutes. The supernatant was discarded, and the pellet was dispersed in nanopure water to the desired concentration (this completes the first washing step). The GNRs were centrifuged and redispersed in nanopure water two additional times (two additional washing steps), bringing the concentration of free CTAB in the solution to less than 0.15 mM(R. Urie et al., 2015).

3.2.4 Generation of collagen-GNRs LATIS fibers

Lyophilized collagen was dissolved in 0.5 M acetic acid at a concentration of 20 mg/mL (2wt%). Concentrated GNRs were added to these viscous collagen solutions, resulting in 0.5 wt% GNR dispersions. Following GNRs addition, the collagen solution was rotated at 4°C for 24 hours

for homogenous mixing. Prior to extrusion, the collagen-GNRs solution was centrifuged at 3,000 rpm for 5 mins to remove any gas bubbles. The collagen-GNR dispersion was extruded thorough thin tubing into a 10% w/v polyethylene glycol (PEG)-10x PBS buffer solution using a syringe pump to obtain LATIS fibers(Ming-Che et al., 1994; Zeugolis et al., 2008). Briefly, a 5mL syringe (BD Syringes) connected to 8-12 inches of tubing was loaded onto a syringe pump (NE 300, New Era Pump Systems, Inc). The tubing inner diameter was 2.0 mm, and the pump was set to a flow rate of 0.75 mL/min. The tubing was then used to extrude the collagen-GNRs dispersion into a bath of fiber extrusion buffer (FEB) maintained at a pH of 7.6 and 37°C. FEB was composed of 110 mM phosphate-buffered saline (PBS) and 10 wt% poly(ethylene glycol) (PEG) (M_w 8000). Following extrusion, fibers were incubated in FEB for 20 minutes at 37°C and washed in a nanopure water bath for 10 minutes. The fibers were then hung and air-dried at room temperature under the tension of their own weight for at least 48 hours. Monofilament LATIS fibers were obtained by hanging and drying single extruded collagen-GNRs fibers. To obtain dual filament LATIS fibers, monofilament fibers were folded over themselves and hung to dry. Dried LATIS fibers were stored at room temperature until use.

3.2.5 Field Emission-Scanning Electron, Transmission Electron and Light Microscopy

Small sections of dry LATIS fibers were cut and placed on an aluminum stub using carbon tape and coated with Au/Pd in a high-vacuum coater for 60 seconds at a 2-Amp current. The estimated coating thickness was 3 nm. Scanning electron microscopy (SEM) was performed with a PHILIPS FEI XL-30 SEM microscope. Similar LATIS sections were soaked overnight in epoxy resin. Thin slices of the cured epoxy-containing sample were sectioned using an ultramicrotome. These thin samples were images using a Philips CM 12 transmission electron microscope. Fiber dimensions and uniformity were determined using an Axio Observer (Zeiss) light microscope. Six images were taken at random along the length of each 2 mm fiber, and the diameter was calculated as the average of these six measurements. SEM and TEM images were acquired by Dr. Karthik

Pushpavanam Subramaniam, then fellow Ph.D. student in Rege Bioengineering Lab and also helped with analyzing the images.

3.2.6 Tensile strength of LATIS

Tensile strength measurements of LATIS fibers was performed using a TA.XT Plus Texture Analyzer (Texture Technologies Corp., Hamilton, MA) in uniaxial tension mode equipped with Exponent (Stable Microsystems) software. Five-centimeter-long suture fragments (n=7 for monofilament LATIS, dual filament LATIS, and control 6-0 PGA suture) were clamped vertically and force from a 2-N load cell was applied to stretch the sample at a rate of 2mm/s in uniaxial tension mode until failure, referred to as ultimate tensile strength (UTS).

3.2.7 Photothermal response of LATIS

A Millennia eV 5W titanium sapphire (Spectra-Physics) laser tuned to 800 nm wavelength and configured in continuous wave (CW) mode with a red HeNe guide beam was used for photothermal response studies. The laser spot size was tuned to a diameter of 1.5 mm. The power density was calculated as the power/area of exposure using a FieldMate laser power meter (model number #S-1544, Coherent Inc.). An A325sc infrared camera (FLIR, Nashua, NH) with 10mm 45º lens measured the surface temperature of the fiber during laser exposure. Five cm sections of LATIS fibers were placed on a glass slide and exposed to laser power densities ranging from 1.6 to 4.8 W/cm^2 for 60-second durations, for 3 cycles in which the laser was turned on for 15 seconds ("on" cycle) and off for 5 seconds ("off" cycle). The IR camera was used to measure the temperature prior to laser treatment for 5 seconds and following laser treatment for 10 seconds. Infrared (IR) images were recorded at 1-second intervals and were analyzed to determine the maximum surface temperature at the center of the laser exposure area. Similar measurements were repeated for PGA and silk sutures, and their photothermal response upon laser irradiation was collected.

For studying the photothermal response of LATIS fibers on skin, LATIS fibers were sutured into cadaveric BALB/c mice skin. The laser was irradiated onto the suture line from one side, while

IR images of the skin-LATIS interface were captured. This configuration allowed for capture of the temperature of the fibers during laser exposure at the surface of the laser exposure, as well as opposite to the laser exposure at the segment of the suture knots that transverse the skin.

3.2.8 Differential scanning calorimetry

Differential scanning calorimetry (DSC) was carried out in order to determine the phase transition and thermal decomposition of collagen in LATIS in the laser operating range using a DSC 2500 (TA Instruments). Hermetic aluminum pans were filled with 3-5 mg of LATIS fragments and scanned at a heating rate of 5°C/min from 5°C to 90°C under nitrogen atmosphere (purity 99.99%, flow: 20 mL/min). A hermetically sealed empty pan was used as a reference. The measurements were repeated 3 times for each sample. DSC program and measurements were acquired by Dr. Samrat Amin at Magnetic Resonance Research Center (ASU core research facilities).

3.2.9 Drag force of LATIS with and without laser treatment in tissue

The drag force exerted by LATIS during suturing in murine skin was measured using a TA.XT Plus Texture Analyzer. A rectangular section of murine cadaver skin (5 cm x 5 mm) was held horizontally by clamps, and LATIS was pulled thorough the skin at a crosshead speed of 10 mm/second until 10 cm of the suture passed thorough the skin. Drag force on the tissue was determined from the maximum force (F) exerted per area of the tissue sample (A), represented as drag force/normalized tissue area (σ, kPa). Similar measurements were also determined using PGA 6-0 commercial sutures for comparison. Drag force measurements are displayed as mean ± standard deviation from seven independent experiments.

To study the effect of laser irradiation on LATIS-tissue interface and resulting drag force, 1cm incision on mouse cadaver skin were closed using PGA, silk, and LATIS in a continuous suturing fashion. The suture-tissue interface was irradiated with the laser at a rate of 0.5 mm/second for 2 minutes at 2.4 W/cm^2 in all groups. The free end of the suture was pulled thorough the skin using the above-mentioned procedure and maximum force (F) exerted per area of tissue

sample (A) to pull the total length of the suture out of the incision indicated the additional drag on the tissue post laser treatment. (σ, kPa). This was represented as drag force/normalized tissue area (σ, kPa).

3.2.10 Hemocompatibility and cytotoxicity of LATIS

Whole porcine blood with sodium citrate as anticoagulant (Lampire Biological Laboratories, PA) was used to test the hemolytic activity of suture samples based on a previous protocol(Singh et al., 1990). Briefly, single strands of all suture types (sufficient to close a 1-cm incision with four simple interrupted knots and weighing ~6 mg) were incubated in 0.5 ml whole porcine blood. After 10 min., 4 ml of 0.9% NaCl solution was added to each sample to stop hemolysis, and the samples were further incubated for 60 minutes at 37°C. Positive and negative controls were prepared by adding 4 ml of nanopure water (NPW) and 0.9% NaCl solution to whole blood. Samples were centrifuged at 1500 rpm for 10 minutes and the supernatant was measured at 545 nm. The % hemolysis for samples were calculated as:

$$\%\ \text{Hemolysis} = \frac{(\text{Sample Abs} - \text{Negative Control Abs})}{(\text{Positive Control Abs} - \text{Negative Control Abs})} \times 100$$

All % hemolysis is displayed as mean ± standard deviation from three independent experiments (n=3).

Cytotoxicity of LATIS and other suture types were evaluated using direct-contact test based on ISO 10993-5 – Tests for *in vitro* cytotoxicity guidelines. Murine fibroblast cell line (NIH 3T3, ATCC® CRL-1658™) and human fibroblast cell line (BJ-5ta, ATCC® CRL-4001™) were seeded onto 24 well plate at a concentration of 25,000 cells/well and were allowed to attach overnight. Cells maintained in DMEM media containing 10% fetal bovine serum (FBS) and 1%penicillin-streptomycin (PS) were treated with single strands of sutures (weighing ~ 6mg) for 24, 48 and 72 hours by incubating at 37°C. Cell viability was assessed using the spectrophotometry based MTT assay. Briefly, 100 µL of the MTT reagent was added to the cells and incubated for 3h at 37°C, following which 500 µL dimethyl sulfoxide: methanol (1:1) was added and further incubated at room temperature for 30 min in a shaking incubator. The 570 nm measures absorbance of formazan

crystals and 670 nm absorbance takes into consideration any noise from sutures and cell debris. Finally, the noise values were subtracted from 570 nm absorbance values, which were then used to measure % cell viability. Control wells were cells and media without sutures.

$$\%\ \text{cell viability} = \frac{(\text{Test Abs})}{(\text{Control Abs})} \times 100$$

All % cell viability are displayed as mean ± standard deviation from three independent experiments (n=3).

3.2.11 Murine dorsal skin incision model

BALB/c mice (8-12 weeks) (Charles River Laboratories, Wilmington, MA, USA) were used in a dorsal skin incision model in strict accordance with The Guide for the Care and Use of Laboratory Animals of the National Institutes of Health. Animal procedures were approved by the Arizona State University Institutional Animal Care and Use Committee (protocol 15-1428R) and conducted according to relevant national and international guidelines. Before surgery, each mouse was anesthetized with 120mg/kg ketamine and 6mg/kg xylazine by intraperitoneal injection. The hair was clipped and prepped with chlorhexidine gluconate and alcohol. Two 1-cm, full-thickness skin incisions side-by-side on the back of each animal were spaced 1 cm apart. Incisions were closed using 4 interrupted knots of LATIS sutures. The suture line was irradiated with the laser being scanned along the suture line at a rate of 0.5 mm/second for 2 minutes at 2.4 W/cm^2, at an angle between 60 and 80° from the skin, corresponding to temperatures not exceeding 60°C on the LATIS-skin surface. Additionally, skin incisions were also closed using LATIS without laser irradiation or closed with silk or PGA 6-0 sutures. For comparison, the left incision on each mouse was closed using commercial silk or PGA 6-0 sutures, and the right incision was closed using LATIS with or without laser. The mice were recovered on a heating pad until fully mobile and then housed individually to prevent suture removal. The incision healing was assessed 3 days after surgery. Adverse signs such as inactivity, inability to eat or drink, emaciation, gross infection, or wound dehiscence required an animal be removed from the study. Mice were euthanized by CO_2 inhalation followed by cervical dislocation.

3.2.12 Healed skin tensile strength

Immediately following euthanasia, rectangular sections of the skin around the incision area (2 x 1 cm, measured by calipers after underlying fascia removal) were excised. Sutures were removed to measure the strength of the tissue alone. Skin samples were stretched until failure at a rate of 2 mm/sec using a TA.XT Plus texture analyzer. Ultimate tensile strength (UTS) of the healed skin was determined from the maximum force of the tissue from the healed area prior to failure, where the maximum force (F) and area of the tissue sample (A) determined the ultimate tensile strength (σ, kPa) of the sutured skin ($\sigma = F/A$). The tensile strength of intact skin (with no incision) was also tested for comparison. All tensile strengths are displayed as mean ± standard deviation from nine independent experiments (n=9). Tensile strength recovery for skin samples were calculated as a difference between ultimate tensile strength for each group after 3 days from native skin strength, with the difference then converted to a percentage.

3.2.13 Histologic and morphometric analysis

Following euthanasia, the wound tissue was excised together with surrounding tissue and fixed in 10% formalin solution (Scigen) for 72 hours. Tissue samples were processed routinely, embedded in paraffin blocks and then sliced into 5 µm-thick sections. Sections were stained with hematoxylin and eosin (H&E) and Masson's trichrome. A board-certified veterinary pathologist, blinded to sample source, read and analyzed the slides for evidence of healing, inflammation, and collagen incorporation. The extent of bridging at the incision site, inflammation, collagen deposition, and epidermal thickness, were assessed in a blinded manner according to a semi-quantitative scoring system: – (absent), + (minimal), ++ (mild), +++ (moderate), and ++++ (marked)(Gal et al., 2008). Skin samples from three independent experiments were collected and submitted for histological examination. The thickness of epidermis was measured vertically from the basement membrane to the most superficial layer of epidermis at six equidistant places around the wound site. Measurements were taken from four different tissue sections and average thickness was

calculated in μm(Malinda et al., 1999)(Fig. 5). Tissue processing, embedding, sectioning and embedding were performed by Ms. Polina Aukon at the Pathology core laboratory facility at Midwestern University.

3.2.14 Statistical Analyses

All results are presented as mean ± standard deviation (SD). Statistical analyses were performed using one-way analysis of variance (ANOVA) followed by post hoc Tukey HSD Test for pairwise comparison (Prism 7, GraphPad Software). A p-value < 0.05 was considered statistically significant.

3.3 RESULTS AND DISCUSSIONS

3.3.1 Generation and Characterization of Laser-Activable Tissue-Integrating Sutures

An aqueous dispersion of GNRs, 41 ± 7 nm in length and 11 ± 2 nm in diameter, was generated in order to tune the peak absorption wavelength to ~800 nm, which is in the near infrared (NIR) region of the spectrum(Huang et al., 2011; Mackey et al., 2014). Concentrated GNRs were added to viscous collagen solution (20 mg/mL or 2wt% in 0.5 M acetic acid) and mixed homogenously, resulting in the formation of collagen-GNR dispersion. There is negligible change in the absorbance peak wavelength of GNRs in dispersion and in the collagen matrix, indicating minimal aggregation of GNRs (Figure 3-1A). LATIS monofilament or dual filament fibers, ~30 cm in length, uniform in diameter (Figure 3-1B) were generated from the collagen-GNR matrix using a polymer wet extrusion method(Zeugolis et al., 2008) (Figure 3-1C). Scanning electron microscopy (SEM) images show that the mean diameter of LATIS fibers is ~130 μm (Figure 3-1D), which is similar to the diameter of 6-0 collagen suture(Greenberg & Clark, 2009). GNRs are homogenously distributed throughout the LATIS fibers as seen in TEM micrographs (Figure 3-1E)

.

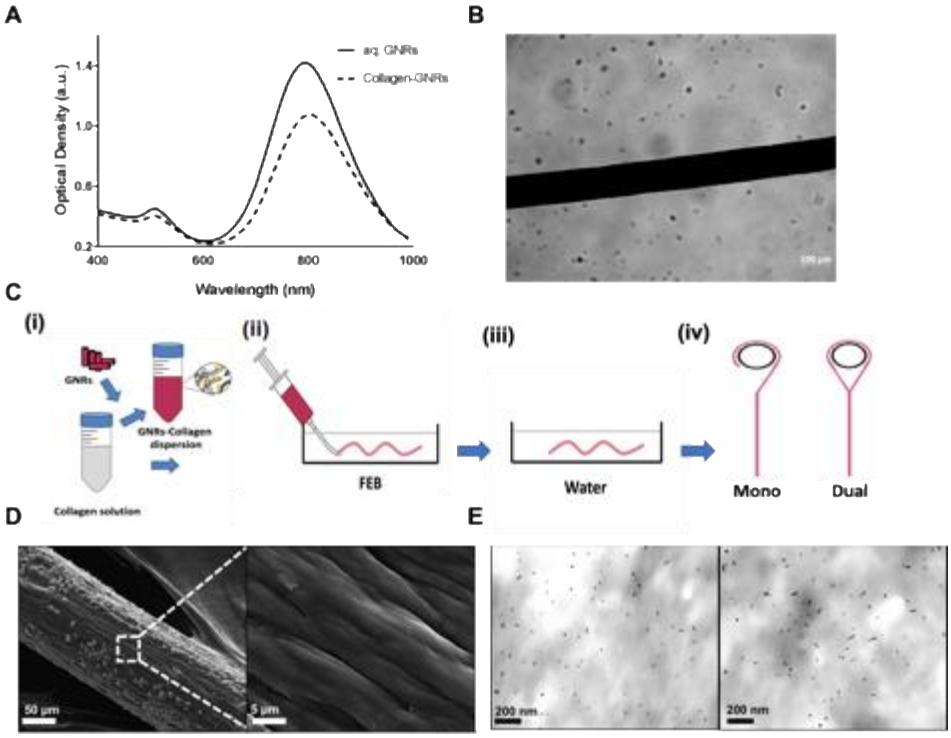

Figure 3-1. Fabrication and physical characterization of light-activated tissue-integrating sutures (LATIS).

(A) Absorbance spectra of dispersion of GNRs in nanopure water and collagen (20mg/ml concentration dissolved in nanopure water) at RT. (B) Light microscope image of LATIS showing the fiber dimension and uniformity (100 μm scale bar). (C) Synthesis procedure of LATIS fibers (i) GNRs were added to a 20 mg/ml collagen solution (in 0.5 M acetic acid diluted in nanopure water) and a homogenous collagen-GNR (0.5 wt%) dispersion was obtained (ii) Collagen-GNR dispersion was extruded into fiber extrusion buffer (FEB) maintained at 37°C and the extruded fibers were incubated for 20 minutes (iii) Fibers were washed in nanopure water three times post incubation in order to remove any excess buffer (iv) The fibers were then hung and air-dried at room temperature under the tension of their own weight for at least 48 hours. Monofilament fibers were folded over themselves and dried to obtain dual filament fibers as shown in the schematic. (D) Representative field emission-scanning electron microscopy (FE-SEM) images of LATIS acquired at an accelerating voltage of 10 kV (scale bar = 50 μm). Magnified inset of the surface of LATIS (scale bar = 5 μm). The location of the inset indicated in (D) is approximate. (E) Representative TEM image of LATIS sections showing the uniform distribution of GNRs at the LATIS surface (left) and core (right).

Monofilament and dual-filament LATIS fibers demonstrated ultimate tensile strengths (UTS) of ~5 and 6 kPa, respectively, which were comparable to that of commercial USP size 6-0 polyglycolic (PGA) sutures (8 kPa) of comparable diameter (Figure 3-2A). Surface temperatures of LATIS fibers irradiated with continuous-wave (CW) laser at 800 nm increased with increasing laser power densities, which ranged from 1.6 to 4.8 W/cm^2. Typically, temperatures in the range of 55-65°C are necessary for laser-activated tissue sealing, and temperatures of 55-60°C are considered optimal(Mushaben et al., 2018). These sealing temperatures were easily attained by modulating the laser power intensity. Temperature increase occurred rapidly and quickly reached a maximum following laser irradiation during the 15 S “on” cycle. The temperature rapidly dropped to room temperature (baseline) as soon as the laser was switched off. This behavior was reproducible across multiple cycles and different laser powers. Monofilament LATIS failed to yield optimal sealing temperatures at power densities of 1.6-4.8 W/cm^2 (Figure 3-2B). However, in case of dual filament fibers, optimal temperatures were reached and maintained at laser power densities of 2.4 W/cm^2 (Figure 3-2C). The higher photothermal response of dual filament LATIS can be attributed to higher amount of GNRs present per unit area at a given spot in dual filament LATIS. Laser irradiation of commercial PGA sutures did not show any increase in temperature over baseline levels. These results show that GNRs in the sutures act as photoconverters of NIR light, which is a key requirement for laser-activated tissue approximation and repair. Taking their higher tensile strengths and lower power densities required to obtain desired photothermal response into consideration, dual filament fibers were used in subsequent studies. LATIS fibers demonstrated a robust photothermal response when used as sutures in mouse cadaver skin; increasing laser power densities resulted in higher temperatures, but the heat was localized to the spot of laser irradiation along the suture line (Figure 3-2D-G, indicated using white arrows). Optimal sealing temperatures could be reached on the cadaver skin by modulating the laser power.

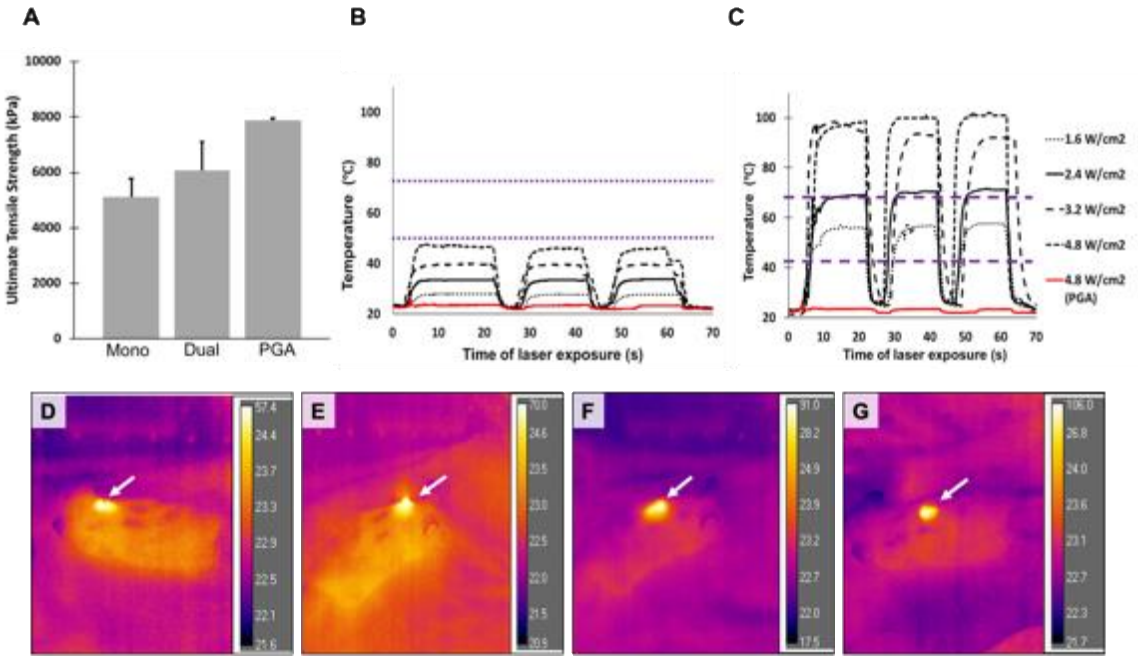

Figure 3-2. Ultimate tensile strength and photothermal response of LATIS.
(A) Ultimate tensile strength (UTS) of LATIS and PGA sutures (CARAglyde, CARALife, Inc.). Monofilament and dual filament collagen–GNR LATIS fibers demonstrated ≈63% and ≈75% tensile strength compared to PGA sutures, respectively. (B, C) Photothermal responses of monofilament and dual filament LATIS fibers following exposure to 800 nm continuous wave (CW) laser for 1 min at power densities from 1.6 to 6.4 W/cm2 in a 15 s “on” and 5 s “off” cycle (3 cycles total). The response of the PGA sutures to irradiation with 6.4 W/cm2 laser (800 nm) is indicated by a red line. Each curve is representative of six different experiments. (D - G) Representative infrared (IR) thermal camera images of the photothermal response of LATIS sutured onto cadaver murine skin, following NIR laser irradiation at increasing power densities from 1.6 to 4.8 W/cm2. The temperature increase is confined around the suture line.

Differential scanning calorimetry (DSC) analysis indicated that LATIS fibers are stable between 5°C to 90°C, with a characteristic denaturation peak for the triple helical structure of collagen at 54°C(Miles & Burjanadze, 2001; Zeugolis & Raghunath, 2010) (Figure 3-3A). No distinct change in LATIS behavior was observed in any of three cycles studied indicating that they are stable over multiple thermal cycles and will allow multiple laser scans over the suture line for

efficient sealing. Rheological studies carried out over a wide range of temperatures facilitate a deeper understanding of the behavior of LATIS at physiological as well as elevated temperatures that are attained during laser induced tissue sealing applications. A significant decrease in complex shear modulus (G*) of collagen and collagen-GNRs matrices was observed between 45°C and 55°C (Figure 3-3B). These temperature-induced changes in collagen are anticipated to enhance conventional suturing and facilitate rapid tissue integration.

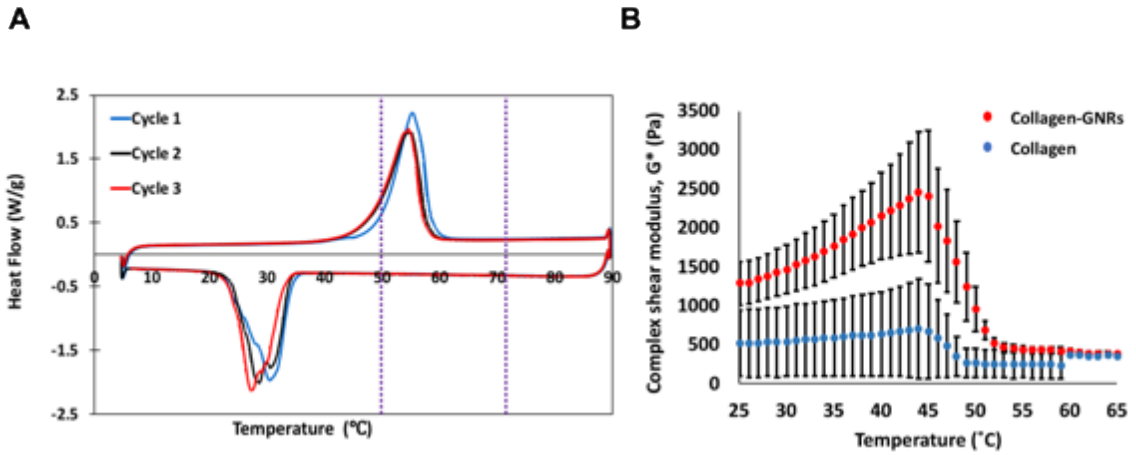

Figure 3-3. Thermal stability and rheological behavior of LATIS.
(A) Thermal stability of LATIS fibers, determined using differential scanning calorimetry (DSC), in laser-induced temperature operating range. LATIS fibers are stable between 5°C to 90°C, with a characteristic denaturation peak for the triple helical structure of collagen at around 54°C. LATIS fibers were fairly stable in the laser operating range of 50°C to 70°C (shown by purple dashed lines). The thermal cycle was repeated three times in the same conditions and there was no distinct change in LATIS behavior observed in any of the subsequent cycles. (B) Rheological behavior of collagen-GNR matrix showing complex shear modulus as a function of temperature. Curves are representative of n = 3 independent experiments.

3.3.2 Suturing Performance of LATIS

Maintaining tissue trauma to a minimum aids faster healing, and the goal throughout surgery is to cause minimum trauma to the wound edges and underlying tissue and blood vessels(Dunn & Phillips, 2007). Judicious choice of sealing materials facilitates minimal trauma to the tissue during the suturing process. The drag force required to pull the sutures thorough a unit

area of mouse skin tissue was comparable (~38 kPa) for commercial PGA sutures (CARAglyde) and LATIS fibers (Figure 3-4A). Thus, LATIS fibers are not likely to cause higher trauma to tissue during suturing than that seen with existing sutures. Incomplete or poor healing, which can result in wound dehiscence, can also be a result of dead space left in the wound area, which is caused by inadequate tension or poor approximation of the wound edges during suturing(Dunn & Phillips, 2007). Greater force was required to remove laser-irradiated LATIS fibers from the wound compared to that needed for PGA or silk sutures (p-value <0.0001), which indicated better integration of the LATIS fibers with the tissue (Figure 3-4B); all sutures were subjected to similar levels of laser irradiation. The phase transition in collagen brought about by the localized increase in temperature likely facilitates better integration of the sutures with the tissue following annealing, resulting in greater suture integrity in the approximated tissue. Irradiating a light-activated suture line can facilitate better integration with tissue and more efficient approximation of wound edges, leading to accelerated tissue repair and healing.

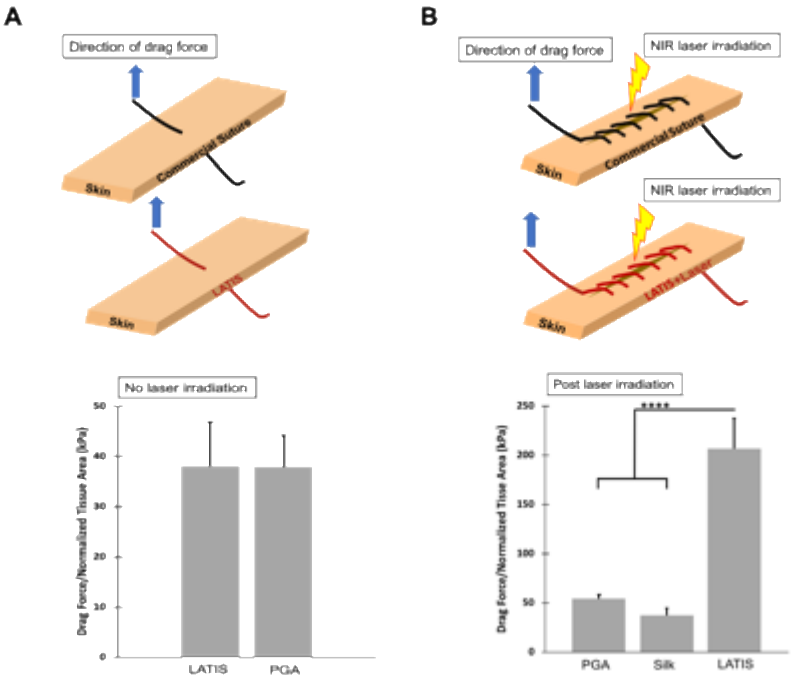

Figure 3-4. Suturing performance of LATIS in murine cadaver skin.
A) Drag force of LATIS thorough mouse cadaver skin shows no significant increase in tissue drag compared to PGA suture. Data shown are mean ± standard deviation (SD) of n = 7 experiments. Statistical significance was determined using unpaired t-test with Welch's correction (t = 0.034, degree of freedom = 10.96, p-value = 0.45) followed by Tukey HSD Test. **p < 0.01, ***p < 0.001, ****p < 0.0001. B) Drag force of sutures thorough mouse cadaver skin following laser irradiation indicating greater tissue integration/security in the LATIS group compared to PGA and silk groups; all groups were irradiated laser at a rate of 0.5 mm/s for 2 min at 2.4 W/cm2 in this study. Data shown are mean ± standard deviation of n = 3 experiments. Statistical significance was determined using one-way ANOVA (F value =60.46, degree of freedom = 8) followed by Tukey HSD Test. *p < 0.05, **p < 0.01, ***p < 0.001, ****p < 0.0001.

3.3.3 Hemocompatibility and biocompatibility of LATIS

Hemolysis assay was conducted with all suture types using porcine whole blood to evaluate their hemolytic activity (Figure 3-5A). LATIS exhibited very low hemolytic activity (% hemolysis) towards erythrocytes present in whole porcine blood. Hemolytic activities for LATIS, PGA sutures, and silk sutures were 0.44%, 0.69% and 0.60% respectively compared to fully hemolyzed positive control. (Figure 3-5B). Conventionally, blood-contacting materials which result in less than 2% hemolysis are considered as non-hemolytic (Weber et al., 2018). In addition, exposure of LATIS and commercially available PGA and silk sutures to NIH 3T3 and BJ-5Ta cell lines did not result in significant loss of cell viability at different time intervals (24, 48 and 72 h: Figure 3-5C). We also investigated collagen-only sutures (i.e., collagen fibers without GNRs) in the cytotoxicity assay. After exposure for 72 h, the cytotoxicity induced by LATIS was not statistically significant from that seen with commercially available PGA and silk sutures as well as sutures made from collagen alone, indicating that GNRs present in the LATIS fibers did not result in cell toxicity. Taken together, these results indicate that the collagen-GNR LATIS fibers are likely as biocompatible as commercially available silk and PGA sutures.

A

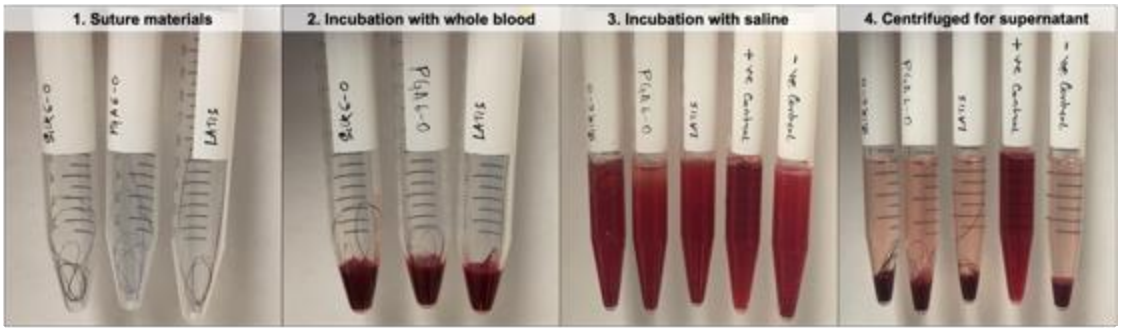

B

Sample	% Hemolysis
Positive Control	0
Negative Control	100
PGA suture	1.01 ± 0.29
Silk suture	0.15 ± 0.05
LATIS	0.36 ± 0.09

C

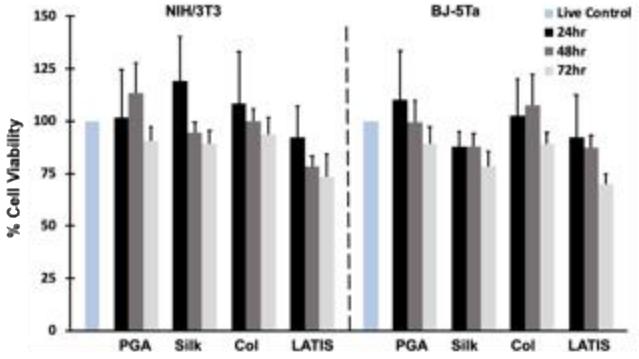

Figure 3-5. Hemocompatibility and biocompatibility of LATIS.
(A) Representative images of hemolytic activity of LATIS compared to commercial PGA and silk suture. (B) Hemolytic activity (% hemolysis) of each suture type. Hemolytic activity of LATIS was comparable to PGA and silk suture and within range of nonhemolytic biomaterials. Data indicate mean ± standard deviation of n = 3 experiments. (C) Cytotoxicity (% cell viability) of each suture type exposed to NIH/3T3 and BJ-5Ta cell lines at 24, 48, and 72 h time point. Data indicate mean ± standard deviation of n = 3 experiments. Col indicates collagen fibers (sutures) without GNRs.

3.3.4 Light-Activated suturing of soft tissues

Ineffective skin sealing following spine surgeries can lead to significant complications including surgical site infections and wound dehiscence(Yao et al., 2018). In order to investigate the efficacy of skin sealing in an animal model with incisions similar to those in spine surgeries, full-thickness dorsal skin incisions, 1-cm in length, were made in BALB/c mice and closed with PGA sutures (Figure 3-6A), silk sutures (Figure 3-6B), LATIS alone (Figure 3-6C) and LATIS irradiated

with 2.4 W/cm^2 laser (Figure 3-6D). Laser irradiation resulted in a discernible change in LATIS morphology in the skin likely due to phase changes in collagen induced by the localized heating, which ultimately resulted in fusion of individual suture strands (Figure 3-6I top right, yellow arrows). This can lead to more effective approximation of wound edges, maintenance of tension, and greater suture integrity within the tissue. Such fusion was not observed for LATIS fibers not irradiated with laser light (Figure 3-6I top left, blue arrows) or for the other sutures used in the study.

Three days following surgery, the skin appeared to have completely closed and healed with silk sutures, LATIS and LATIS+Laser, but was only partially closed with PGA sutures (Figure 3-6 E-H). Incisions closed with PGA suture, silk suture and LATIS without laser irradiation resulted in skin tensile strengths of 50 ±12, 62 ±13, and 62.8±15 kPa, respectively (Figure 3-6J). Laser irradiation of the LATIS fibers (LATIS+laser) resulted in closure of the incision (Figure 3-6H) and yielded the highest skin tensile strength 101.3±13 kPa (Figure 3-6J), which was statistically significant when compared to every other group: PGA (p-value <0.001), silk (p-value = 0.0017) and LATIS alone without laser irradiation (p-value = 0.0028). These wounds also showed a marked reduction in gaps between tissue edges as observed visually. The tensile strength of intact mouse tissue without any incision was measured to be 188 ±50.2 kPa and used as a control to measure recovery in case of the different suture groups. After a 72-hour healing period, PGA sutures resulted in lowest recovery of ~27% of that of intact skin (Figure 3-6J, secondary axis). Silk sutures on the other hand resulted in a 33% recovery in strength, which was similar recovery to that seen with LATIS suturing in absence of laser irradiation (34% recovery). However, laser irradiation of LATIS fibers resulted in tensile strength recovery of approximately 54% of that of native skin (Figure 3-6J). The LATIS+Laser treatment improved tissue approximation likely because of greater integration with the tissue as indicated by the drag force studies shown in Figure 3-4B. This greater integration is likely responsible for the significant enhancement in biomechanical properties and indicate benefit of using light-activated sutures that can combine physical approximation with photothermal sealing.

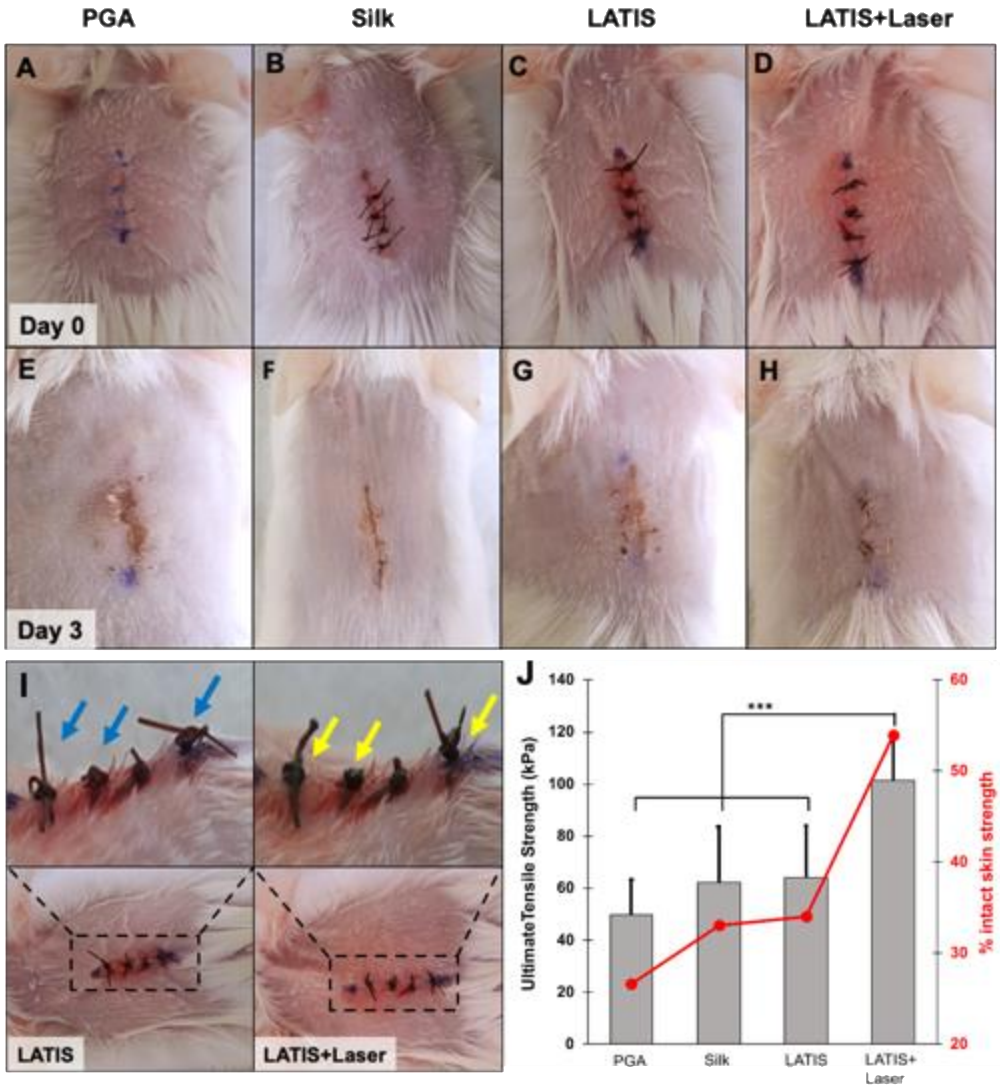

Figure 3-6. Representative images of 1-cm dorsal skin incision in BALB/c mice at Day 0 and 3 post wounding.

(A-C) Representative images of incisions closed with four interrupted knots made using PGA, silk, and LATIS sutures. (D) Incision was closed with four interrupted knots of LATIS followed by irradiation with an 800 nm laser, power density 2.4 W/cm^2 at a rate of 0.5 mm/s for 2 min. (E-H) Representative images of skin after suture removal in BALB/c mice following the healing period (three days) post-surgery. (I) Magnified image of the LATIS and LATIS + Laser suture line showing individual suture strands after skin closure and temperature-induced fusion of individual suture strands, respectively. (J) Ultimate tensile strength and strength recovery plot of healed skin three days following surgery compared to intact skin. LATIS + Laser resulted in the highest skin tensile strength and % recovery (secondary axis) compared to PGA, silk, and LATIS without laser irradiation groups. Data shown are mean ± standard deviation of n = 9 experiments. Statistical significance was

determined using one-way ANOVA (F value = 23.67, degree of freedom = 32) followed by Tukey HSD Test. ****p < 0.0001, ***p < 0.001.

Histological analyses of the incision closed with PGA sutures indicated that epidermis was almost fused at the site, but complete re-epithelialization was not achieved (Figure 3-7A). The epidermis layer was 3-5 cells thick and covered with serocellular crust, a small number of neutrophils, degenerate leukocytes, fibrin and cellular debris. Moderate numbers of neutrophils were intermingled with fibrous connective tissue. The dermis and the adipose tissue had moderate numbers of neutrophils, but fewer lymphocytes or macrophages (Figure 3-7A, E). Cross-section of the incision site revealed that the suture material was surrounded by degenerate leukocytes, neutrophils, and necrotic material. Together, these results indicate that PGA sutures likely elicit minimal foreign body reaction in the wound, which is along expected lines. In case of incisions closed with silk and LATIS fibers (in absence of laser irradiation), the incision site was connected with immature fibrous connective tissue and the epidermal layer is 4-6 cell layer thick, covered with degenerate leukocytes, and with fibrin and cellular debris in both cases. (Figure 3-7B, C). A moderately higher number of neutrophils were found together with fibrous connective tissue in wounds closed with silk sutures (Figure 3-7B) compared to those approximated with LATIS fibers in absence of laser irradiation (Figure 3-7C). The dermis and the underlying adipose tissue also contained moderate numbers of neutrophils, but only a few lymphocytes and macrophages. The dermis and the subcutis layers of wounds closed with silk suture showed a mildly higher deposition of connective tissue matrix and collagen compared to those closed with LATIS fibers in absence of laser irradiation (Figure 3-7F, G). The silk suture material located at subcutis, was surrounded by macrophages, lymphocytes, neutrophils and immature fibrous tissue with a small amount of necrotic material. Incisions closed with silk showed a minor inflammatory reaction, which is characteristic of silk as a biomaterial (Selvig et al., 1998; Soong & Kenyon, 1984; Yaltirik et al., 2003), but no severe reaction was observed. LATIS was barely removed from the incision site and was surrounded by a large number of degenerate leukocytes, neutrophils and necrotic material.

Incisions closed with LATIS fibers and followed by laser irradiation were completely fused with immature fibrous connective tissue and a well-formed hyperplastic epidermis at the wound site. The epidermis was 4-8 cells thick and covered with serocellular crust, a small number of neutrophils, degenerate leukocytes, fibrin and cellular debris (Figure 3-7D). The dermis and adipose tissue region contained moderate numbers of neutrophils, a small number of lymphocytes and macrophages similar to the LATIS group not subjected to laser irradiation. Moderate amounts of collagen deposition were observed at the dermis and subcutis around the incision line, which, in turn, depicted positive healing response post injury (Figure 3-7H). Additionally, the increased collagen deposition, as indicated by Masson's Trichrome (MT) stain, may also help preserve the structural integrity of the wound, which can enhance the mechanical strength of the healing tissue. The suture material in the tissue was surrounded by inflammatory cells including macrophages and lymphocytes, and necrotic material was present in abundance around the suture site as compared to other groups. The suture material was slightly removed by inflammatory cells. Presence of macrophages and lymphocytes around the LATIS fibers, with and without laser irradiation, is characteristic of inflammatory response of collagen suture material to facilitate absorption of suture material in wounds(Selvig et al., 1998).

During wound closure, the epidermis becomes highly stratified, and increase in epidermal thickness is an important indicator of wound healing(Alemdaroğlu et al., 2006; Malinda et al., 1999). Morphometric analysis of histological sections showed that the increase in the epidermal thickness was highest for the LATIS+Laser group compared to that seen for incisions approximated with PGA (p-value <0.001), silk (p-value <0.001) and LATIS fibers without laser irradiation (p-value <0.001) (Figure 3-7I). Taken together with histological results, the epidermal thickness results indicated rapid tissue healing in case of wounds approximated with LATIS fibers and irradiated with NIR lasers compared to other groups.

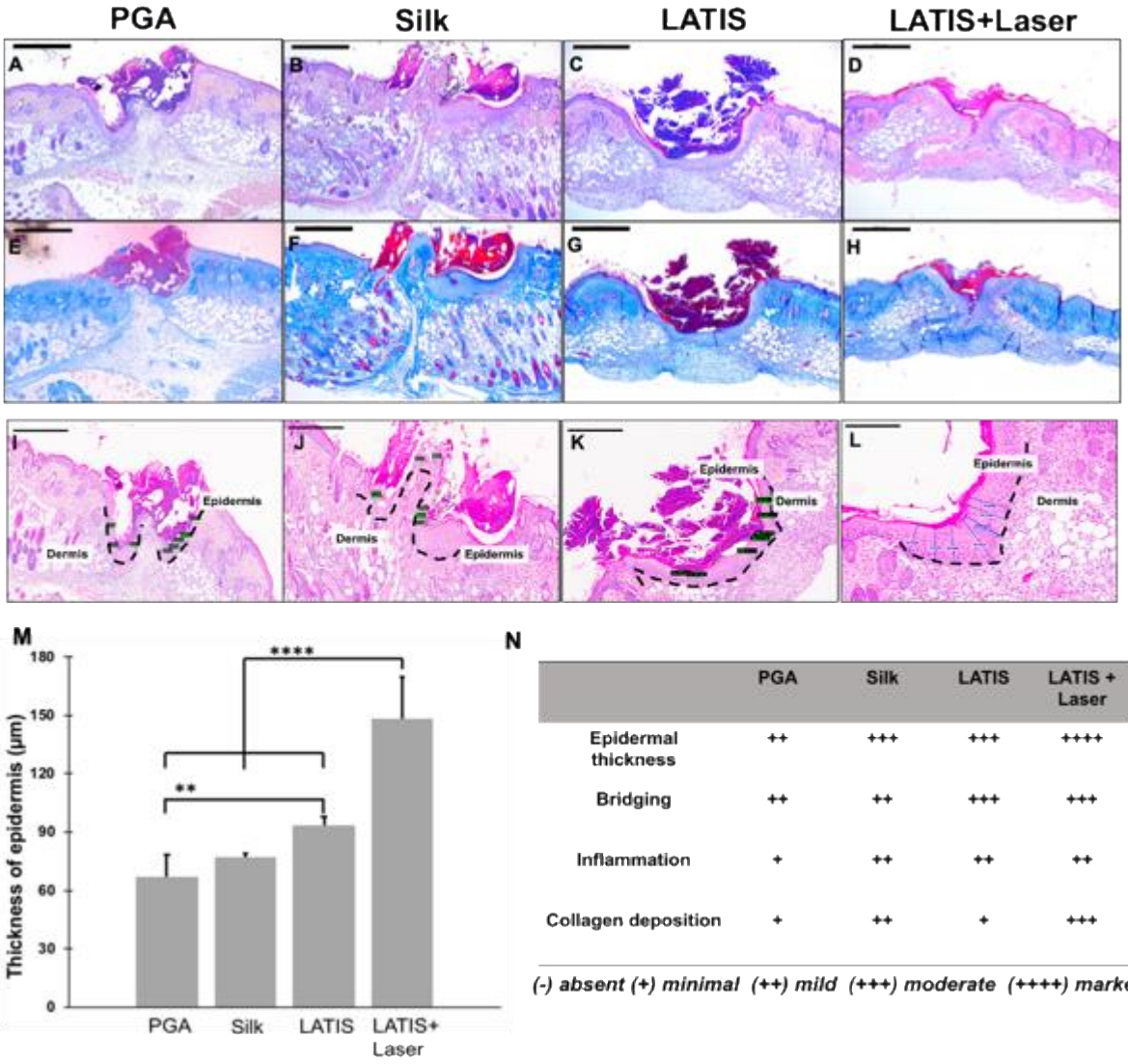

	PGA	Silk	LATIS	LATIS + Laser
Epidermal thickness	++	+++	+++	++++
Bridging	++	++	+++	+++
Inflammation	+	++	++	++
Collagen deposition	+	++	+	+++

(-) absent (+) minimal (++) mild (+++) moderate (++++) marked

Figure 3-7. Analysis of healed tissue at day 3 post wounding.
(A-D) Representative digital images of hematoxylin and eosin (H&E) stained tissues. Wound edge of LATIS + Laser group is completely fused with immature fibrous connective tissue and fusion of the hyperplastic epidermis (scale bar = 500 µm). (E-H) Representative digital images of Masson's trichrome stained tissues (scale bar = 500 µm). Multiple layers of hyperplastic epidermis are identified at the wound site of LATIS + Laser group and a greater amount of collagen deposition is observed compared to other suture groups. (I-L) Representative histological images of hematoxylin and eosin stained tissues showing regenerated epidermis at the wound site (shown with black dotted line). (M) Quantification of thickness of epidermis around the wound site among various suture groups. The epidermal thickness in LATIS + Laser group was higher compared to the other groups. Data indicate mean ± standard deviation of n = 6 experiments. Statistical significance was determined using one-way ANOVA (F value = 10.49, degree of freedom = 35) followed by Tukey HSD Test. ****$p < 0.0001$, **$p < 0.01$. (N) Results of the semiquantitative assessment of selected healing parameters at the wound site

3.4 CONCLUSIONS

Lacerations and incisional wounds are approximated using sutures, glues or staples leading to healing by primary intention. Well approximated wounds heal in shorter periods of time, which can reduce the potential for dehiscence. However, it is not always possible to achieve exact wound edge approximation due to wound structure, asymmetric wound margins, or potential interference with the function of a joint(Sal Salcido, 2017). In this study, a novel class of tissue approximation materials, light-activated tissue-integrating sutures (LATIS), were generated, characterized and evaluated for facilitating closure of skin incisions in murine skin, with relevance to dermal closure in spine surgeries. Collagen-GNR LATIS fibers, generated via wet polymer extrusion, demonstrated comparable dimensions and strength to commercial sutures (PGA and silk). GNRs present in LATIS fibers facilitate the generation of a photothermal response upon laser irradiation, which helps attain temperatures required for photothermal approximation of soft tissues. Laser irradiation of LATIS sutures resulted in the highest recovery of skin biomechanical strength compared to all other sutures studied. This performance further supports our hypothesis that better tissue approximation can be achieved using photothermal sealing combined with suturing. Further studies will require modifying the current formulations for deep tissue applications, particularly considering the high shear and wet conditions therein. As described, appreciable tension on the wound site and tissue integration was achieved following laser treatment, but no negative effects including tissue necrosis and / or animal discomfort were observed during the healing period. Histopathology data further suggested that the incision site in LATIS with laser group was completely fused with immature fibrous connective tissue and the fusion of hyperplastic epidermis was achieved in a 3-day period. A small number of inflammatory cells in underlying fibrous tissue was present, which indicated a favorable healing environment at the incision site. No severe inflammatory or allergic responses were observed. Therefore, LATIS facilitates tissue regeneration with minimal inflammation, and it’s convenient handling, tunable physical properties make it a promising practical wound closure option. To our knowledge, this is the first report on laser-activated sutures for achieving improved wound approximation, repair and healing. This approach

can be further extended by functionalizing light-activated sutures with small-molecule drugs and / or growth factors in order to generate multifunctional tissue approximation nanodevices for use in trauma and routine surgery.

CHAPTER 4: COPPER-ELUTING FIBRES FOR ENHANCED TISSUE SEALING AND REPAIR

4.1 INTRODUCTION AND BACKGROUND

The potential use of sutures as multifunctional devices that can simultaneously approximate wounds and deliver bioactive molecules has significant implications in surgery and tissue repair(Joseph et al., 2017). The wide applicability of sutures in surgeries makes them excellent platforms for controlled and localized delivery, which can eliminate the need for systemic administration in tissue repair applications(Champeau et al., 2017). Sutures have been used to deliver growth factors, including basic fibroblast growth factor, vascular endothelial growth factor A, and platelet-derived growth factor to promote repair of injured tendons(Younesi et al., 2016; Y. L. Zhou et al., 2019), adipose-derived stem cells (ASCs) to suppress local acute inflammatory reaction post tracheal anastomosis(Georgiev-Hristov et al., 2012), and bioactive drugs including doxycycline for improving intestinal anastomotic strength (Pasternak et al., 2008). In dermal tissue repair, basic fibroblast growth factor (bFGF) delivery using collagen and polycaprolactone electrospun sutures, and berberine-loaded polyurethane fibers enhanced wound healing in a dermal incision model in mice(Hu et al., 2020; W. Zhou et al., 2019). Suture-mediated delivery of antimicrobial and anti-inflammatory agents, including cefotaxime sodium, levofloxacin, triclosan, silver nanoparticles and diclofenac directly at the wound site has been explored in order to combat surgical site infections (Catanzano et al., 2014; Dubas et al., 2011; Gallo et al., 2016; Justinger et al., 2009; Kashiwabuchi et al., 2017; Wang et al., 2007).

Copper is an essential trace element involved in various physiological and metabolic processes in humans. For example, copper plays a crucial role in different processes of wound healing and is particularly known for promoting angiogenesis in wounds (Borkow et al., 2008).

Elemental copper has been shown to facilitate induction of angiogenesis, expression of vascular endothelial growth factor (VEGF) in primary and transformed human keratinocytes, modulation of integrin expression from keratinocytes and stabilization of extracellular skin proteins(Sen et al., 2002; Tenaud et al., 1999) at physiologically relevant concentrations. In addition, studies describing copper-mediated accelerated closure of murine dermal wounds, extracellular matrix remodeling, and upregulated VEGF expression in excisional murine wound healing have also been reported (Li et al., 2016; Sen et al., 2002; Wang et al., 2017). Although concerns related to copper toxicity exist, it has been reported that human skin is not highly sensitive to copper and risk of toxicity due to dermal exposure may likely be low(Gorter et al., 2004; Hostynek & Maibach, 2006).

Alginate is a linear anionic polysaccharide consisting of 1,4'-linked D-mannuronic acid (M) and L-guluronic acid (G) residues either as blocks of the same unit (MMMMM or GGGGG) or as alternating sequence of these two sugar residues (GMGMGM)(Lee & Mooney, 2012; Skaugrud et al., 1999; Szekalska et al., 2016). Alginate is considered as a generally recognized as safe (GRAS) material by United States Food and Drug Administration (FDA) and has been widely investigated for various pharmaceutical and biomedical applications, including microspheres for drug delivery, matrix for encapsulating cells, and for tissue repair (Fragonas et al., 2000; Ghidoni et al., 2008; Tan & Takeuchi, 2007). Ionic crosslinking using divalent ions (Ca^{2+}, Cu^{2+}, Mg^{2+}, etc.) is the most common method to prepare hydrogels, fibers and beads from aqueous alginate solutions. Two consecutive residues of alginate make an 'egg-box' array upon contacting divalent ions, thus forming an ionically interlinked structure in aqueous environments (Grace et al., 2009; Lee & Mooney, 2012).

Motivated by a potential role for copper ions in wound healing and tissue repair(Sen et al., 2002; Xiao et al., 2017; Zhao et al., 2015), we generated, characterized, and evaluated copper-eluting alginate fibers as potential sutures for the acceleration of wound approximation and repair. We first demonstrated calcium-mediated gelation of sodium alginate to obtain calcium alginate fibers. Subsequent incubation of calcium alginate fibers in copper (II) chloride bath resulted in the formation of copper alginate fibers via displacement of Ca (II) ions by Cu (II) ions(Yang et al., 2019)

within the alginate gel. This ion-exchange was easily observed by a change in color of the fibers (colorless for Ca-alginate to green for Cu-alginate). We characterized the fibers for their photothermal response to near infrared light based on the light absorption properties of copper. Motivated by the need to establish effective dermal closure methods following spine surgeries(Yilmaz et al., 2018), we investigated these fibers as copper-eluting sutures for tissue approximation and repair in a live mouse model that mimicked this surgical closure. Our results indicate that copper-eluting fibers have a role in enhancing wound healing and tissue repair.

4.2 MATERIALS AND METHODS

4.2.1 Materials

Sodium alginate (alginic acid sodium salt), anhydrous calcium chloride ($CaCl_2$), copper (II) chloride dihydrate ($CuCl_2 \cdot 2H_2O$), and glycerol were purchased from Millipore Sigma (St. Louis, MO). To maintain integrity, all reagents were stored at temperatures as indicated by vendor. All solutions were freshly prepared in nanopure water (NPW; resistivity ≈18.2 MΩ cm, Millipore filtration system, Darmstadt, Germany). Commercially available 4-0 monofilament nylon sutures (Monosof, Covidien) were purchased from Covidien and used as controls. All suture sizes are reported based on those in the United States Pharmacopeia (USP).

4.2.2 Generation of copper-alginate (Cu-alginate) and calcium-alginate (Ca-alginate) fibers.

Sodium alginate was first dissolved in nanopure water at a concentration of 5% w/v (50 mg/mL). The solution was heated to 50°C and stirred continuously overnight at 100 RPM till a homogenous solution was obtained. Prior to extrusion, the sodium alginate solution was centrifuged at 3000 rpm for 5 min to remove gas bubbles (Figure 4-1 (i)). The sodium alginate solution was extruded thorough thin tubing into a coagulation bath containing 1% w/v calcium chloride-10% (v/v) glycerol solution using a syringe pump in order to obtain calcium-alginate fibers(Wang et al., 2007). Briefly, a 5 mL syringe (BD Syringes) connected to 8–12 in. long tubing was loaded onto a syringe

pump (NE 300, New Era Pump Systems, Inc.). The tubing inner diameter was 2.0 mm, and the pump was set to a flow rate of 0.75 mL/min. The tubing was then used to extrude the sodium alginate solution into a calcium chloride-glycerol coagulation bath maintained at room temperature to form Ca-alginate fibers (Figure 4-1 (ii)). Following extrusion, the fibers were incubated in the coagulation bath for 60 minutes at room temperature to facilitate calcium ion-mediated crosslinking of sodium alginate. To obtain Cu-alginate fibers, crosslinked Ca-alginate fibers from the calcium chloride-glycerol bath were transferred into a second coagulation bath containing 0.01% w/v copper (II) chloride-10% (v/v) glycerol solution and incubated overnight. Following overnight incubation and chelation of copper ions, green-colored copper-alginate fibers were obtained (Figure 4-1 (iii)) (Grace et al., 2009; Mikołajczyk & Wołowska-Czapnik, 2005). The fibers were then hung and air-dried at room temperature under the tension of their own weight for at least 48 h (Figure 4-1 (iv)). The Ca-alginate and Cu-alginate fibers were stored at room temperature until further use. We also generated Cu-alginate fibers in a one-step process where sodium alginate solution was extruded directly into varying concentrations of copper (II) chloride (3% and 0.1% w/v in nanopure water) - 10% (v/v) glycerol bath. Although this method led to high loadings of copper in alginate fibers, we continued to work with the two-step, ion-exchange gelation process because of toxicity concerns associated with high copper loadings using the former method and better control of loading using the latter.

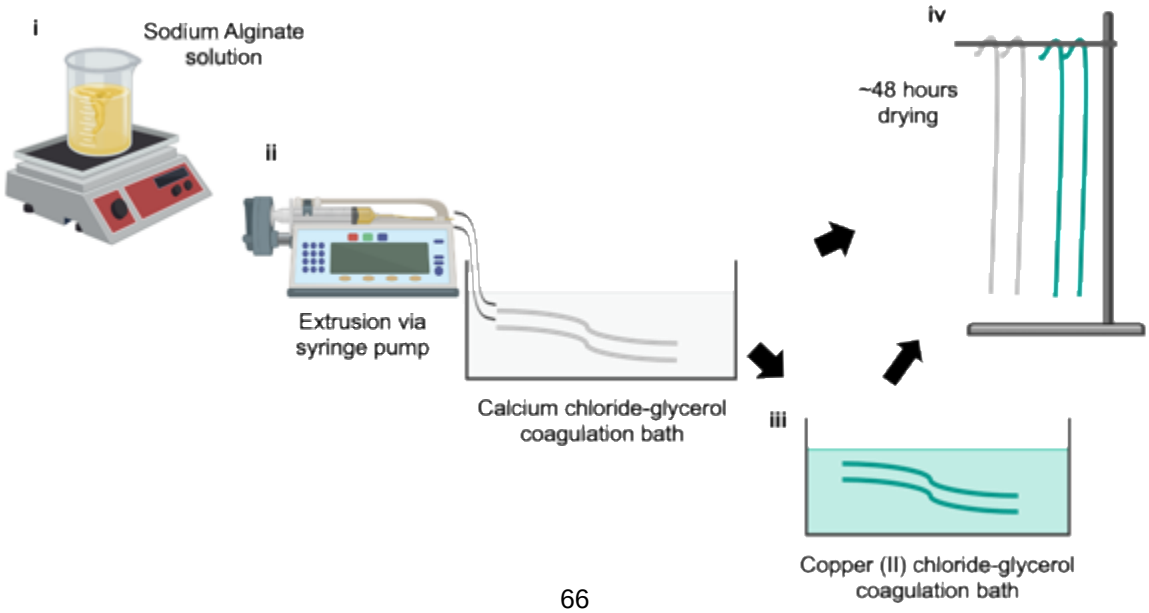

Figure 4-1. Schematic of the process used for generating Ca-alginate and Cu-alginate fibers. (i) Sodium alginate was dissolved in nanopure water (5 wt% or 50 mg/mL), heated to 50°C, and stirred continuously overnight at 100 RPM to obtain a homogenous solution. (ii) Sodium alginate solution was extruded at a flow rate of 0.75 mL/min into calcium chloride solution in NPW (1% w/v) – glycerol (10% v/v) bath maintained at room temperature and the extruded fibers were incubated for 60 minutes. (iii) Extruded Ca-alginate fibers were further incubated overnight in copper (II) chloride (0.01% w/v) – glycerol (10% v/v) bath maintained at room temperature. (iv) Post extrusion, Ca-alginate and Cu-alginate fibers (~12-15 inches in length) were hung and dried in dried at room temperature under tension of their own weight for at least 48 hours.

4.2.3 Field Emission-Scanning Electron Microscopy (FE-SEM)

The morphology of copper-alginate fibers was examined using field emission-scanning electron microscopy (FE-SEM, PHILIPS FEI XL-30). Small sections (2-3 mm sections) of the copper-alginate fibers were cut and mounted on aluminum stubs using double-sided carbon tape. Samples were sputter-coated with gold (Technics Hummer-II sputter coater) in a high-vacuum coater for 60 s at a 2A current, resulting in a coating of approximately 5nm thickness. Samples were then imaged using a PHILIPS FEI XL-30 SEM operated at 10 kV. Three images were acquired at random locations along the length of the cut sections and the diameter was calculated as the average of six measurements.

4.2.4 Mechanical properties

Tensile strengths of Ca-Alginate and Cu-Alginate fibers were determined using a TA.XT Plus Texture Analyzer (Texture Technologies Corp., Hamilton, MA) equipped with Exponent software (Stable Microsystems). Fibers were cut in five-centimeter long fragments and were clamped vertically onto the texture analyzer. The fibers were stretched at a crosshead speed of 2 mm/s in uniaxial tension mode until failure applying force from a 2N load cell. The maximum force (F) exerted per unit of area of fiber (A) until failure was recorded and reported as ultimate tensile strength (UTS, $\sigma = F/A$). The UTS of nylon 4-0 sutures was also measured in a similar manner. All measurements were carried out six times for each sample and the average value of these six measurements was reported.

4.2.5 Photothermal response

A Millennia eV 5W titanium sapphire (Spectra-Physics) laser pumped by a solid-state laser tuned to 800 nm wavelength was configured in continuous wave mode with 130 fs pulses at 12.5 ns intervals and a red HeNe guide beam. The laser spot size was tuned to a diameter of 1.5 mm. The power density was calculated as the power/area of exposure using a FieldMate laser power meter. An A325sc infrared (IR) camera (FLIR, Nashua, NH) with 10 mm 45° lens measured the surface temperature of the fiber during laser exposure. Five-centimeter sections of Cu-Alginate fibers were placed on a glass slide and exposed to laser power densities ranging from 1.6 to 4.8 W/cm^2 for 90 s durations, for 3 cycles in which the laser was turned on for 20 s ("on" cycle) and off for 5 s ("off" cycle). The IR camera also recorded the temperature prior to laser treatment for 5 s and following laser treatment for 10 s. Infrared images were recorded at 1s intervals and were analyzed using ResearchIR software (FLIR, Nashua, NH) in order to determine the maximum surface temperature at the center of the laser exposure area. Similar measurements were repeated for Ca-Alginate and nylon sutures, and their photothermal response upon laser irradiation was collected.

4.2.6 Copper loading and release

A calibration curve, which correlated the absorbance values at 800 nm with different concentrations (0-2.5 wt%) of copper (II) chloride in HCl (1% v/v in NPW) was generated (Figure 4-2A) and used for determination of copper ion content in this study. For the generation of Cu-Alginate fibers, a total of ~1.87 mg of copper (II) ions is available in the 50 mL incubation bath for ion-exchange mediated loading into Ca-Alginate fibers. Following fabrication, the initial copper ion content loaded onto Cu-alginate fibers was calculated by incubating ~5 mg of these sutures in 1 mL of HCl (1% v/v in NPW) for 30 mins under constant stirring at room temperature (RT). Post incubation, 200 μL of supernatant were collected, and their absorbance values were recorded at 800 nm using UV-Vis absorption spectroscopy (Synergy 2 Multi-Mode Reader, BioTek Instruments; Winooski, VT). Absorbance values of the supernatants determined upon incubation in HCl were

used in concert with this calibration curve in order to quantify the amount of copper ions loaded onto suture. The percentage copper ion loading into sutures was calculated as:

$$\%\ copper\ ion\ loading = \frac{Amount\ of\ Copper\ ion\ loaded\ onto\ sutures\ (in\ \mu g)}{\text{Amount of copper ion in copper (II)chloride incubation bath } (in\ \mu g)} \times 100$$

In vitro release of copper from copper-alginate sutures was determined by incubating ~5 mg of Cu-Alginate suture in 1 ml of release medium (PBS at pH 7.4) at 37°C under continuous stirring. At predetermined time intervals, 200 μL of supernatant samples were collected, and their absorbance values were recorded at 800 nm using UV-Vis absorption spectroscopy. A calibration curve using different concentrations (0-2.5 wt%) of copper (II) chloride in NPW was constructed using absorbance values at 800 nm (Figure 4-2B). Absorbance values of the supernatants collected at different time points were used in concert with this calibration curve to quantify the temporal release of copper ions from Cu-Alginate sutures. Copper release was reported in μg/25 milligram copper alginate suture fragment; this weight was approximately of the equivalent length of suture used to close a 1-cm long incision in subsequent *in vivo* studies. All copper ion loading and release studies from Cu-Alginate were carried out with three independent suture fragments (~5mg) taken from different fabrication batches and results are derived from three independent experiments (n=3).

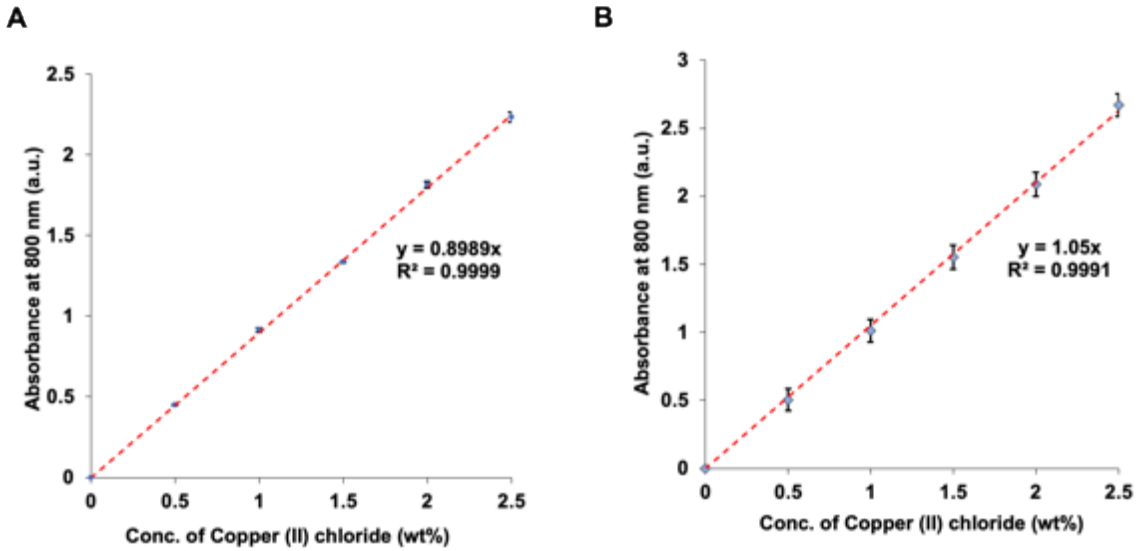

Figure 4-2. Calibration curves for quantifying copper ion loading and release.
(A) Calibration curve of absorbance at 800 nm vs. concentration of copper (II) chloride (0-2.5 wt%) solution in 1% v/v HCl (in NPW). This curve was used for quantifying initial copper loading onto copper alginate sutures. Data shown are mean ± standard deviation of n = 3 experiments. (B) Calibration curve of absorbance at 800 nm vs. concentration of copper (II) chloride (0-2.5 wt%) solution in nanopore water (NPW). This curve was used for quantifying copper release from copper alginate sutures in 1X PBS over a 24-hour time period. Data shown are mean ± standard deviation of n = 4 experiments.

4.2.7 Suture extract preparation for cytotoxicity assay

Prior to extract preparation, all suture samples were sterilized using ultraviolet (UV) irradiation. Next, single strands of sutures (weighing ~ 22-25 mg) were immersed into DMEM media supplemented with 10% fetal bovine serum (FBS) and 1% penicillin streptomycin (PS) and incubated for 24 hours at 37 ºC under constant stirring to obtain suture extracts according to ISO 10993-5 cytotoxicity guide. Post incubation, the extracts were collected for cytotoxicity tests without any filtration(Wallin & Arscott, 1998; Wang et al., 2015).

4.2.8 Cytotoxicity Assay

NIH 3T3 murine fibroblasts (ATCC CRL-1658) and BJ-5ta human fibroblasts (ATCC CRL-4001) were seeded onto 24-well cell culture plates at a density of 25,000 cells per well and allowed to attach overnight. The cells were maintained in DMEM media supplemented with 10% fetal bovine serum (FBS) and 1% penicillin streptomycin (PS). Approximately 24 hours post cell seeding, the culture media was carefully aspirated and replaced with equal amounts of suture extract culture media. Cells were incubated with the suture extracts for 24, 48 and 72 h under cell culture conditions (5% CO_2, 95% humidity, 37ºC).

Cell viability was determined using the spectrophotometry based 3-(4,5-dimethylthiazol-2-yl)-2,5-diphenyltetrazolium bromide (MTT assay). Briefly, 100 µL of the MTT reagent was added to the cells and incubated for 3 h at 37ºC, following which 500 µL dimethyl sulfoxide: methanol (1:1) was added and further incubated at room temperature for 30 min in a shaking incubator. The absorbance of formazan formed in the assay was determined at 570 nm and absorbance of cell

debris, etc. was determined at 670 nm. the absorbance values at 670 nm were subtracted from those at 570 nm and the resulting values were used to determine cell viability as:

$$\%\ \text{cell viability} = \frac{\text{Absorbance of Suture extract treated cells}}{\text{Absorbance of Control}} \times 100$$

The absorbance values for untreated cells, determined in the same manner as above, were used as control. All % cell viability are displayed as mean ± standard error of mean from three independent experiments (n = 3).

4.2.9 Mouse model of dermal closure following spine surgery

All animal care and experimental studies were carried out in compliance with protocols approved by the Institutional Animal Care and Use Committee (IACUC) at Arizona State University. Immunocompetent BALB/c mice (10-12 weeks), weighing 22-25 g, were purchased from Charles River Laboratories, Inc. (Wilmington, MA) and were housed in groups of five till surgery. Prior to surgery, mice were anesthetized with 120mg/kg and 6mg/kg xylazine by intraperitoneal injection. A full-thickness dorsal skin incision model in mice(Ghosh et al., 2019), used to mimic skin closure following spine surgeries, was used to evaluate suture efficacy. Briefly, hair on the dorsal region were clipped and the skin was prepped with chlorhexidine gluconate and alcohol. Two 1-cm, full-thickness skin incisions were made side-by-side using a number 15 scalpel blade on the back of each animal; the incisions were spaced 1 cm apart. Incisions were closed using 4 simple interrupted knots of nylon evenly spaced (0.25 cm pitch), Ca-Alginate, and Cu-Alginate sutures(Yang et al., 2012). The suture-tissue interface was irradiated with the laser, which was scanned along the suture line at a rate of 0.5 mm/second for 2 minutes at ~3.2 W/cm^2, and at an angle between 60 and 80° to the skin, corresponding to temperatures not exceeding 65°C on the suture-skin surface. Choice of suture material for incision closure was randomized; the left and right incisions were closed using two different suture types. Post-surgery, the mice were allowed to recover on a heating pad until fully mobile and then housed individually to prevent suture removal. Mice were allowed to heal for three days following surgery and were monitored daily for any adverse signs. Adverse signs such as inactivity, inability to eat or drink, emaciation, gross infection, or wound dehiscence

required an animal be removed from the study; no such adverse effects were seen in any case and no animal had to be removed from the study. Thiourea days post-surgery, mice were euthanized by CO_2 inhalation followed by cervical dislocation.

4.2.10 Biomechanical analyses

Following euthanasia, rectangular sections of the healed skin around the incision area (2 cm × 2 cm) were excised. Sutures were removed prior to skin tensile strength to measure the strength of the healed tissue alone. Skin samples were stretched until failure at a rate of 2 mm/s using a TA.XT Plus texture analyzer. Ultimate tensile strength (UTS) was determined from the maximum force of the tissue prior to failure, where the maximum force (F) and area of the tissue sample (A) determined the ultimate tensile strength (σ, kPa) of the healed skin (σ = F/A). The tensile strength of intact skin (unwounded and with no incision) was recorded as control. All tensile strengths are displayed as mean ± standard error of the mean from five independent experiments (n = 5). Tensile strength recovery post healing at Day 3 was calculated as the difference between tensile strength of unwounded skin (no incision control, 2 cm × 2 cm section) to healed skin sections in each group. This difference was then converted to a percentage value and reported as % intact skin strength.

$$\%\ \text{intact skin strength} = \frac{\text{UTS of healed skin at Day 3}}{\text{UTS of unwounded skin (no incision control)}} \times 100$$

4.2.11 Histology and immunohistochemistry

Skin tissues from the site of incision were fixed in 10% neutral buffered formalin solution (Scigen) overnight and then stored in 70% ethanol (aqueous) at 4°C until further histological processing. After fixation, skin specimens were dehydrated gradually with ethanol (70% to 100%), cleared in xylene, and embedded in paraffin. Paraffin blocks were sectioned (5 μm) and stained with hematoxylin and eosin (H&E) stain. Epidermal thickness and epithelial gap were measured from H&E stained tissue sections using ImageJ analyses. Epidermal thickness was defined as the vertical distance from the basement membrane to the most superficial layer of the hyperplastic

epidermis measured at six equidistant points around the incision site(Rønø et al., 2013). Epithelial gap is defined as the vertical distance between the regenerating epidermis on either side of the wound edge. Additional sections were further processed for immunohistochemical (IHC) staining using CD31 rabbit polyclonal antibody (Abcam, cat #28364, 1:100) and Ki67 polyclonal rabbit antibody (Abcam, cat #15580, 1:100). All histology and immunohistochemistry results are derived from three independent experiments (n=3).

4.2.12 Image processing for immunohistochemistry sections

To obtain quantitative information staining results, we used Gabriel Landini's "color deconvolution" plugin for ImageJ analysis. Briefly, images were deconvoluted as Image > Color > Color Deconvolution using methods described previously (Ruifrok & Johnston, 2001). For CD31-stained sections, the ratio of positive DAB signal (brown) around the incision site (epidermis and dermis) per field (10x and 20x magnification) were quantified and reported. For Ki67 stained sections, ratio of positive DAB-stained nuclei (brown) around the incision site (epidermis and dermis) per field (10x and 20x) to total nuclei were quantified and reported. The quantification per field was performed using Image J and compared among different suture groups. A total of six fields were evaluated for each group.

4.2.13 Statistical analyses

Data from suture tensile testing, skin tensile strength recovery, and immunohistochemistry are presented as mean ± standard error of the mean (SEM). Differences between groups were assessed using one-way analysis of variance (ANOVA) followed by Tukey HSD Test for pairwise comparison using GraphPad Prism version 8 (GraphPad, USA). A p-value < 0.05 was considered statistically significant.

4.3 RESULTS

4.3.1 Fiber fabrication and characterization

Different divalent cations including Ca^{2+}, Cu^{2+}, Zn^{2+}, and Mg^{2+} were characterized for their light absorption properties in the visible and near infrared (NIR) regions of the spectrum (Figure 4-3A). Copper ions demonstrated a significant absorption peak at ~800nm, which is in the NIR region, and is particularly attractive for photothermal activity; no other divalent cation among those that were investigated demonstrated this property. In case of copper (II) ions, the d-orbital can split to form degenerate orbits, where copper (II) electrons are in higher degenerate (e_g) orbits and lower degenerate (t_{2g}) orbits. This energy gap between the e_g and t_{2g} orbits, called splitting energy, matches the wavelength of the NIR wavelength resulting in photothermal activity as previously described in literature(Li et al., 2018; Lin et al., 2015). It has also been reported that most transition as well as s-block metals absorb light in the ultraviolet (UV) and visible wavelength regions (200-500 nm) of the spectrum(Creighton & Eadon, 1991). We also observed the same when we characterized other metal cations for their absorption in the 400-900 nm wavelength range; only copper (II) ion showed absorption in the NIR region (~750 nm and above). In addition, modestly elevated temperatures have been shown to enhance tissue sealing and wound healing using biomaterials(Ghosh et al., 2019; Urie, Guo, et al., 2018b). Calcium (Ca^{2+} from calcium chloride) was also used for crosslinking alginate, because of its common use in facilitating the formation of alginate gels(Grace et al., 2009; Sugiura et al., 2005). Calcium alginate (Ca-alginate) fibers were first generated for use as sutures by extruding sodium alginate solution (5% w/v in nanopore water or NPW) into a calcium chloride bath (1% w/v in NPW) containing glycerol (10% v/v). Ca-alginate fibers were further incubated in a second bath containing 0.01% w/v copper (II) chloride-10% (v/v) glycerol solution overnight in order to obtain copper alginate (Cu-alginate) fibers by ion-exchange. (Figure 4-1). The use of glycerol as a plasticizer in the incubation bath made the fibers flexible. Cu-Alginate sutures showed a maximal absorbance peak at approximately 800 nm, which is indicative of the presence of copper (II) ions in the fibers. (Figure 4-3B). Digital images of the sutures show

that the Cu-Alginate and Ca-Alginate fibers were uniform in morphology, and that the Cu-Alginate sutures appeared green due to the characteristic color of copper (II) chloride (Figure 4-3C). Field emission scanning electron microscopy (FE-SEM; Figure 4-3D-F) corroborated these results and indicated a generally smooth morphology with striations along the fiber axis. The fiber diameter was estimated to be ~250 μm and as a control we have used a 4-0 nonabsorbable Nylon suture (150-199 μm, USP suture diameter) which is widely used for skin closure. Alternatively, Cu-Alginate fibers were also generated by direct extrusion and incubation of sodium alginate solution into copper (II) chloride (3 and 0.15 w/v in NPW) - 10% (v/v) glycerol bath, although fabricated using the two-step method were employed because of increased control over loading with this method.

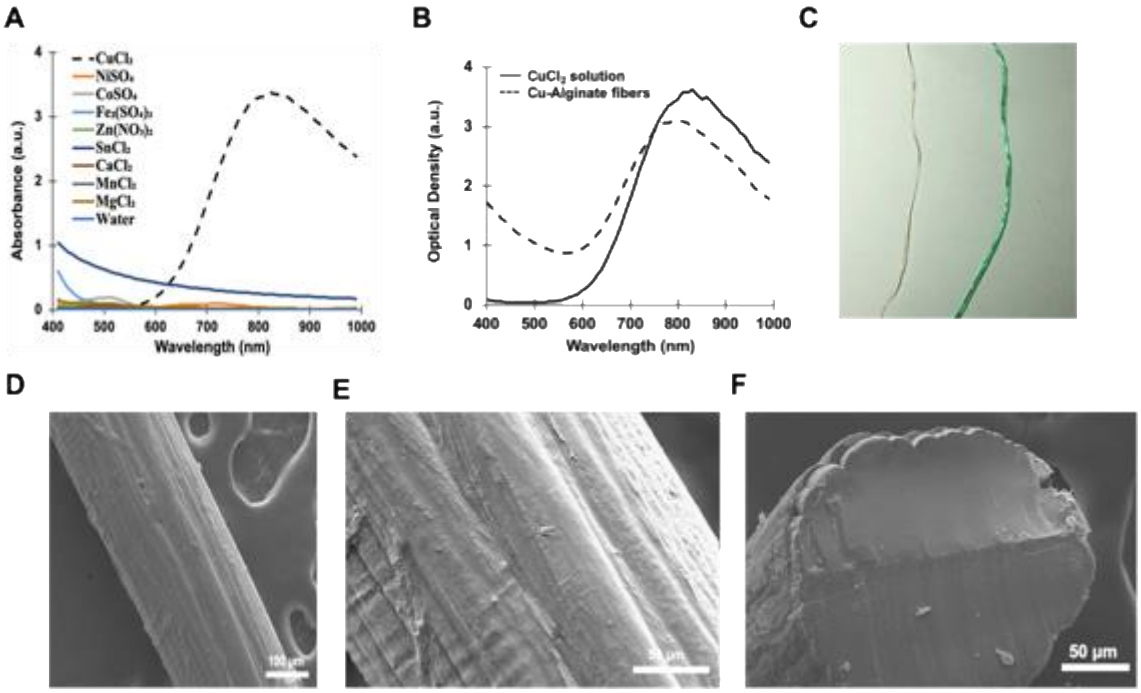

Figure 4-3. Absorbance spectra and representative images of Ca-alginate and Cu-alginate fibers.
(A) Absorbance spectra of different divalent cation salts: $CuCl_2$, $NiSO_4$, $CoSO_4$, $Fe_2(SO_4)_3$, $Zn(NO_3)_2$, $SnCl_2$, $CaCl_2$, $MnCl_2$, $MgCl_2$ in nanopure water (NPW). (B) Absorbance spectra of aqueous $CuCl_2$ solution (0.58 mM in NPW) and Cu-Alginate fibers. (C) Representative images of Ca-Alginate and Cu-Alginate fibers after ~48 hours drying at room temperature. (D) Representative field emission-scanning electron microscopy (FE-SEM) images of Cu-Alginate fibers (accelerating voltage of 10 kV; scale bar = 100 μm). (E, F) Magnified and cross-section FE-SEM images of Cu-alginate fibers (accelerating voltage of 10 kV; scale bar = 50 μm).

4.3.2 Mechanical properties and photothermal response

The ultimate tensile strength (UTS) of Cu-Alginate and Ca-Alginate sutures, determined upon complete drying, were ~10.6 kPa and ~11.3 kPa, respectively, and were comparable to the UTS (~14 kPa) determined for nylon 4-0 sutures (Figure 4-4A). These results indicated that the mechanical properties of the alginate fibers warranted their investigation in potential suturing applications. We investigated the photothermal response of Cu-Alginate sutures based on the absorption of NIR light by copper ions present in the sutures. Copper alginate fibers showed rapid increase in surface temperature upon irradiation with an 800 nm NIR laser; temperatures increased with increasing laser power densities, which ranged from 1.6 to 4.8 W/cm^2. Following laser irradiation, fiber temperatures quickly reached a maximum for a 15 s “on” cycle (blue arrows) and returned to baseline temperature as soon as the laser was switched off in the 5 s “off” cycle (green arrows). The photothermal response was reproducible over multiple cycles and different laser power densities (Figure 4-4B). Laser irradiation of calcium alginate did not show a significant increase in the fiber temperature over baseline temperatures (red line, Figure 4-4B). A similar robust photothermal response of Cu-Alginate fibers was also observed on cadaver murine skin irradiated with NIR laser at a power density of 3.2 W/cm^2 captured using infrared (IR) camera. The immediate area around the incision line is chosen as the region of interest (ROI; marked with white box) and the maximum temperature is depicted using a quantitative color bar (Figure 4-4C).

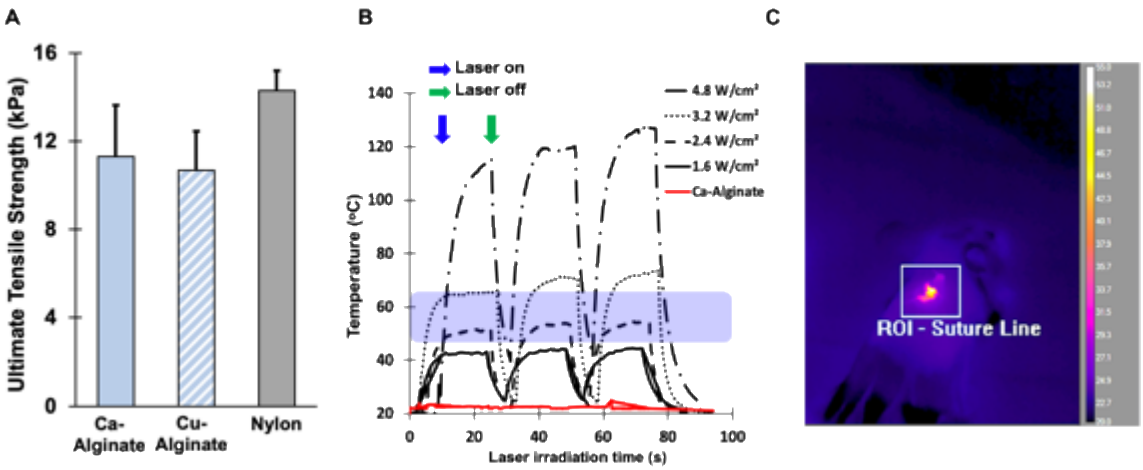

Figure 4-4 Ultimate tensile strength and photothermal response of Ca-alginate and Cu-alginate fibers.
(A) Ultimate tensile strength (UTS) of nylon sutures (Monosof, Covidien) and Ca-Alginate, Cu-Alginate fibers. Ca-Alginate and Cu-Alginate fibers demonstrated ≈80% and ≈75% tensile strength compared to that of nylon sutures, respectively. (B) Photothermal responses of Cu-Alginate and Ca-Alginate fibers following exposure to 800 nm continuous wave (CW) laser at power densities from 1.6 to 4.8 W/cm^2 in a 20 s "on" and 5 s "off" cycle (3 cycles total). The response of the Ca-Alginate fibers to irradiation with 4.8 W/cm^2 laser (800 nm) is indicated by a red line. Each curve is representative of n=6 different experiments. (C) Representative photothermal response of Cu-Alginate fiber on murine skin irradiated with NIR laser at a power density of 3.2 W/cm^2 captured using infrared (IR) camera. The immediate area around the incision line is chosen as the ROI (region of interest marked with white box) and the maximum temperature is depicted using a quantitative color bar

4.3.3 Release of copper ions from Cu-alginate fibers and cytotoxicity of Cu-alginate fibers

The copper ion content and % loading of copper ion in Cu-alginate fibers was determined by incubating Cu-alginate fibers in HCl (1% v/v in nanopure water) for 30 mins under constant stirring at room temperature (RT) to extract copper ions from the fibers. The copper ion content per full length suture (~25 mg) was approximately 40 µg and this was equivalent to ~2.15% copper ion loading based on initial copper content in the coagulation bath used in the fabrication process. Direct copper-mediated gelation using a copper (II) chloride bath (3% w/v in nanopure water) resulted in a copper ion loading of 362.5 µg per 25 mg of suture (weight of 1 equivalent strand of suture used for closing a 1-cm incision). The use of lower copper ion concentrations in the bath (0.3 and 0.1% w/v) did not facilitate gelation and formation of sutures. The ion-exchange method, although carried out in two steps, resulted in lower copper content in fibers of ~40 µg per 25 mg of suture. We reasoned that although high copper loadings obtained with the direct gelation method appear useful, they could lead to tissue toxicities due to the rapid delivery of high local amounts of the ion at the wound site. Consequently, we carried out our studies with the ion-exchange method, which allowed for more controlled loading of copper in the fibers. Further optimization of the direct gelation method can lead to a more streamlined process in the future. The release profile of copper ions from Cu-Alginate fibers was determined in phosphate-buffered saline (PBS; pH 7.4) at 37°C

under continuous stirring. In general, release of copper ions from sutures increased over time, with an initial rapid release rate (0-2 hours), subsequent slow release and a final plateau (up to ~24 hours) (Figure 4-5A). It was found that approximately 95% of the copper originally loaded in the sutures was released in 24 hours. Early release of copper ions is desirable because they upregulate the expression of vascular endothelial growth factor (VEGF), which is pro-angiogenic and augments early processes involved in wound repair, thereby accelerating healing(Johnson & Wilgus, 2014; Sen et al., 2002). It has also been reported that during the early proliferative phases of wound repair, VEGF expression, can stimulate keratinocytes for early repair of epidermal barrier, which enhances reepithelialization activity(Wilgus et al., 2005). Hence, early release of copper can be beneficial for accelerating the healing of incisional wounds following suturing. It is also possible to modulate the loading and release of different amounts of copper depending on therapeutic needs.

NIH 3T3 murine and BJ5T-a human fibroblast cells were treated with suture extracts for 24 hour, 48 hour and 72 hour as per ISO 10993-5 guidelines and % cell viability was evaluated using the 3-(4,5-dimethylthiazol-2-yl)-2,5-diphenyltetrazolium bromide (MTT) assay. No significant reduction in cell viability was observed at any time point due to release of copper ions from Cu-Alginate sutures in either cell type compared to that seen with extracts from nylon or Ca-Alginate sutures, which were used as controls (Figure 4-5B). These results indicate that the copper loading and release from Cu-alginate sutures did not cause toxicity in the cell types employed in the current study.

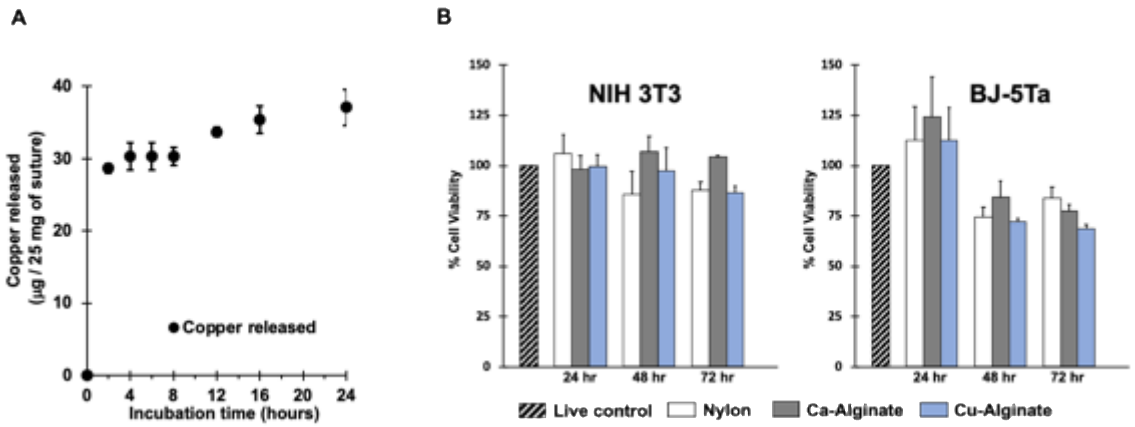

Figure 4-5. Copper ion release and cytotoxicity of Cu-alginate fibers.
(A) Cumulative copper ion release from Cu-Alginate fibers following incubation in phosphate-buffered saline (PBS) for 24 hours under continuous stirring at 37°C. Data shown are mean ± standard error of the mean of n = 3 experiments. (B) Cytotoxicity (% cell viability) of NIH 3T3 and BJ-5Ta cell lines exposed to suture extracts for 24, 48, and 72 h. Data indicate mean ± standard error of mean of n = 3 experiments. Live control indicates cells cultured in untreated media.

4.3.4 *In vivo* incisional repair using Cu-alginate sutures

Ca-alginate, Cu-alginate and commercially available Nylon (4-0) sutures were employed to close a 1-cm long full-thickness incision made in the dorsal skin surface of immunocompetent BALB/c mice. In an additional group, incisions were closed using Cu-Alginate sutures and irradiated with an 800 nm laser (power density 3.2 W/cm^2) for 2 minutes. This animal model was used to mimic dermal closure following spinal surgeries. All sutures demonstrated significant mechanical strength for approximating the incised tissue and no opening (wound dehiscence) was observed following surgical closure (Figure 4-6A-D).

All sutures were removed three days following surgery and the wound edges appeared closed and healed to varying extent in different groups (Figure 4-6E-H). Incisions closed with nylon and Ca-Alginate sutures had minor gaps along the wound edges as observed visually (Figure 4-6E, F), and resulted in skin tensile strengths of 75 $\pm$ 7 kPa and 72 $\pm$ 15 kPa, respectively (Figure 4-6I). Skin at the incision site appeared to have completely closed and healed in incisional wounds closed with Cu-Alginate sutures, with and without the use of the NIR laser; a reduction in tissue gap around wound edges was observed compared to other groups (Figure 4-6G, H). Incisions closed with Cu-Alginate sutures with or without NIR laser irradiation, demonstrated tensile strengths of 102 $\pm$ 7 kPa and 95 $\pm$ 15 kPa, respectively, which indicated the highest biomechanical recovery in tissue strength among the four groups investigated (Figure 4-6I, secondary axis in red). The tensile strength of unwounded (no incision control) skin of BALB/c mice of the same age range was determined to be 188 $\pm$ 22 kPa and was used to compare the efficacy of the different surgical approximation methods. Approximation with Ca-Alginate and nylon sutures resulted in a recovery

of approximately 38.5 ± 3.4 and 40 ± 1.6 % in UTS, respectively, relative to that of intact skin. However, the highest % recovery of tensile strength of healed skin was seen in copper alginate suture approximated incisions: 50.5 ± 6.5 % for copper alginate suture without laser irradiation and 54.4 ± 1.3 % in case of Cu-Alginate sutures followed by laser irradiation of suture line (Figure 4-6I, secondary axis in red). Laser irradiation of Cu-Alginate sutures resulted in similar recovery in tissue tensile strength after a 3-day healing period compared to those not irradiated with the laser. These results indicate that it is likely that the copper ions have a greater effect in determining the healing outcome compared to laser irradiation. However, given the similar performance of laser irradiated and non-irradiated Cu-Alginate sutures, we carried out further studies with the former.

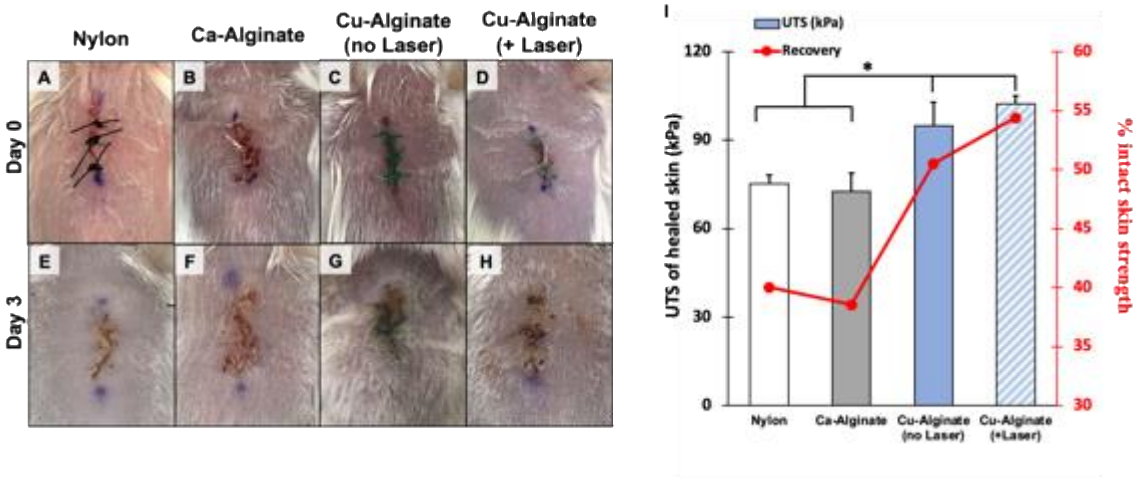

Figure 4-6. Surgical wound closure of dorsal skin incision in BALB/c mice.
(A-D) Representative images of incisions closed with simple interrupted knots made using nylon, Ca-Alginate, Cu-Alginate sutures without laser irradiation and Cu-Alginate sutures irradiated with an 800 nm wavelength, 3.2 W/cm2 laser at a rate of 0.5 mm/s for 2 min. Additional images are shown in Figure S4A in the supporting information section. (E-H) Representative images of incision sites following removal of the corresponding sutures three-days post wounding and surgery. (I) Ultimate tensile strength and biomechanical recovery of healed skin compared to intact skin (secondary axis), three days following surgery. Incisions closed with Cu-Alginate sutures (with and without laser irradiation) resulted in the highest skin tensile strength and % recovery (secondary axis) compared to nylon and Ca-Alginate controls. Data shown are mean ± standard error of the mean of n = 5 experiments (n=4 for Cu-Alginate-no laser irradiation group). Statistical significance was determined using one-way ANOVA (F value = 5.18, degree of freedom = 18) followed by Tukey HSD Test. * indicates p-value < 0.05, which was considered statistically significant.

4.3.5 Histological and immunohistochemical evaluation of healed skin

Histological analysis of the hematoxylin and eosin (H&E)-stained sections of the healed skin revealed that the epidermis was mostly fused in incisions closed with calcium alginate and nylon sutures, but complete reepithelialization was not achieved (Figure 4-7A, B). Improved reepithelialization and fusion of wound edges was observed in incisions closed with laser-irradiated copper alginate suture (Figure 4-7C). Morphometric analysis of H&E-stained histological sections showed significant reduction in epithelial gap (Figure 4-7D-F, solid yellow line) in tissue sections closed with copper alginate sutures compared to those closed using calcium alginate (p-value = 0.007) and nylon sutures (p-value = 0.01) (Figure 4-7M). This finding is consistent with our visual observation which indicated a reduction in wound edge gaps in case of incisions closed with copper alginate sutures (Figures 4-7E-H). The epidermal layer was approximately 3-4 cell layers thick in all three suture groups. Neutrophils were the major cell type in the inflammatory infiltrate around the wound site, with degenerate leukocytes and cellular debris present close to the wound site as eschar (Figure 4-7D-F). The closure of epithelial gap, resulting in a continuous epithelial layer, is crucial for maintaining tissue integrity during and after the repair process (Begnaud et al., 2016). However, no difference in epithelial thickness was observed in case of different suture groups around the incision site (Figures 4-7D-F, dotted black line and Figure 4-7N, p-value > 0.5, not significant or “ns”).

The effect of copper delivery on endothelial cell levels in the wound area was investigated using immunohistological staining for CD31 expression for various suture groups (Figures 4-7G-I). At three days post-surgery, incisions closed with copper alginate sutures had significantly higher CD31 expression (CD31+ positive pixels/field, brown signal) compared to incisions closed with calcium alginate (p-value = 0.01) and nylon sutures (p-value = 0.04). No differences in CD31 expression were observed in skin closed with calcium alginate and nylon sutures (p-value > 0.5, ns) (Figure 4-7O). These findings are consistent with previous studies where copper ion (Cu^{2+}) release from copper metal-organic framework-loaded hydrogels significantly increased the

migration of human epithelial keratinocytes (HEKa) and human dermal fibroblasts (HDF) compared to unloaded hydrogels in an *in vitro* cell migration in scratch assay(Xiao et al., 2017). In another study, copper-containing bioactive glass (BG)/ eggshell membrane (ESM) nanocomposite films successfully stimulated angiogenesis in endothelial cells and upregulated expression of angiogenesis-related genes including VEGF, HIF-1α, KDR (VEGFR2) and eNOS compared to ESM films and BG/ESM films without copper(Li et al., 2016). Copper-oxide impregnated dressings upregulated gene expression of proangiogenic factors (PlGF, VEGF, HIF-1α, etc.) from a pool of 84 angiogenesis related genes studied in full thickness murine diabetic wounds compared to wounds treated with control dressings(Borkow et al., 2010). No significant differences were seen in the proliferation status of the healed tissue closed with nylon, calcium alginate, and copper alginate sutures observed at 3-days post healing (p-value > 0.5, ns; Figures 4-7J-L, P). The tensile strength and histological results indicate that copper alginate sutures are promising devices for promoting repair and healing of incisional wounds *in vivo* compared to calcium alginate and nylon sutures, indicating a role for localized copper delivery.

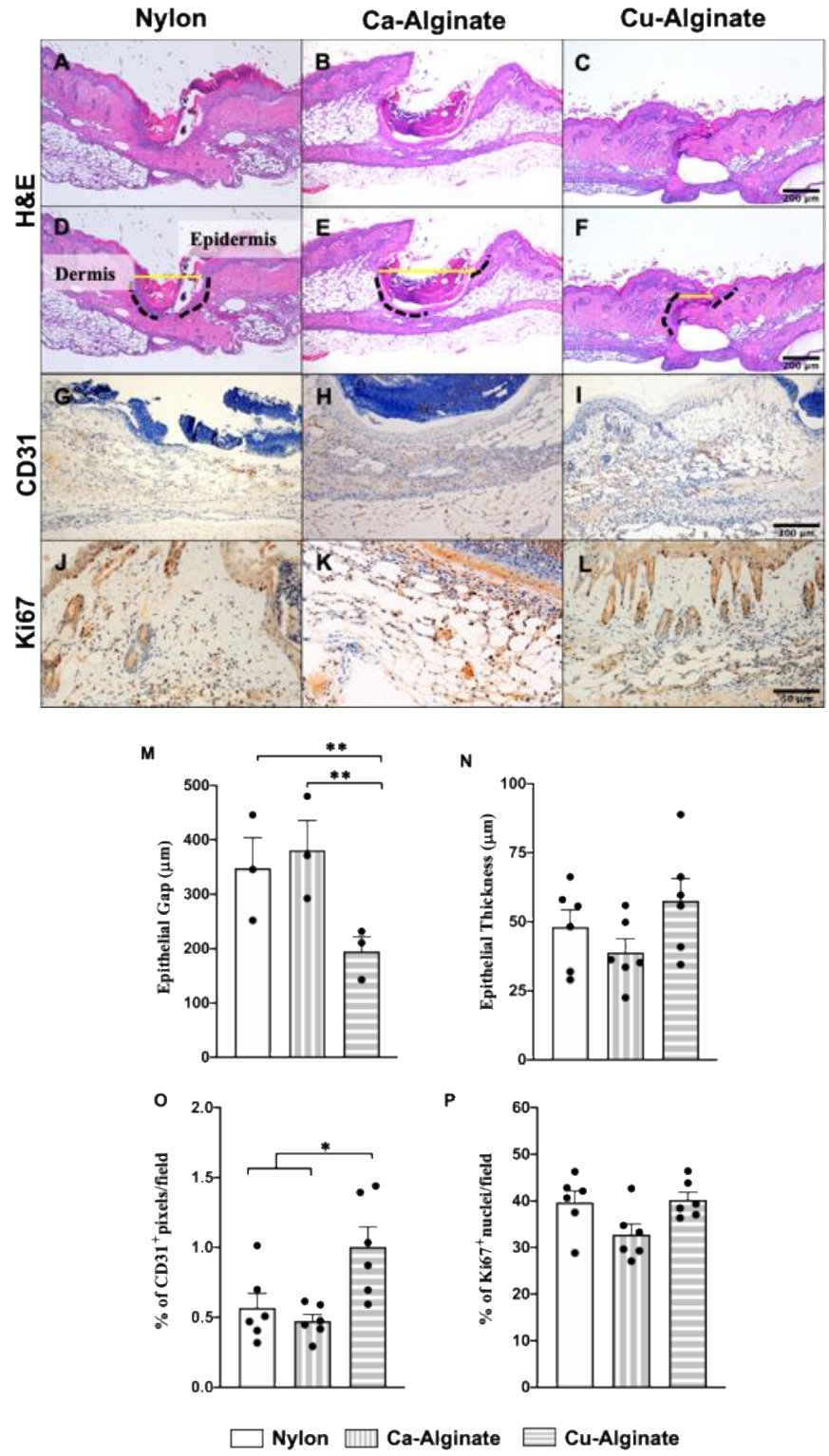
Nylon
Ca-Alginate
Cu-Alginate
H&E
CD31
Ki67
A
B
C
D
E
F
G
H
I
J
K
L
Epidermis
Dermis
200 µm
100 µm
50 µm
M
N
O
P
Epithelial Gap (µm)
Epithelial Thickness (µm)
% of CD31+ pixels/field
% of Ki67+ nuclei/field
**
**
*
Nylon
Ca-Alginate
Cu-Alginate

Figure 4-7. Analysis of healed tissue at day 3 post wounding closed with Nylon, Ca-alginate and Cu-alginate sutures.
(A–C) Representative digital images of hematoxylin and eosin (H&E)-stained cross-section of the incision area (scale bar = 200 µm). (D-F). Representative histological images (from n=3 independent experiments for each group) of H&E stained tissues showing regenerated epidermis at the wound site (shown with black dotted line) and dermal gap (shown with yellow solid line). (G-L) Representative digital images of the vascularization biomarker CD31 (scale bar = 100 µm) and proliferation biomarker Ki67 (scale bar = 50 µm) stained cross-section of incision area respectively. (M, N) Quantification of epithelial gap and epithelial thickness at the incision site for different suture groups obtained from H&E stained cross-section of incision areas of the different groups. Data shown are mean ± standard error of the mean for n = 3 experiments. (O, P) Quantification of CD31+ pixels/field and Ki67+ nuclei /field obtained from CD31 and Ki67 stained cross-section of incision area of various suture groups, respectively. Data shown are mean ± standard error of the mean of n = 3 experiments. * Indicates p-value < 0.05, ** indicates p-value < 0.01 which was considered statistically significant

4.4 CONCLUSIONS

Here, we generated copper-eluting fibers to augment biomechanical approximation and repair of soft tissues following surgical or traumatic injuries. Cu-Alginate sutures demonstrated a robust and reversible photothermal response following irradiation with lasers in the near infrared wavelength range. Local delivery of copper ions from Cu-Alginate sutures significantly improved skin biomechanical recovery at early time points (three days) post wounding compared to Ca-Alginate and nylon sutures in a murine model of skin closure following spine surgeries. It was observed that subsequent laser irradiation of the Cu-Alginate closed wounds did not enhance biomechanical strength recovery of healed skin compared to non-irradiated Cu-Alginate suture closed wounds. Biochemical analyses indicated that Cu-Alginate sutures increased the number of $CD31^{+}$ cells, which is indicative of increased angiogenesis. However, high levels of copper can cause toxicity and care must be taken to optimize doses for effective repair. To our knowledge, this is the first report on the delivery of ionic copper from sutures for enhancing wound approximation, repair, and healing. We posit that judicious selection of sealant biomaterials, including those effective in photothermal repair (Ghosh et al., 2019), together with localized copper delivery, will likely lead to new multifunctional devices for approximation and repair of different wounds.

CHAPTER 5: SILK FIBROIN SEALANT WITH TEMPORAL DELIVERY OF BIOACTIVES ACCELERATES WOULD HEALING

5.1 INTRODUCTION AND BACKGROUND

Chronic wounds affect 6.5 million patients in US annually (1 in 38 adults) and account for $20 billion per year in health management costs. Dysregulation of finely regulated events at any stage of healing leads to non-healing wounds(Powers et al., 2016; Sen et al., 2009). Complexity of repair process, low potency of monotherapies and delivery challenges limit the effectiveness of current wound healing treatment strategies, particularly in chronic and diabetic wounds. Growth factors, engineered cells and skin grafts have been investigated for promoting wound healing. However, little attention has been given to the critical role of augmenting early-stage processes in order to set the stage for effective execution of subsequent proliferation and remodeling phases of tissue repair.

Upon injury, mast cells are recruited at the wound site in a chemokine-dependent manner. Monocyte chemoattract protein-1 (MCP-1) released by keratinocytes, endothelial cells and other inflammatory cells present at the wound edge following injury and as five-fold increase in mast cells numbers at the wound site has been reported(Trautmann et al., 2000). Arriving mast cells then degranulate in response to various stimuli (physical, immunogenic, and neuropeptide) and release mediators which are either pre-formed and stored in granules (histamine, heparin, chymase, serotonin and tryptase), synthesized de novo upon cell stimulation (lipid mediators like PAF, PDG2, etc.), and or as cytokines (IL-1, IL-3, IL-10, GM-CSF, TNF-α, etc.)(Komi et al., 2018). Mast cells and its mediators have been reported to be involved in all four stages of wound healing(Artuc et al., 1999; Wulff & Wilgus, 2013). Histamine as one of the mediators released from mast cells have been widely studied for its role in wound healing. Under in vitro conditions, addition of exogenous histamine in a dose dependent manner (10 ng/mL to 250 ng/mL) improved fibroblast migration with 100 ng/mL dose significantly upregulating migration(Kupietzky & Levi-Schaffer,

1996). Similarly, wound healing in histidine decarboxylase gene-knockout ($HDC^{-/-}$) mice was impaired and single dose of exogenous histamine (100 nmol or 1 µmol/g skin) recovered healing in these mice. It was suggested that exogenous histamine promoted angiogenesis and recruitment of macrophages by upregulating bFGF levels in wounds(Numata et al., 2006). Besides accelerating repair, exogenous histamine (i.p. injection) has also been shown to improve healed skin strength in the earlier stages of healing in incisional wounds in rats(Boyd & Smith, 1959). Histamine also stimulated collagen synthesis in human skin derived fibroblasts in a dose dependent manner and levels of collagen type I were upregulated(Hatamochi et al., 1991) and use of antihistamine (diphenhydramine hydrochloride) reduced fibroblast growth in human skin, scar and keloid samples under in vitro conditions(Topol et al., 1981). Specifically, inhibition of histamine activity using H1 receptor antagonists like mepyramine and promethazine have negatively impacted wound healing outcomes by reducing strength of incisional wounds and collagen content in healed tissue in rats whereas H2 receptor antagonists did not impair healing outcomes (Bairy et al., 1991). It was reported that low doses of histamine increased collagen production and maturation in wounds, but higher doses showed inhibition in collagen production and polymerization(Masliíski & Olczak, 1977).

Here, we investigate the therapeutic potential of topical application of histamine along with silk fibroin-based sealant for repair of full-thickness excisional wounds both in acute and diabetic splinted skin wound models in mice. Silk fibroin-based scaffolds have been reported to be conducive for healing outcomes in challenging wounds previously and also subject to clinical trials in human patients(Farokhi et al., 2018; Zhang et al., 2017). Our results indicate that silk fibroin-based films combined with topical histamine delivery can enhance wound repair involving mechanisms of neoangiogenesis, myofibroblast activation, transient epidermal EMT, and also improve healed skin biomechanical strength. Based on the wound closure kinetics of histamine and silk sealant as a therapeutic, we further investigated the benefit of temporal delivery of a second therapeutic (growth factor nanoparticles) in modulating wound healing outcomes in both acute and diabetic wounds. Our hypothesis of temporal delivery of second therapeutic around the ‘transition

period' of wounds moving from early repair to late repair phenotype further improve wound closure kinetics and biomechanical recovery of skin strength. A fundamental understanding of tissue repair kinetics and associated temporal delivery of therapeutics can lead to faster healing and improved tissue repair outcomes, thus reducing the propensity for re-opening, progression to intractable phenotypes and surgical site infections, all of which can have remarkable outcomes in the clinic.

5.2 MATERIALS AND METHODS

5.2.1 Materials

Cetyltrimethyl ammonium bromide (CTAB), chloroauric acid trihydrate ($HAuCl_4.3H_2O$), ascorbic acid, sodium borohydride ($NaBH_4$), hydrochloric acid (HCl), and silver nitrate ($AgNO_3$) were purchased from Millipore Sigma (St. Louis, MO) for gold nanorods (GNRs) synthesis. All solutions were freshly prepared in nanopure water (resistivity ~ 18.2 MΩ-cm, Millipore filtration system, Darmstadt, Germany). Silkworm (*Bombyx mori*) cocoons were purchased from Mulberry Farms, California, USA to obtain silk fibroin.

5.2.2 Gold nanorods (GNRs) synthesis

GNRs were synthesized according to a previously described seedless growth method, forming nanorods stabilized by a CTAB bilayer. GNRs synthesized using this method demonstrated a peak absorbance of ~800 nm, as determined by ultraviolet (UV)-visible spectrophotometer (Biotek Synergy2 pate reader). To remove excess CTAB, GNRs were further centrifuged and redispersed in nanopure water two additional times, bringing down the final free CTAB concentration in the solution to less than 0.15 mM(Russell Urie et al., 2015).

5.2.3 Silk fibroin extraction and silk-GNRs film preparation

Silk fibroin was extracted from *Bombyx mori* silkworm cocoons according to previously described protocols(Rockwood et al., 2011; Urie, Guo, et al., 2018b). Briefly, silkworm cocoons

were degummed in a boiling 0.02M Na_2CO_3 (Sigma–Aldrich, St. Louis, MO) solution for 30 min, washed with distilled water three times, and dried at room temperature (RT). Degummed silk fibroin was dissolved in 9.3 M LiBr solution at 60 °C for 4 h, centrifuged to separate insoluble contents, and dialyzed for 72 h at 4 °C against a 3.5 kDa membrane to remove LiBr and impurities. Dissolved silk fibroin solution was centrifuged at 14000 rpm for 20 min to remove remaining impurities. The solution was lyophilized and stored at RT for further use. Concentrated GNRs (0.5 wt%) were added to aqueous silk fibroin solution (8 wt%) and homogenously mixed. 200 μL of this solution was poured over 8mm round glass coverslips and dried overnight at RT to obtain silk fibroin sealant films. The dried silk fibroin sealant films were cut to 3.5 mm or 5mm discs using biopsy punches (Integra Miltex, VWR) to match the wound size in our mice model.

5.2.4 Animals, Wound model, and Treatment

The Animal Care Committee of the Arizona State University approved all animal studies. Equal numbers of male and female mice were used in strict accordance with the Guide for the Care and Use of Laboratory Animals of the National Institutes of Health. Eight-week-old BALB/c mice (strain code 028) and BKS.Cg-*Dock7*^{m} +/+ *Lepr*^{db}/J mice (strain code 000642) were ordered from Charles River Laboratories and The Jackson Laboratory, respectively. Mice were acclimated to their environment for at least 1 week prior to the procedure and were allowed food and water *ad libitum*. The *db/db* mice at 10 weeks were tested for their blood glucose levels with a glucometer (Accu-Chek; Aviva) to confirm that plasma glucose levels were above 400 mg/dL at least three days before surgery. Mice were anesthetized with 120mg/kg ketamine and 6mg/kg xylazine by intraperitoneal injection. The dorsal surface was shaved with an electric clipper, and prepped using chlorhexidine gluconate and alcohol in series to the surgical site. 3.5- or 5-millimeter biopsy punches (Integra Miltex, VWR) were used to create middorsal full-thickness wounds by excising epidermis and dermis, including the panniculus carnosus. Immediately after the surgery on day 0, the wounds were topically treated with 10 μL of either 8.2 mM (1.5 mg/ml) histamine dihydrochloride solution in saline (low-histamine group, H1), or 40.8 mM (7.5 mg/ml) histamine dihydrochloride

solution in saline (high-histamine group, H2), or saline (control group). The wound beds were then covered with biosealant or Tegaderm films (3M). A donut-shaped splint with an inner diameter of 6-mm prepared from a 0.5 mm-thick silicone sheet (Grace Bio-Laboratories, Bend, OR) was placed so that the wound was centered within the splint. An immediate-bonding adhesive (Krazy Glue®; Elmer's Inc.) was used to fix the splint to the skin followed by interrupted 4–0 nylon sutures (Monosof™ monofilament nylon sutures, Medtronic) to ensure position. In order to prevent contraction of the wounds, silicon splint was used allowing wounds to heal thorough granulation and re-epithelialization(Galiano et al., 2004). The mice were recovered on a heating pad until fully mobile. The mice were housed individually to prevent splint removal.

5.2.5 Planimetric wound area image analysis

Wounds were photographed daily post-wounding, and wound areas were determined by calibrated image analysis using ImageJ/FIJI (NIH). Day 0 wound areas were considered as 1 and all wound areas of subsequent days were normalized accordingly. Changes in wound areas were expressed as the proportion of the initial wound areas and represented as normalized wound area.

5.2.6 Biomechanical analyses of healed skin

Following euthanasia, rectangular sections of the skin around the wound area (approximately 20 x 0.5 mm) were excised at days 7 (BALB/c mice) and 11 (*db/db* mice) post wounding. Skin samples were stretched until failure at a rate of 2 mm/sec using a TA.*XT* Plus texture analyzer. Ultimate tensile strength (UTS) was determined from the maximum force of the tissue prior to failure, where the maximum force (F) and area of the tissue sample (A) determined the ultimate tensile strength (σ, kPa) of the sutured skin ($\sigma = F/A$). The tensile strength of intact skin (with no incision) was also tested for comparison. All tensile strengths are displayed as mean ± standard error of mean from at least five independent mice (n=5) or as mentioned in different conditions. Tensile strength recovery for skin samples were calculated as a difference between

ultimate tensile strength for each group after healing from native skin strength, with the difference then converted to a percentage.

5.2.7 Temporal delivery of second therapeutic in wounds

We delivered growth factor-elastin like polypeptide nanoparticles (GFNPs) which were developed as a fusion protein with stromal-cell derived factor-1 (SDF1) or basic fibroblast growth factor (bFGF) and ELP domain(Yeboah et al., 2016; Yeboah et al., 2017). In case of subsequent treatments on post wounding day 3 (BALB/c and *db/db*) or day 6 (*db/db*), the mice were anesthetized using 1-3 % isoflurane, and 20 µL of saline or 20 µL of saline containing GFNPs (2000 nM concentration) was topically applied on the wound using an insulin syringe inserted thorough the silicone splint without disrupting the healing wound bed.

5.2.8 Immunohistochemistry staining

Mice were euthanized either 7 (BALB/c mice) or 11 days (*db/db* mice) post wounding. Wound tissues, with unwounded skin margins were fixed in 10% neutral-buffered formalin for at least 72 hours and then processed without further storage. Tissues were then embedded in parafilm, and 5-6-µm thick sections were captured on charged glass slides and dried for further processing. Immunohistochemistry (IHC) staining was performed using the methods described previously(Yaron et al., 2020). Briefly, dried sections on charged glass were deparaffinized and rehydrated thorough xylene and graded alcohols into tap water. A sandwich method was used for epitope retrieval where rehydrated slides were submerged in epitope retrieval buffer (pH 6, sodium citrate buffer with 0.05% Tween20), sandwiched with another clean glass slide, and incubated at 60 °C. Following epitope retrieval, sections were washed with 3% hydrogen peroxide in PBS to quench endogenous peroxidases and blocked with 5% bovine serum albumin in TBS/0.1% Tween 20 to prevent non-specific protein binding. Sections were then probed overnight at 4 °C with antibodies listed in Table 5-1. HOURP and Ap-conjugated secondary antibodies against rabbit and rat IgG (Jackson ImmunoResearch, West Grove, PA) were applied at a dilution of 1:500 for 2 hours

at room temperature. Antigens were either developed with ImmPACT DAB (HOURP) or Vector Red (AP) as listed in Table 5-1. Developed slides were then counterstained by Hematoxylin (Gill No. 2, #GHS232, Sigma Aldrich, St. Louis, MO) for 3 minutes except in case of iNOS stained slides to retain clarity during image analysis, differentiated by 6-12 quick dips in acid alcohol (0.3% hydrochloric acid in 70% ethanol), and blued in a solution of ammonium water (0.2% ammonium hydroxide in distilled water) for 30 seconds. Followed by dehydration thorough an abbreviated 90% ethanol, absolute ethanol series, xylene and then mounted with CytoSeal XYL (Richard-Allan/Thermo Fisher Scientific, Kalamazoo, MI). All histology and immunohistochemistry results are derived from three independent mice (n=3). Stained slides were imaged on an Olympus BX43 upright microscope equipped with an Olympus DP74 CMOS camera operated by cellSens Standard software (Olympus Corporation, Center Valley, PA).

Table 5-1. List of antibodies used for immunohistochemistry

Antibody	*Manufacturer*	*Catalog #*	*Host*	*Clonality*	*Clone ID*	*Dilution*	*Detection*
pSTAT3	Cell Signaling	9145	Rabbit	Monoclonal	D3A7	1:400	ImmPACT DAB (HOURP)
Slug	Cell Signaling	9585	Rabbit	Monoclonal	C19G7	1:200	ImmPACT DAB (HOURP)
E-cadherin	Cell Signaling	3195	Rabbit	Monoclonal	24E10	1:400	ImmPACT DAB (HOURP)
Arginase-1	Cell Signaling	93668	Rabbit	Monoclonal	D4E3M	1:200	ImmPACT DAB (HOURP)
iNOS	Abcam	ab15323	Rabbit	Polyclonal	N/A	1:100	ImmPACT DAB (HOURP)
CD31	Abcam	ab28364	Rabbit	Polyclonal	N/A	1:50	ImmPACT DAB (HOURP)
alpha-SMA	Abcam	ab5694	Rabbit	Polyclonal	N/A	1:200	ImmPACT DAB (HOURP)
Ly-6G	Invitrogen	14-5931-82	Rat	Monoclonal	RB6-8C5	1:100	Vector Red (AP)

5.2.9 Image processing and analyses

Morphometric features of healing were assessed in ImageJ/FIJI. Images were calibrated according to magnification. To obtain quantitative information staining results, we used

Gabriel Landini's "color deconvolution" plugin for ImageJ analysis. Briefly, images were deconvoluted as Image > Color > Color Deconvolution using methods described previously(Ruifrok & Johnston, 2001). For CD31 and α-SMA stained sections, the % of positive DAB signal (brown) in the granulation tissue per field (10x magnification). For pSTAT3 and Slug-stained sections, the % of keratinocytes with positive (brown) nuclear pSTAT3 and Slug expression per field (20x magnification) in the fields immediate to the epithelial tongue was reported. For E-cadherin-stained sections, the number of keratinocytes in the epithelial tongue with marked loss of E-cadherin at the cell boundaries was reported. Arg-1, iNOS, and Ly-6G stained sections were quantified as the % of positive DAB signal (brown) and AP signal (magenta in Ly-6G stained sections) in the granulation tissue per field (20x magnification).

5.2.10 Statistical analyses

All data and figures in this paper were analyzed and plotted by GraphPad Prism 9.0 (GraphPad Software). The obtained data are expressed as means ± standard error of mean. The statistical significance analyses were performed using either one way or two-analysis of variance (ANOVA) and relevant post-hoc test mentioned in figure captions. *P*-values less than 0.05 was considered statistically significant.

5.3 RESULTS

5.3.1. Generation and characterization of LASE

Aqueous dispersion of GNRs with a characteristic plasmon resonance peak at ~800 nm was obtained from seedless growth method. Concentrated GNRs (0.5 wt%) were added to aqueous silk fibroin solution (8 wt%) and silk fibroin sealants were prepared by slow drying at RT. As prepared ~200 µm thick films were cut to 3.5 mm or 5 mm discs to be used on wounds in vivo.

To demonstrate the potential of silk fibroin sealants in accelerating wound healing it was tested against an FDA-approved and clinically available polyurethane wound dressing (Tegaderm)

in vivo. In the mouse wound healing model, full thickness 3.5 mm or 5 mm wounds were treated with 10 µl saline (control) and covered with either Tegaderm or silk fibroin sealants. Wounds covered with silk fibroin sealant, and it formed a viscous paste upon being placed on the moist wound bed. The wound bed was subsequently laser irradiated with a NIR laser tuned to 800 nm peak wavelength at 2.4 W/cm^2, resulting in temperatures between 50 and 65 °C on the wound bed. Wound bed covered with Tegaderm were also laser irradiated in the same manner and no rise in surface temperature of the wound bed was observed.

5.3.2 Silk fibroin sealant, histamine and their combination promote full thickness acute wound healing

Acute wounds were treated with Tegaderm and silk fibroin sealant in combination with saline or histamine (Figure 5-1A). Daily planimetric measurements were performed and normalized wound area was calculated everyday post wounding to track wound closure over time. Silk fibroin sealant and saline treated wounds showed significant reduction in wound area day 5 onwards compared to Tegaderm saline control wounds ($p < 0.05$, n=6). By day 7, Tegaderm saline-control wounds had only achieved an average of ~63% wound closure, while silk fibroin sealant-saline treated wounds accelerated the process and had ~83% wound closure ($p < 0.0001$, n=6) (Figure 5-1B). A single dose of histamine (40.8 mM histamine dihydrochloride in 10 µL saline or 3.4 mg/kg based on average mouse weight of 22g) applied to the wounds further accelerated wound closure both in case of Tegaderm or silk fibroin sealant covered wounds. Early experiments looked at histamine treatment of wounds with two concentrations of histamine, either 8.2 mM (0.7 mg/kg) or 40.8 mM (3.4 mg/kg) in 10 µL saline. With the early wound closure data, we modified our experiments to use only the 40.8 mM dose of histamine. Wound closure was most accelerated in silk fibroin sealant – histamine treated which achieved complete wound closure (~99.3%) by day 7, with improved wound closure also seen in Tegaderm-histamine group to ~88% ($p < 0.0001$, n=6). Along with silk fibroin sealant as the wound dressing, single dose of histamine exhibited enhanced wound closure from day 4 post wounding compared to saline treatment ($p = 0.006$, n=6) (Figure 5-1B).

Biomechanical tests were also performed to determine the extent of skin wound healing compared to intact skin. Uniaxial tensile strength is a common and simple test method to biomechanical recovery, which measures the tensile failure load of skin at specified conditions(Bellare et al., 2018; Fernandes et al., 2019). Clearly, silk fibroin sealant covered wounds (792 ± 14.7 kPa, 39.6% recovery) showed higher biomechanical strength of healed skin at day 7 post wounding compared to Tegaderm saline-control wounds (425 ± 3.9 kPa, 21.2% recovery). Early treatment of histamine along with Tegaderm and silk fibroin sealant further improved healed skin biomechanical strength; 888.9 ± 127.2 kPa and 1185.96 ± 127.8 kPa respectively (44.5% and 59.2% recovery, n=4, Figure 5-1C).

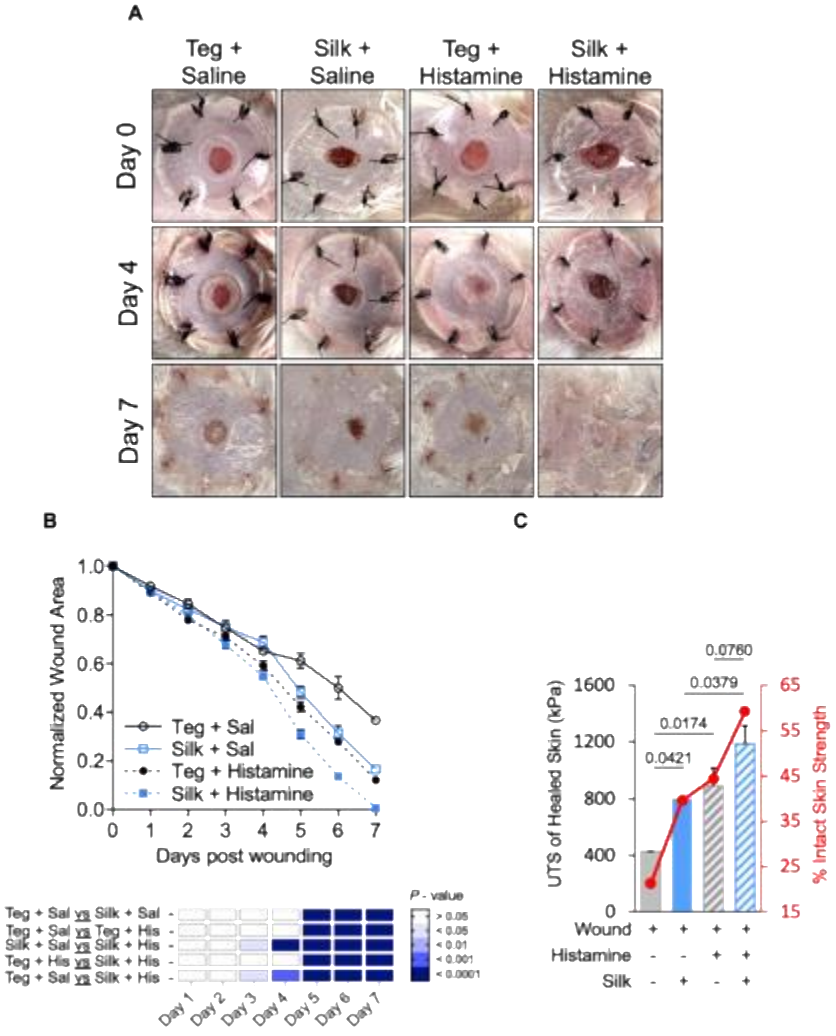

Figure 5-1 Silk sealant, histamine and their combination accelerate acute wound healing. Representative wound images of Tegaderm saline, silk sealant saline, Tegaderm histamine, and silk sealant histamine wounds on day 0, 4, and 7 post wounding. (B) Daily planimetric measurement of wound areas normalized to day 0 for each mouse. Data shown are mean ± standard error of mean of n = 6 mice per group. Statistical significance was determined using one-way ANOVA with correction for multiple comparisons by Holm-Sidak method. Individual p-values between groups on individual days post wounding are shown using a color-coded heat-map. (C) Plot showing ultimate tensile strength and % recovery of healed skin strength (secondary y-axis) 7-days post wounding. Data shown are mean ± standard error of mean of n = 4 mice per group. Statistical significance was determined using one-way ANOVA with correction for multiple comparisons by Tukey method. Individual p-values between groups are shown in the plot.

5.3.2 Effect of silk fibroin sealant, histamine and their combination on myofibroblast response and angiogenesis

We investigated α-smooth muscle action (αSMA) expression in the wound bed which is a known marker of myofibroblasts cells in skin (Figure 5-2A). Myofibroblasts play a role in fibroblast contractility and implicated in contracting the wound edge during the wound healing process(Hinz et al., 2001). Quantification of αSMA^+ pixels per 20x field in the granulation tissue was performed on day 4 and 7 post wounding. Silk sealant treatment along with histamine had a significantly higher expression of αSMA^+ pixels compared to Tegaderm saline control wounds ($p < 0.05$), and an increasing trend compared to silk sealant alone treated wounds ($p = 0.08$). No difference was observed between silk sealant-histamine treated wounds and Tegaderm-histamine wounds at this timepoint. At day 7 post wounding, Tegaderm-histamine treated wounds had a persistent higher αSMA^+ expression compared Tegaderm saline control wounds ($p = 0.055$). Similarly, silk sealant treated wounds had a higher αSMA^+ expression but no significant difference was observed compared to silk sealant treated wound alone (Figure 5-2C). Similar effect on increased myofibroblast activity in wound bed was reported with exogenous histamine delivery in mice(Numata et al., 2006). We also performed immunohistochemistry staining of wound tissues for CD31 on day 4 and 7 post wounding, a canonical marker for endothelial cells in the vasculature to observe the degree of neovascularization in wound beds (Figure 5-2B). Quantification suggested a trend towards increased CD31+ expression in silk sealant treated wounds compared to

Tegaderm treated samples at day 4 post-wounding. The combination of silk and histamine resulted in higher expression of CD31 stained endothelial cells at day 4 post-wounding (Tegaderm saline vs silk histamine $p < 0.05$, Tegaderm histamine vs silk histamine $p < 0.05$, Figure 5-2D). Although during the course of the healing at day 7 post-wounding, no significant difference in CD31 expression was observed in granulation tissue of different groups (Figure 5-2D).

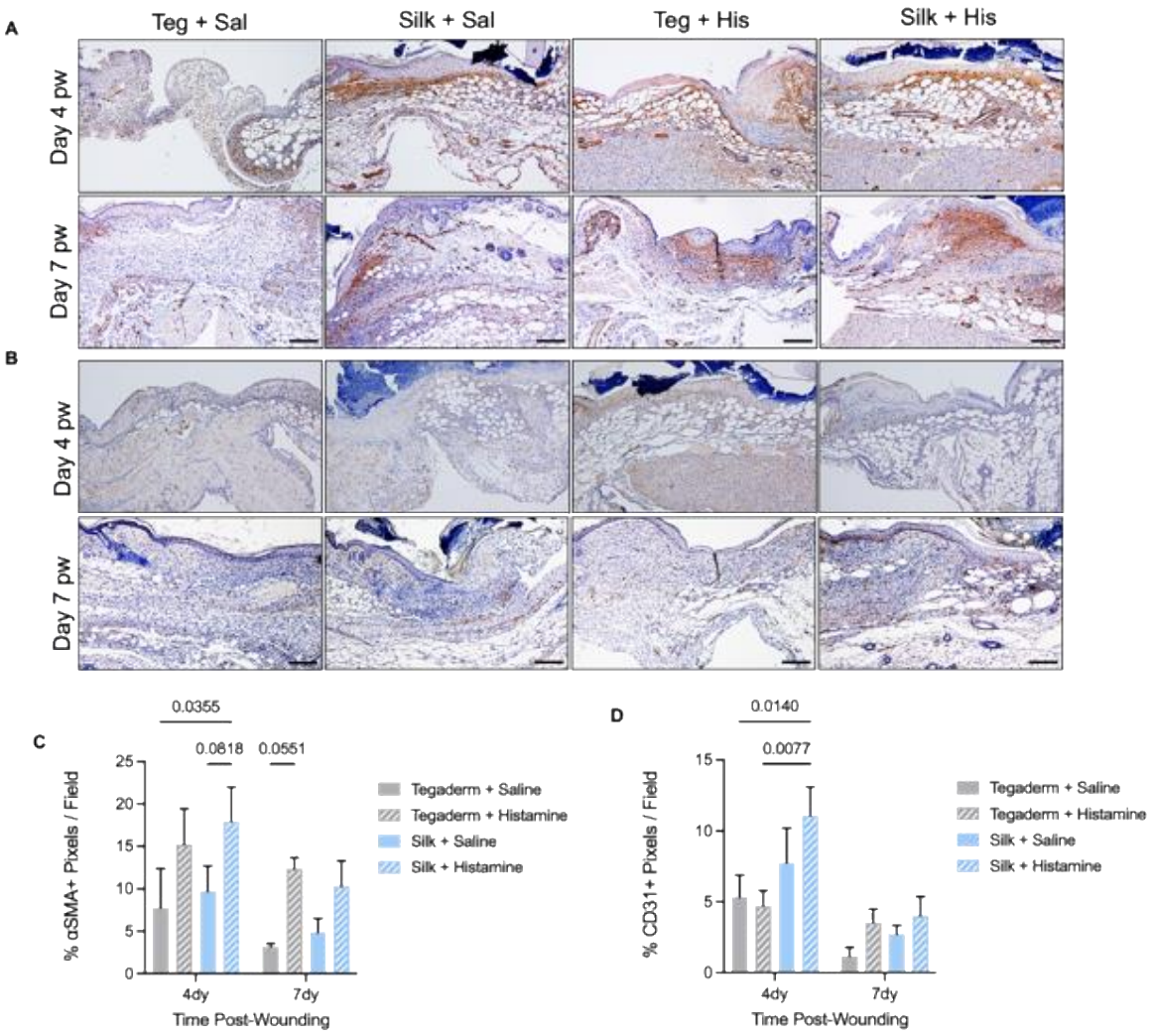

Figure 5-2. Effect of silk sealant, histamine and their combination on myofibroblast response and angiogenesis.
(A) Representative wound bed micrographs of αSMA stained IHC field (10x magnification) on day 4 and 7 post wounding for all the groups (scale bar = 200 µm). (B) Representative wound bed images of CD31 stained IHC field (10x magnification) on day 4 and 7 post wounding for all the groups (scale bar = 200 µm). (C, D) Quantification of αSMA+ and CD31+ pixels per 10x field respectively in the granulation area (wound bed) of wounds treated with Tegaderm saline, silk sealant saline, Tegaderm histamine, and silk sealant histamine on day 4 and 7 post wounding. At least six non-overlapping fields were quantified for each group and data shown are mean ± standard error of mean of n = 3 mice per group. Statistical significance was determined using two-way ANOVA with Fisher's LSD post-hoc analysis. Individual p-values between groups are shown in the plot.

5.3.3 Silk fibroin sealant, histamine and their combination modulate EMT response in acute wounds

Re-epithelialization is a crucial early step in wound healing, partially preceding myofibroblast activation and wound contraction. Successful re-epithelialization requires the inward mobility of keratinocytes in the epidermis to create a neoepidermis covering wound granulation tissue. Adherens junctions and other cell anchorage features limit the mobility of keratinocytes during the process of mobility(Pastar et al., 2014). Transient, reversible relaxation of cell anchor proteins in a process generally recognized as a partial epithelial-to-mesenchymal transition (EMT) in the epidermis has been identified as a fundamental, early step to re-epithelialization(Haensel & Dai, 2018; Kuwahara et al., 2001). We investigated several molecular partners in the epidermal EMT pathway to evaluate whether this component of healing was augmented by silk and histamine treatment (Figure 5-3A, C, E). Immunohistochemical analysis of phosphorylation of the broad transcriptional regulator STAT3 (pSTAT3) indicated a histamine-dependent (i.e., with or without silk) increase in percentage of keratinocytes with nuclear pSTAT3 at day 2 post-wounding (Tegaderm saline vs Tegaderm histamine *p-value 0.08*, silk vs silk histamine *p <0.05,* Figure 5-3B). In contrast, silk alone was not statistically significant versus Tegaderm treatment (*p-value ns*, Figure 5-3B). Slug is a key transcription factor in the EMT pathway normally not expressed in healthy skin. Molecular evidence indicates that STAT3 is the transcriptional regulator for Slug activation(Lin et al., 2018). We found a time-dependent increase in nuclear Slug signal by immunohistochemistry in wound tongue keratinocytes as early as 6 hours post-wounding (Figure

5-3D). Slug trended towards increased expression and nuclear localization wounds treated individually with silk and histamine and was statistically significantly higher in the combination of silk and histamine versus Tegaderm alone at 2 days post-wounding (silk histamine vs Tegaderm saline, $p < 0.05$, Figure 5-3D). Levels began to successively drop at days 4 and 7 post-wounding, in line with the previously described kinetics of EMT in mouse dermal wounds (Figure 5-3D) (Kuwahara et al., 2001). Activation of Slug reduces the expression of E-cadherin at the transcription and translation level and is a key hallmark of EMT(Batlle et al., 2000; Hudson et al., 2009; Pan et al., 2016). We found that the number of keratinocytes at the wound edge which lost E-cadherin tracked with the timeline of Slug activation by IHC analysis. Interestingly, while individual treatment with silk or histamine did not statistically significantly affect the number of E-cadherin-modulated keratinocytes, the combination of silk and histamine dramatically increased keratinocytes exhibiting EMT by 2 days post-wounding (silk histamine vs Tegaderm saline, $p < 0.05$), continuing to day 4 and resolving by day 7 (Figure 5-3F). Altogether, these data indicate that silk and histamine partially affect markers of EMT in healthy, acute wounds (i.e., non-impaired wounds), and that the combination of silk and histamine synergistically enhanced the process of EMT in keratinocytes at the wound edge. These findings may explain in part the enhanced acceleration of closure in mice treated with the silk and histamine combination.

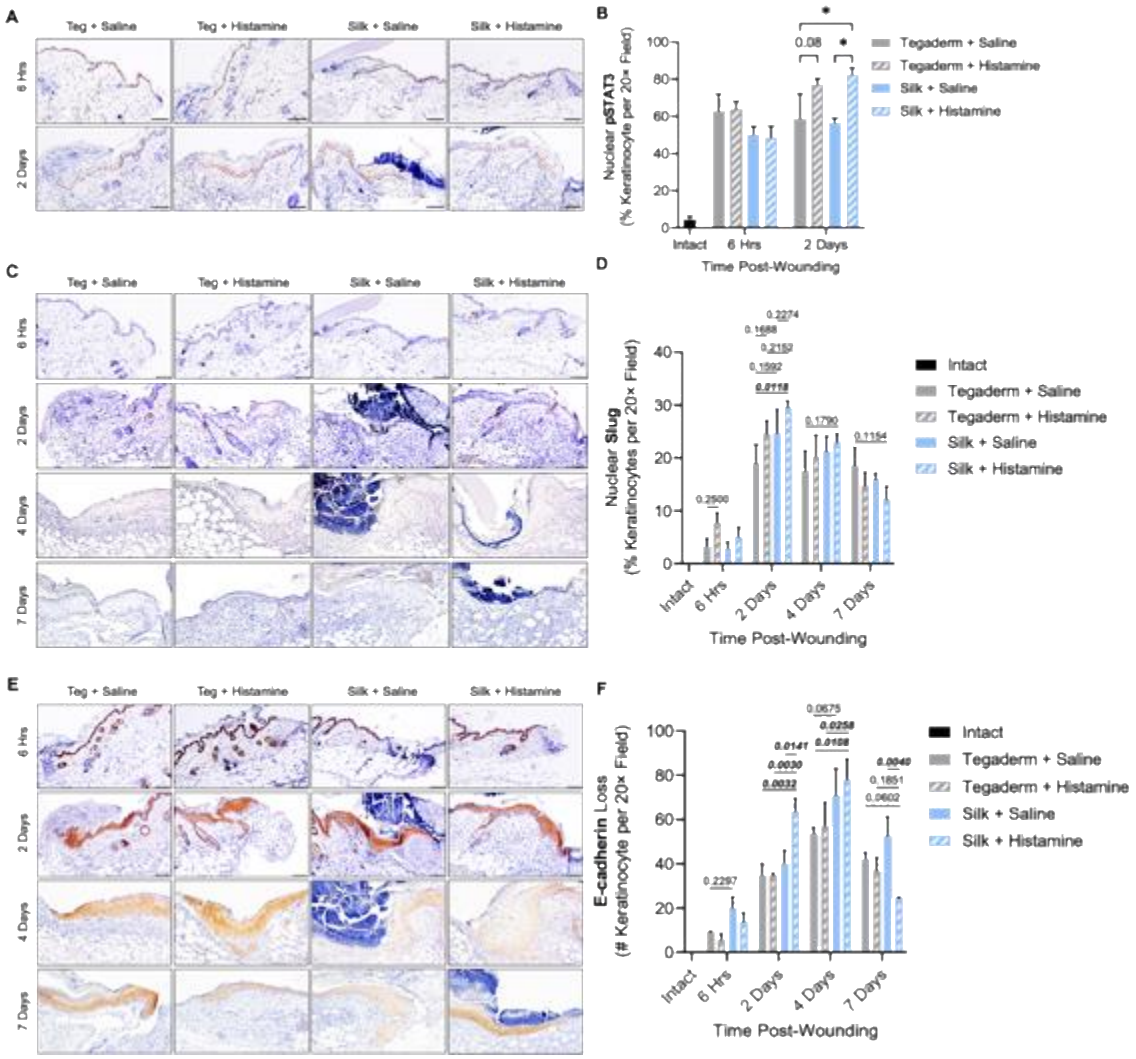

Figure 5-3. Effect of silk sealant, histamine and their combination on modulation of EMT in acute wounds.

(A) Representative micrographs of the epithelial tongue stained for pSTAT3 (20x magnification) at 6 hours and day 2 post wounding for all the groups (scale bar = 200 µm). (B) Quantification of % keratinocytes with positive nuclear pSTAT3 signal per 20x field. (C) Representative micrographs of the epithelial tongue stained for Slug (20x magnification) at 6 hours, day 2, 4, and 7 post wounding for all the groups (scale bar = 200 µm). (D) Quantification of % keratinocytes with positive nuclear Slug signal per 20x field. (E) Representative micrographs of the epithelial tongue stained for E-cadherin (20x magnification) at 6 hours, day 2, 4, and 7 post wounding for all the groups (scale bar = 200 µm). (F) Quantification of number of keratinocytes with loss of E-cadherin signal at the cell boundaries per 20x field. At least four non-overlapping fields were quantified for each group and data shown are mean ± standard error of mean of n = 3 mice per group. Statistical significance was determined using two-way ANOVA with Fisher's LSD post-hoc analysis. Individual p-values between groups are shown in the plot.

5.3.4 Silk fibroin sealant, histamine and their combination modulate innate immune response in acute wounds

Immune cells play a complex, orchestrated role in the process of dermal healing. Regulated polarization, mobilization and clearance of immune cells is thought to be a critical component for healthy healing. Canonical understanding of immune cell infiltration in wounds involves the earliest and most abundant presence by neutrophils concurrently with a smaller population of pro-inflammatory (M1) macrophages. Subsequently, neutrophil presence drops in the wounds and M1 macrophages are repolarized to pro-resolution (M2) macrophages(Eming et al., 2014; Larouche et al., 2018). Wounds were stained for Ly-6G, iNOS, and Arginase-1 (Arg-1) which can be used as one of the markers to identify neutrophils, M1 macrophages, and M2 macrophages, respectively on days 2, 4, and 7 post-wounding (Figure 5-4 A, C, E). We found that silk, histamine or their combination did not have any significant effect on iNOS-expression M1 macrophages during the first 7 days of healing (Figure 5-4D). Analysis of Arginase-1-expression M2 macrophages suggests a delayed polarization of macrophages to the M2 state, with tegaderm saline exhibiting the highest levels at day 4 post-wounding. Interestingly, treatment with silk or silk and histamine combination resulted in a delayed, significantly increased presence of M2 macrophages on day 7 post-wounding, suggesting an augment polarization profile over the course of healing mediated by the presence of silk in the wound bed (Tegaderm saline vs silk saline $p < 0.05$, Tegaderm histamine vs silk histamine $p < 0.05$, Figure 5-4B). Probing for Ly6G-positive neutrophils demonstrated that silk had a robust effect on neutrophil presence in the wound (Tegaderm saline vs silk saline $p < 0.05$, Figure 5-4F). While Tegaderm or histamine treatment alone had no effect on Ly6G cell counts over a period of 7 days, silk alone dramatically increases neutrophils at day 2 post-wounding, with a slower and sustained resolution of cell presence over the course of 7 days. Interestingly, the combination of silk and histamine resulted in a sustained, elevated neutrophil presence over the course of 7 days of healing with no indication of resolution over the course of our analysis (Tegaderm saline vs silk histamine $p < 0.05$, Tegaderm histamine vs silk histamine $p < 0.05$, Figure 5-4F). Ly6G is a universal marker for neutrophils, and it will be important to understand the N1/N2

polarization state of these neutrophils in further study. Evidence suggests a pro-healing effect of increased N2-polarized neutrophils (Ym1-expressing) in healing wounds(Peiseler & Kubes, 2019). Another study reported following myocardial infraction (MI), N2 polarized neutrophils ($Ly6G^{+}CD206^{+}$) increased during the later phases (day 3, 5, and 7 compared to day 0 and 1) following MI injury which helped with inflammation resolution and wound repair(Ma et al., 2016). Taken together, these data indicate that exogenous treatment with histamine has little, if any, effect on immune cell behavior in healing wounds, while silk treatment augments the timeline of cellular polarization and infiltration in wounds. These may indicate key effects on immune-mediated effects in healing and represent opportunities to target specific immune cell populations to further enhance the healing process.

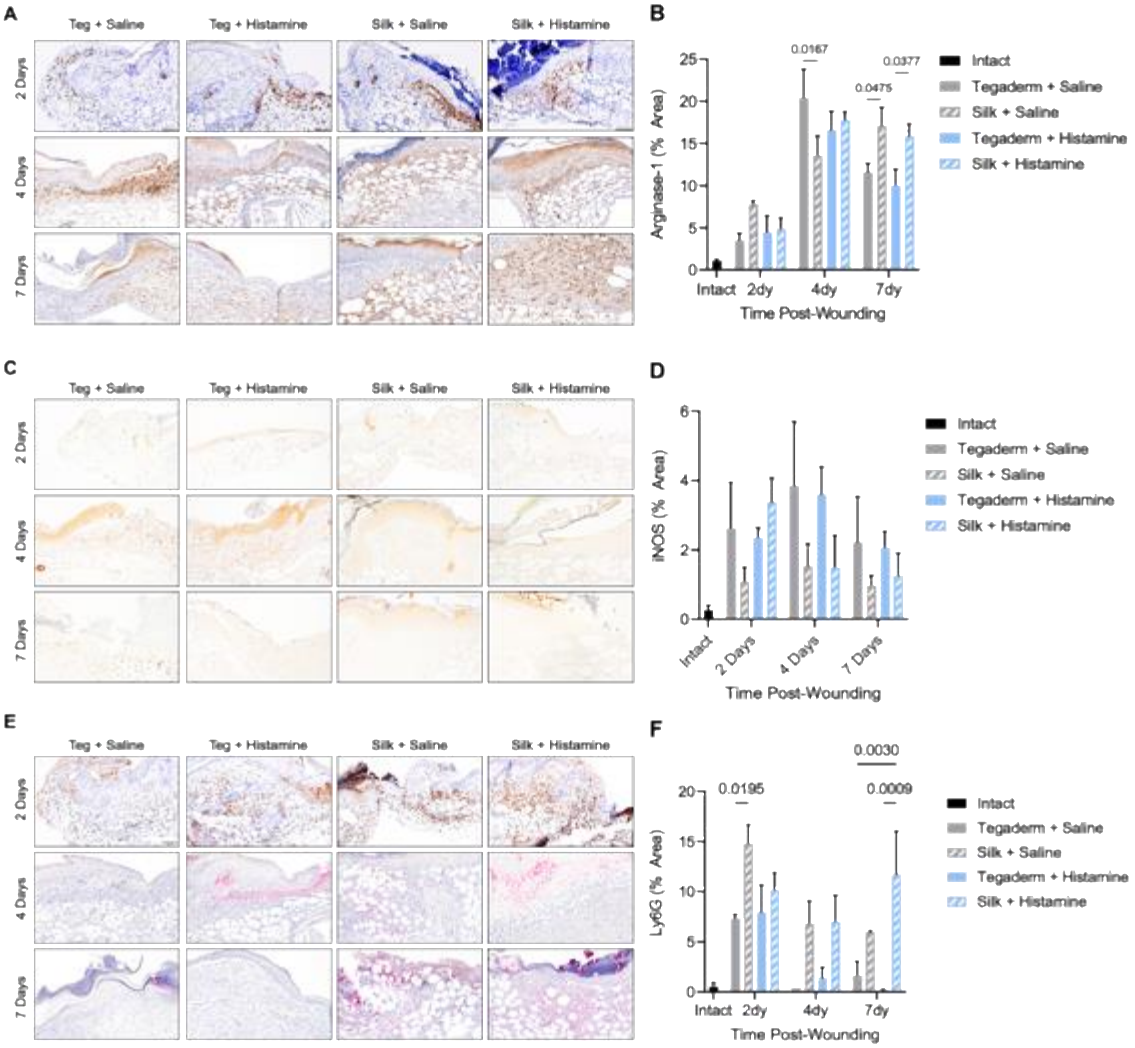

Figure 5-4. Effect of silk sealant, histamine and their combination modulate innate immune response in acute wounds.
Representative wound bed micrographs of Arginase-1 stained IHC field (20x magnification) on day 2, 4, and 7 post wounding for all the groups (scale bar = 200 µm). (B) Quantification of % Arginase-1 positive signal per 20x field. (C) Representative wound bed micrographs of iNOS stained IHC field (20x magnification) on day 2, 4, and 7 post wounding for all the groups (scale bar = 200 µm). (D) Quantification of % iNOS positive signal per 20x field. (E) Representative wound bed micrographs of Ly-6Gstained IHC field (20x magnification) on day 2, 4, and 7 post wounding for all the groups (scale bar = 200 µm). (F) Quantification of % Ly-6G positive signal per 20x field. At least four non-overlapping fields were quantified for each group and data shown are mean ± standard error of mean of n = 3 mice per group. Statistical significance was determined using two-way ANOVA with Fisher's LSD post-hoc analysis. Individual p-values between groups are shown in the plot.

5.3.5 Silk fibroin sealant, histamine and their combination promote diabetic wound healing and biomechanical recovery

We also analyzed the effect of silk fibroin sealant, histamine and their combination on treatment of splinted full thickness wounds in diabetic and obese mice (BKS.Cg *Dock7*^{m} +/+ *Lepr*^{db}/J) which is a model of diabetic wounds(Grada et al., 2018; Michaels et al., 2007). The gross appearance of the wounds treated with Tegaderm and silk fibroin sealant in combination with saline or histamine are shown at intermediate time points post-wounding (Figure 5-5A). The single dose of histamine was adjusted to 81.6 mM histamine dihydrochloride in 10 µL saline to maintain a similar dose of 3.4 mg/kg per mouse based on the average body weight of the diabetic mouse (~40 g). Daily planimetric measurements were performed to track wound closure over time using normalized wound areas. Tegaderm saline control wounds exhibited ~70% closure at day 11 post wounding, whereas silk fibroin sealant resulted in ~90% wound closure (p= 0.0001, n=4, Figure 5-5B). Single dose of histamine further accelerated wound closure both in combination with Tegaderm dressing and silk fibroin sealant, resulting in ~85% and 97% wound closure respectively (Figure 5-5B).

Similar to the effect observed in case of acute wounds, single dose of histamine improved biomechanical strength and recovery of healed skin in diabetic wounds also. Along with improved wound closure, silk fibroin sealant-histamine treated wounds showed highest recovery of healed skin strength at day 11 post wounding (643.4 ± 21.18 kPa, 49.2% recovery) whereas Tegaderm

saline treated control wounds only resulted in a strength of 275.9 ± 16.50 kPa and 21.1% recovery within the same 11-day period (Figure 5-5C).

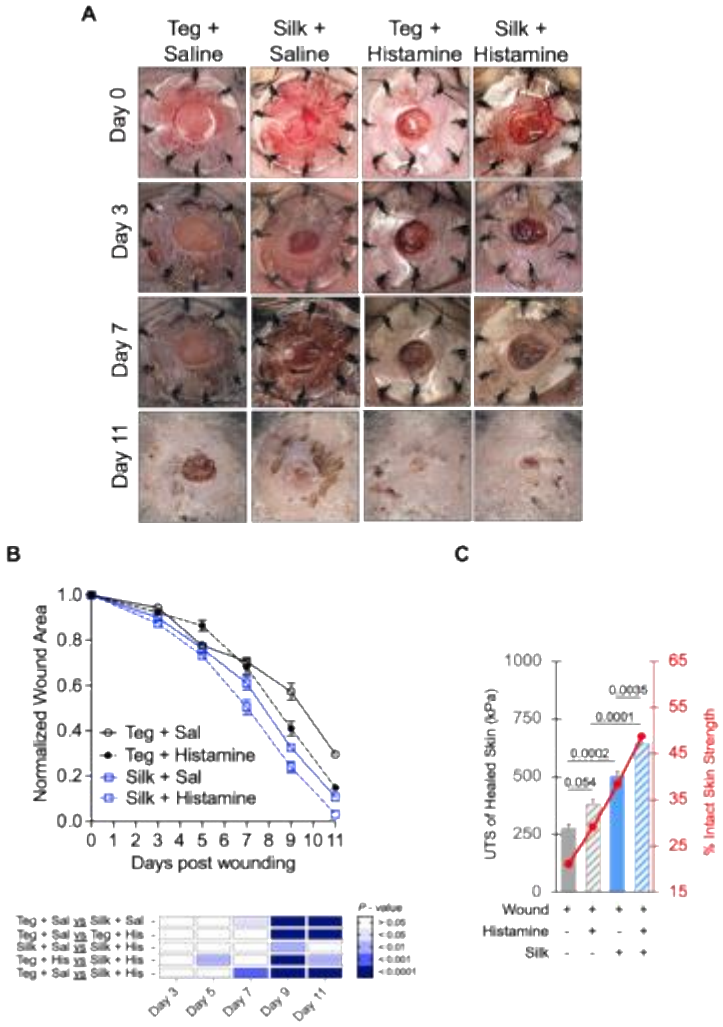

Figure 5-5. Silk sealant, histamine and their combination promote diabetic wound healing. (A) Representative wound images of Tegaderm saline, silk sealant saline, Tegaderm histamine, and silk sealant histamine wounds on day 0, 3, 7, and 11 post wounding. (B) Planimetric measurement of wound areas on day 0, 3, 5, 7, 9, and 11 normalized to day 0 for each mouse. Data shown are mean ± standard error of mean of n = 4 mice per group. Statistical significance was determined using one-way ANOVA with correction for multiple comparisons by Holm-Sidak method. Individual p-values between groups on individual days post wounding are shown using a color-coded heat-map. (C) Plot showing ultimate tensile strength and % recovery of healed skin strength (secondary y-axis) 11-days post wounding. Data shown are mean ± standard error of mean of n = 4 mice per group. Statistical significance was determined using one-way ANOVA with correction for multiple comparisons by Tukey method. Individual p-values between groups are shown in the plot.

5.3.6 Effect of temporal delivery of second therapeutic in acute wounds

The timeline for the delivery of second bioactive was chosen based on the wound healing kinetics (planimetry data) for acute wounds treated with silk sealant-histamine and Tegaderm-histamine (Figure 5-1A). Upon plotting the rate of healing (dA/dT, wound area/time) with respect to days post wounding, we observed a peak in the healing response around day 4 post-wounding and topical application of histamine along with silk sealant or Tegaderm dressing. This observation was consistent both in case of silk sealant and Tegaderm covered wounds, although the rate of healing was higher in silk sealant covered wounds (Figure 5-6A). We posit the day where the rate of healing peaks coincides with the transition period where the wound might be switching from an early phase of healing to a late phase of healing. In case of acute wounds in BALB/c mice, this transition period was day 4 post-wounding, and we delivered the second therapeutic a day prior to the transition window (i.e., day 3 post-wounding) to maximize the availability of the delivered therapeutic around the transition period. In case of acute wounds, our choice of second therapeutic is a fusion peptide SDF1-ELP (stromal cell-derived growth factor-1) which self assembles into nanoparticles at ~37 °C, this would allow the nanoparticles to act as growth factor depots with release over an extended period of time. The SDF1-ELP after self-assembly forms ~600 nm sized particles, have similar binding characteristics to CXCR4 receptor as free SDF1, improved stability in wound fluid compared to free SDF-1, and also improved wound healing outcomes in murine model of diabetic wounds(Yeboah et al., 2016; Yeboah et al., 2017).

SDF1-ELP nanoparticles were delivered on day 0 and 3 post-wounding in conjugation with silk sealant and with or without histamine to evaluate the role of temporal delivery in acute wounds (Figure 5-6B). Daily planimetric measurements were performed and normalized wound area was calculated everyday post wounding to track wound closure over time (Figure 5-6C). Silk sealant treated wounds with temporal delivery of a single dose of SDF1-ELP (2000 nM concentration in 20 µL of saline) either on day 0 or 3 post-wounding achieved ~81% and ~89% wound closure by day 7 post-wounding. Topical histamine treatment during wounding along with silk sealant resulted in slightly improved wound closure around ~91% by day 7 post-wounding.

Whereas, combining a second therapeutic, SDF1-ELP along with histamine and silk sealant did result in improved wound closure based on the day when the second therapeutic was delivered, ~93% wound closure for simultaneous treatment (SDF1-ELP and histamine delivered on day 0 post-wounding) and ~98% wound closure for subsequent treatment (histamine on day 0 post-wounding and SDF1-ELP on day 3 post-wounding) (Figure 5-6C).

We compared the wound healing kinetics of the simultaneous and sequential treatments with the kinetics of single treatments (SDF1-ELP alone on day 0 or 3 post-wounding, histamine alone on day 0 post-wounding). The simultaneous treatment of bioactives resulted in accelerated wound closure from day 5 post-wounding onwards compared to SDF1-ELP treatment alone either on day 0 or day 3 post-wounding. Compared to histamine alone treatment on day 0 post-wounding, simultaneous treatment of bioactives showed a modest improvement in healing kinetics only on day 5 post-wounding and at the end of the study a similar wound closure profile was observed (Figure 5-6C, heat map). Whereas, if the bioactives were delivered in a sequential manner (histamine on day 0 post-wounding and SDF1-ELP nanoparticles on day 3 post-wounding), improved kinetics of wound closure was observed from day 4 onwards post-wounding compared to SDF1-ELP alone treated wounds and this was sustained for the rest of the healing period. Similar improvement in wound healing was observed compared to histamine alone treatment and a significant improvement in kinetics was obtained on days 6 and 7 post-wounding. Finally, comparing the healing kinetics of simultaneous and subsequent treatment of bioactives, a modest improvement of wound closure was observed from day 5 post-wounding, but no significant acceleration was observed except on day 6 post-wounding (Figure 5-6C, heat map).

The biomechanical recovery of healed skin strength at day 7 post-wounding from different treatment groups and % recovery in strength compared to intact skin strength (control skin, no wounding) were plotted (Figure 5-6D). Higher tensile strength of healed skin was observed in wounds treated with a combination of bioactives, both in a simultaneous and sequential compared to similar treatments. This finding is consistent with our wound closure kinetics as improved wound closure would result in higher biomechanical recovery (Figure 5-6C). Compared

to control intact skin strength, healed skin from simultaneous and sequential bioactive treatment group achieved ~51% (1022.08 ± 56.5 kPa) and ~53% (1062.07 ± 101.9 kPa) recovery in skin strength, respectively. Whereas the individual treatments of SDF1-ELP achieved ~24% (488.94 ± 61.4 kPa) and ~32% (646.53 ± 67.8 kPa) of healed skin strength recovery in comparison to control skin (Figure 5-6D). Taken together, the kinetics of wound closure and healed skin biomechanical strength recovery suggest that a combination of bioactives if delivered in a temporal manner to work in targeted phases of wound healing can further benefit the wound healing outcomes in acute wounds.

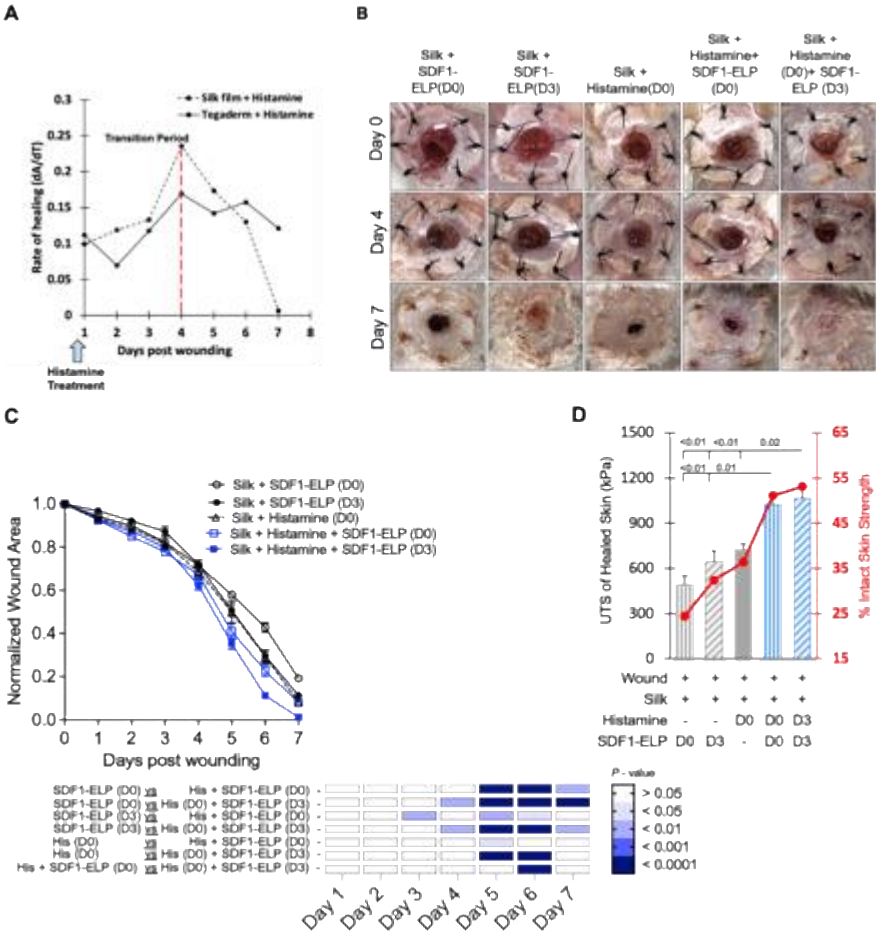

Figure 5-6. Temporal delivery of second therapeutic along with silk sealant in acute wounds. (A) Rate of healing plot of silk sealant-histamine and Tegaderm-histamine treated acute wounds obtained from the healing kinetics in Figure 5-1B. The day with the maximum healing rate is shown using a red dashed line. (B) Representative wound images of silk sealant treated wounds along with temporal delivery of SDF1-ELP nanoparticles (day 0 or 3 post-wounding), histamine (day 0 post-wounding), and

combination of histamine with SDF1-ELP (day 0 or 3 post-wounding) on day 0, 4, and 7 post wounding. (C) Daily planimetric measurement of wound areas normalized to day 0 for each mouse. Data shown are mean ± standard error of mean of n = 6 mice per group (n=5 for silk sealant – SDF1-ELP D0 group). Statistical significance was determined using one-way ANOVA with correction for multiple comparisons by Holm-Sidak method. Individual p-values between groups on individual days post wounding are shown using a color-coded heat-map. (D) Plot showing ultimate tensile strength and % recovery of healed skin strength (secondary y-axis) 7-days post wounding. Data shown are mean ± standard error of mean of n = 4 mice per group. Statistical significance was determined using one-way ANOVA with correction for multiple comparisons by Tukey method. Individual p-values between groups are shown in the plot**.**

5.3.7 Effect of temporal delivery of second therapeutic in diabetic wounds

Similar to temporal delivery of second therapeutic in acute wounds, the day for the delivery of second bioactive was chosen based on the wound healing kinetics (planimetry data) for diabetic wounds treated with silk sealant-histamine and Tegaderm-histamine (Figure 5-5B). In this case, the rate of healing indicated day 7 post-wounding as the transition period. Accordingly, the second therapeutic was delivered on day 6 (a day prior to the transition period), day 0 (along with the first therapeutic right after wounding), and on day 3 post-wounding (somewhere in middle from the wounding to the transition period) (green arrows, Figure 5-7A). We delivered FGF2-ELP fusion peptide which self assembles into nanoparticles ~240nmin diameter at ~37 °C. FGF2 has been previously shown to promote angiogenesis, formation of granulation tissue, migration of fibroblasts, and tissue remodeling which are hallmarks of late stage tissue repair (Akita et al., 2013; Barrientos et al., 2008; Makino et al., 2010).

5-mm full-thickness wounds were treated with histamine and silk sealant followed by FGF2-ELP as the second therapeutic (2000 nM concentration in 20 µL of saline) either on day 0, day 3 or day 6 post-wounding (Figure 5-7B). Planimetric measurements were performed on days 0, 3, 5, 7, 9 and 11 and normalized wound areas were calculated to track wound closure over time (Figure 5-7C). Individual treatment of wounds FGF2-ELP along with silk sealant and without histamine were also performed as controls for the combination treatment of therapeutics to assess wound repair. During the course of the healing, FGF2-ELP delivered on day 0 along with the silk sealant and histamine achieved ~88.5% by day 11 post-wounding whereas FGF2-ELP delivered

on day 3 and day 6 post-wounding resulted in complete wound closure indicating accelerated closure (Figure 5-7C). Whereas, in case of day 6 treatment of FGF2-ELP almost complete wound closure was achieved by day 9 post-wounding compared to ~85% on the same day in the day 6 FGF2-ELP treated wounds (Figure 5-7C). This is significant as it shows delivery of FGF2-ELP closer to the transition period was able to improve wound closure kinetics by almost 2 days compared to its delivery during wounding or earlier when the wound bed is not primed for transition towards late healing stage. The biomechanical recovery of healed skin from different treatment groups followed a similar trend to the wound closure. The healed skin strength and % recovery in strength compared to intact skin strength (control skin, no wounding) at day 11 post-wounding were plotted (Figure 5-7D). Higher healed skin was observed in groups which where combination of therapeutics was used along with silk sealant compared to individual treatment of FGF2-ELP or histamine alone. Within the combination treatments, day 6 delivery of FGF2-ELP resulted in ~55% recovery of healed skin strength (805.34 ± 29.5 kPa) compared to intact skin (1460.61 ± 224.46 kPa) and is higher that combination treatment with day 0 delivery of FGF2-ELP (692.55 ± 19.77 kPa, ~47% recovery) (Figure 5-7D).

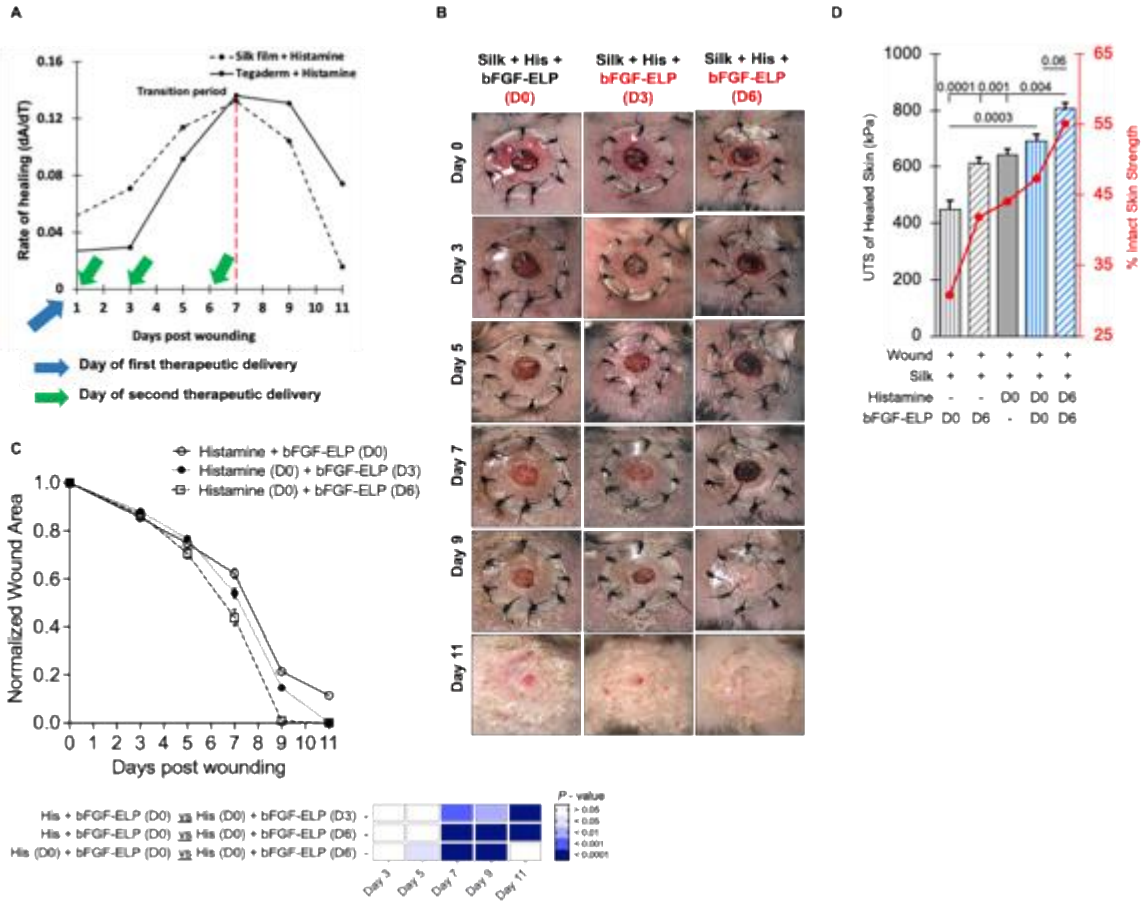

Figure 5-7. Temporal delivery of second therapeutic along with silk sealant in diabetic wounds.

(A) Rate of healing plot of silk sealant-histamine and Tegaderm-histamine treated diabetic wounds obtained from the healing kinetics in Figure 5-5B. The day with the maximum healing rate is shown using a red dashed line. (B) Representative wound images of silk sealant treated wounds along with temporal delivery of bFGF-ELP nanoparticles (day 0 or 6 post-wounding), histamine (day 0 post-wounding), and combination of histamine with bFGF-ELP (day 0 or 6 post-wounding) on day 0, 3, 5, 7, 9, and 11 post wounding. (C) Planimetric measurement of wound areas on day 0, 3, 5, 7, 9, and 11 normalized to day 0 for each mouse. Data shown are mean ± standard error of mean of n = 3 mice per group. Statistical significance was determined using one-way ANOVA with correction for multiple comparisons by Holm-Sidak method. Individual p-values between groups on individual days post wounding are shown using a color-coded heat-map. (D) Plot showing ultimate tensile strength and % recovery of healed skin strength (secondary y-axis) 7-days post wounding. Data shown are mean ± standard error of mean of n = 4 mice per group. Statistical significance was determined using one-way ANOVA with correction for multiple comparisons by Tukey method. Individual p-values between groups are shown in the plot.

5.4 CONCLUSIONS

Herein this study shows an approach for combining the benefits of a silk-fibroin sealant dressing and exogenous topical delivery of histamine for enhancing full-thickness wound repair outcomes in acute and diabetic wounds. Silk fibroin sealant modulated immune cell activity in the wound bed and with or without histamine had a more sustained reparative immune cell population towards the late stages of healing. The effect of topical delivery of histamine was more pronounced in modulating transient epithelial EMT response during the early stages of healing and myofibroblast activity in the granulation tissue during healing. Our results are in concert with acceleration of wound closure kinetics and modulation of transient epithelial EMT. We also show the potential of delivery of a second therapeutic in a temporal manner can further augment the healing response. This is significant as this help design strategies to deliver specific therapeutic to prevent wounds from moving towards chronicity. As a proof-of-concept we strategized temporal delivery based on rate of wound healing, but additional studies will be required to map the transition period to specific markers sampled from the wound either probing using histological techniques or based on phase-dependent immune response. Also, evaluating the benefit of histamine as a bioactive and in combination with another therapeutic will be evaluated in a larger animal model to evaluate its translational potential.

CHAPTER 6: ADDITIONAL DEVELOPED METHODS: LIGHT-ACTIVATED SEALANT(LASE) FOR COLORECTAL DEFECT REPAIR

6.1 INTRODUCTION AND BACKGROUND

Anastomotic leakages (AL) are still the biggest concern following colorectal surgeries and the incidence rate varies between 3 % to 28%, depending on the location of the anastomotic site either colonic or rectal resection(Snijders et al., 2012). The mortality rate has not changed over the years. Postoperative AL can result in extended hospital stays, secondary interventions, need for correction surgeries, and higher chances of related complications in the future(Schiff et al., 2017). Limitations of specific diagnostic tools and markers limits the timely detection of AL and further warrants the need of closure devices minimizing occurrences of AL(Panda et al., 2020; Slieker et al., 2013). The economic burden of AL can be significant. In a previous study it was reported that the cost of AL per 1000 patients in US was $28.6 million in hospitalization and readmission costs alone(Hammond et al., 2014). Different approaches have been investigated along with convention suturing of bowel to reduce the occurrence of AL; suture/staple line reinforcements, glues and sealants(Costales et al., 2018; Sdralis et al., 2020), wrapping of omentum over the anastomotic site following closure(Hoeppner et al., 2010; Pommergaard et al., 2012), use of intraluminal devices along suture/staple line(Bakker et al., 2017; De Hous et al., 2020), etc. but none of these alternative approaches have been implemented as a preventive measure for AL based on clinical findings.

An ideal sealant for internal organ use will have the following characteristics: ease of application, robust adhesion to tissue surface under moist conditions, controlled swelling, good biocompatibility, combat bacterial growth, and potential matrix functionalization for bioactive delivery for aiding the repair process. Chitosan has been extensively studied as a wound dressing and its excellent mucoadhesive properties has led to its use as an ideal tissue sealant under wet

conditions in the form of films, hydrogel, electrospun mats, etc. (Fujie et al., 2010; Lauto et al., 2012; Lu et al., 2018).

In this study, we have developed a chitosan-based sealant which can be light-activated using a near-infrared (NIR) laser to achieve sealing of incisional colorectal defects. Indocyanine green (ICG) dye embedded in the light-activated sealant (LASE) matrix absorbs NIR laser light and convert it to heat, which leads to LASE-tissue adhesion at the incision site and sealing of the incision. Our studies demonstrate that swelling behavior of LASE can be controlled via crosslinking to minimize sealant failure. Application of LASE followed by laser irradiation resulted in improved wound closure strength can Tachosil closed intestine and leak pressure compared to sutures under *ex vivo* conditions immediately following sealing and extended time period (up to 24 hours). Thorough ex vivo evaluation LASE demonstrated superior adhesion to intestines under wet tissue conditions and could potentially be used as a tissue sealant alone or as a secondary reinforcement for suture/staple line.

6.2 MATERIALS AND METHODS

6.2.1 Materials

Chitosan (#419419, high molecular weight, 85% deacetylation), acetic acid, glacial (#695092), and glycerol (#G7893) were purchased from Millipore Sigma (St. Louis, MO). Glutaraldehyde (#G0068, *ca*. 50% in water, *ca*. 5.6 mol/L) was purchased from TCI America for crosslinking of chitosan. Indocyanine green (ICG) dye was purchased from MP Biomedicals (#ICN15502050). All solutions were freshly prepared in nanopure water (NPW, resistivity ~ 18.2 MΩ-cm, Millipore filtration system, Darmstadt, Germany). Reagents were either stored at room temperature or in fridge as suggested in the MSDS. Cadaver porcine small intestine were procured from local abattoir and were thoroughly disinfected and cleaned prior to use. Rats (SAS Sprague Dawley, strain #400) were purchased at 8 weeks from Charles River Laboratories (Wilmington, MA, USA). Commercially-

available 7-0 Maxon™ monofilament absorbable sutures (Medtronic, Minneapolis, MN) were purchased from esutures.com (product #6145-01, Mokena, IL).

6.2.2 LASE fabrication and processing

LASE were fabricated from chitosan (high molecular weight, 85% deacetylation) by solvent casting methods. Briefly, 204 mg of chitosan powder was dissolved using in 12 mL of acetic acid (0.5% v/v in NPW) containing 240 µL of ICG (5mM stock in NPW) and stirred on a magnetic stir plate set to ~50 °C until a clear homogenous 1.7 wt% chitosan solution with 0.1 mM final concentration of ICG dye was obtained.

For fabricating crosslinked chitosan LASE, varying amounts of glutaraldehyde solution was added to the previously prepared chitosan-ICG solution and further stirred for 30 minutes to ensure homogenous mixing of the crosslinker. Following this, glycerol (10% v/v, final solution volume) was added to the crosslinked chitosan-ICG solution and stirred for another 15 minutes. This solution was degassed and sonicated to remove any bubbles and individual films were casted using 3mL of the solution on 40 mm * 22 mm glass coverslips. The films were cast in a biohood until dry (~48 hours). Non-crosslinked films were fabricated in a similar manner without the addition of glutaraldehyde to the chitosan-ICG solution.

The as-prepared crosslinked LASE films were further neutralized and washed to remove excess glutaraldehyde. Briefly, the dried LASE films were incubated in a neutralization buffer (0.21 M NH_4OH solution in NPW with 0.1 mM ICG, pH ~11.3) under continuous stirring on an orbital shaker (~50 RPM) for 30 minutes. This wash step was repeated again in a freshly prepared neutralization buffer (0.21 M NH_4OH solution in NPW with 0.1 mM ICG, pH ~11.3) for 30 minutes. Following two washes in the neutralization buffer, LASE were washed further in 1x PBS (with 0.1 mM ICG, pH ~7.4) under continuous stirring on an orbital shaker (~50 RPM) for 15 minutes and the change in pH of the solution was noted. This wash step was repeated until no significant changes in the pH of the 1x PBS was observed. Next, washed LASE were sandwiched between

two coverslips and dried inside a biohood (~48 hours). LASE after drying until was stored in RT until further use.

6.2.3 Swelling behavior

Dried uncrosslinked and crosslinked LASE cut to uniform sized square sections (~1cm*1cm) were used for characterizing swelling behavior. To measure swelling ratio of various LASE sections, the initial weight (W_i) of the dried section were measured. These sections were then immersed in 1x PBS (pH ~7.4) and incubated at 37 °C in a humidified chamber under continuous stirring on an orbital shaker (~50 RPM). At predetermined timepoints ranging from 0.25 to 14 days, the LASE section were weighed (W_f) after blotting off excess buffer from the surface. Swelling ratio of LASE sections were calculated as $[(W_f – W_i)/ W_i)$. All swelling ratio studies of LASE sections were carried out with two independent LASE films (n = 2).

6.2.4 Absorbance and photothermal response

Absorbance spectra of ICG solution (0.1 mM), LASE as prepared, and LASE at each step after processing (neutralization and washing steps) were recorded from 400 nm – 999 nm using UV-Vis absorption spectroscopy (Synergy 2 Multi-Mode Reader, BioTek Instruments; Winooski, VT). Absorbance spectra of chitosan film (LASE without ICG) was also recorded as controls for LASE.

A handheld, continuous wave near infrared (NIR) laser (LRD-0808, Laserglow Technologies, North York, Ontario, Canada), coupled with armored optical fiber with FC/PC connector (#AFF2001X, 1m length, and 200 µm core diameter), and tuned to 808 nm was used for laser irradiation. The fixed laser spot size was 2 mm. A FieldMate laser power meter used to measure the power of the laser beam and power density of the laser beam was calculated as the power of the laser beam/area of the laser beam. An A325sc infrared (IR) camera (FLIR, Nashua, NH) with 10 mm 45° lens measured the surface temperature of LASE during laser exposure.

6.2.5 *Ex vivo* porcine intestine adhesion studies: Wound closure strength and Leak pressure

For all our ex vivo studies, fresh porcine small intestine was obtained from a local abattoir and thoroughly washed in deionized water several times to remove any remaining blood/waste matter. The serosal surface of the intestine was used as the substrate for our adhesion studies.

Wound closure strength of LASE was evaluated according to a modified ASTM F2458-05 standard which is a standard test method for wound closure strength of tissue adhesives and sealants(Kim et al., 2020)Ex vivo. Briefly, a ~ 6 cm * 1 cm porcine intestine section was used in this study and cut in half using a razor blade mimicking an injury. Then, a ~2 cm * 1 cm LASE section was applied to cover the wound area and surrounding tissue. Following LASE application, the LASE-intestine area was irradiated for 5 mins using an 808-nm NIR laser (~350 mW) while maintaining a temperature of 55-60 °C at the tissue-LASe interface. During the entire laser irradiation procedure, the intestine was constantly kept moist using 1x PBS to prevent drying/desiccation of tissues. Sealed intestines were either immediately evaluated for wound closure strength following sealing (0 hour) or stored in a humified chamber at 37 °C under continuous stirring on an orbital shaker (~50 RPM) for 6 hour and 24 hour-timepoints to evaluate simulated long-term adhesion. Sealed sections were then clamped onto the grips of the texture analyzer and a uniaxial loading was applied at a strain rate of 2mm/s (tension mode) until failure from the sealed incision site. The force at which failure occurred was defined as wound closure strength (kPa). Sutures a closure device was not used as a control because in this test under ex vivo conditions will not be a true representation of the wound closure strength. We have used Tachosil (collagen patch coated with fibrin sealant) as our commercial control for assessing the wound closure strength of LASE. Tachosil has been previously used alone or in conjugation in suture to evaluate sealing of colorectal anastomoses (Anthis et al., 2021; Nordentoft et al., 2007).

For *ex vivo* leak pressure studies, porcine small intestines were cut into ~6 cm long sections and a centrally placed 1 cm full-thickness incision thorough one lumen of the intestine was made. The incision was either closed with 4-0 Nylon suture (4 simple interrupted knots) or sealed

using LASE. For the LASE group, a ~1.5 cm * 1.5cm LASE section was placed over the incision line and irradiated as mentioned above for the wound closure strength test. During the entire laser irradiation procedure, the intestine was constantly kept moist using 1x PBS to prevent drying/desiccation of tissues. Sealed intestines were either immediately evaluated for leak pressure following sealing (0 hour) or stored in a humified chamber at 37 °C under continuous stirring on an orbital shaker (~50 RPM) for 6 hour and 24 hour-timepoints to evaluate simulated long-term adhesion. To perform leak pressure studies, an in-house fabricated set-up comprising of a digital pressure indicator (#DPI 705, Druck Limited, Leicester, England), syringe pump (#NE-300, New Era Pump Systems Inc., Farmingdale, NY), 60 mL syringe (BD, inside diameter 26.59 mm), and a Y-shaped connector plug to connect the digital pressure indicator with the tissue specimen(Huang et al., 2013; Urie, Guo, et al., 2018b). To visualize fluid leakage, dyed water (deionized with blue tissue marking dye) was infused into the sutured or LASE sealed intestine sections clamped at both ends using a 23G needle at an injection rate of 12.5mL/min. The pressure rise was monitored, and leak pressure was defined as the pressure where visible flow/leakage of dyed water was observed from the closed incision site. Any leakage from the needle insertion site was considered negligible.

6.3 RESULTS

6.3.1 Generation and characterization of LASE

Light-activated sealant (LASE) comprising of chitosan, indocyanine green (ICG) dye, glutaraldehyde (used as a crosslinker in case of crosslinked films), and glycerol was fabricated using solvent casting method. The as is prepared LASE were ~25 µm thick. Following fabrication, swelling ratio of various LASE was evaluated to evaluate their swelling behavior under hydrated conditions. All the crosslinked LASE (increasing glutaraldehyde concentration from 1 to 4) showed ~2-3 folds less swelling compared to uncrosslinked films over a 14-day period. Crosslinked LASE

4 had ~5-fold lower swelling after 14-day incubation in 1x PBS compared to uncrosslinked film at the same timepoint (Figure 6-1A).

We also investigated changes in swelling behavior of crosslinked LASE 4 following processing (neutralization and washing) steps compared to as-is prepared crosslinked LASE 4. As-is prepared crosslinked LASE 4 had ~2-fold higher swelling within the first 6 hours compared to processed LASE 4 and maintained significant lower swelling (~3 fold) over a 14-day period (Figure 5-1B). Neutralization of chitosan films have been shown to significantly reduce swelling of films and this is attributed to increased hydrophobicity of chitosan films due to deprotonation of $—NH_3^+$ groups to $—NH_2$ during neutralization in a basic buffer(Chang et al., 2019; Sangsanoh & Supaphol, 2006). Glutaraldehyde crosslinking followed by neutralization of chitosan has been reported to reduce swelling and improve mechanical properties of chitosan films(Frick et al., 2018; Liu et al., 2019).

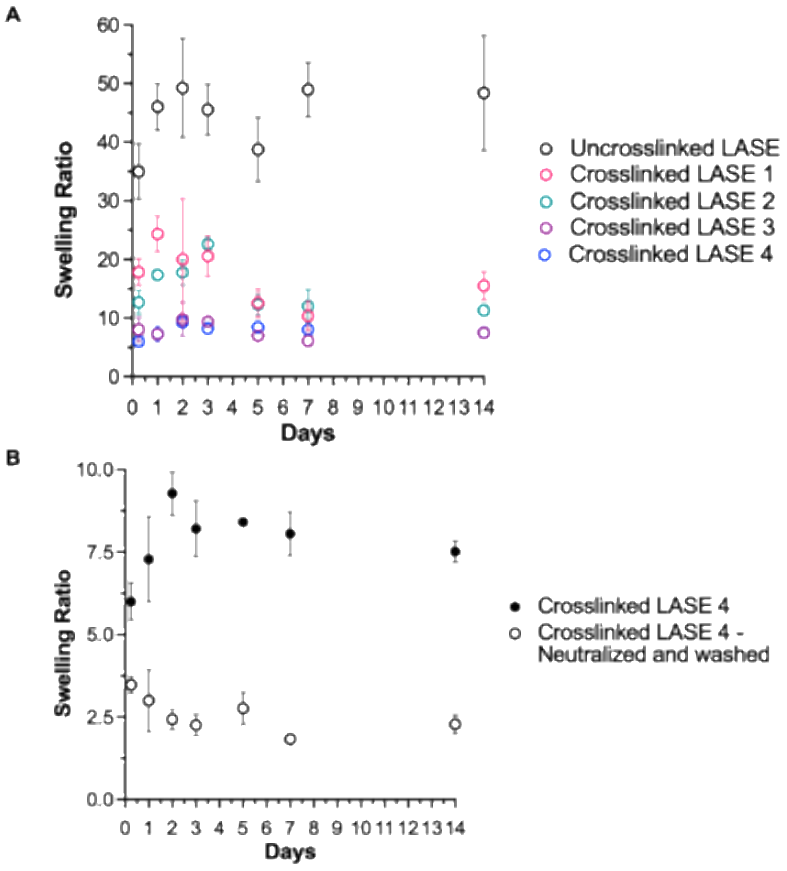

Figure 6-1. Swelling behavior of LASE.
(A) Swelling ratio of uncrosslinked and crosslinked LASE at pre-determined timepoints incubated in 1x PBS (pH ~7.4) at 37 °C in a humidified chamber under continuous stirring on an orbital shaker (~50 RPM). (B) Swelling ratio of an as-prepared crosslinked LASE (LASE 4) compared with neutralized and washed crosslinked LASE (LASE 4). Data shown are mean ± standard error of the mean of n = 2 independent LASE sections.

Processed LASE after the neutralization and washing steps maintains its absorbance similar to characteristic ICG dye absorbance peak and as-is prepared LASE. A minor drop is absorbance is observed during the processing steps, but no significant drop-off was noted (Figure 6-2A). Maintaining the characteristic ICG dye absorbance peak warrants the use of processed LASE for photothermal mediated tissue sealing application.

Photothermal response of processed LASE to a continuous wave handheld near-infrared (NIR) laser tuned to 808 nm irradiated in a 30 s laser “on” and 15 s laser “off” cycle for a total of three cycles was investigated. For the photothermal response studies, a LASE section was applied to an ex vivo porcine small intestine and the surface temperature was recorded using an infrared (IR) camera. Upon irradiation with laser, a rapid increase in surface temperature of the LASE-tissue interface was observed due to efficient photothermal conversion of the embedded ICG dye in the LASE matrix. This photothermal response was reproducible over three cycles and varied using different laser power densities (1.6 to 2.4 W/cm^2) (Figure 6-2B). Irradiation of LASE without ICG even at the highest laser power density tested (2.4 W/cm^2) did not result in any photothermal response (red dotted line, Figure 6-2B). Surface temperatures in the range of 50–60 °C (shown using blue shaded region) optimal for tissue sealing was achieved by modulating the laser power density (Figure 6-2B).

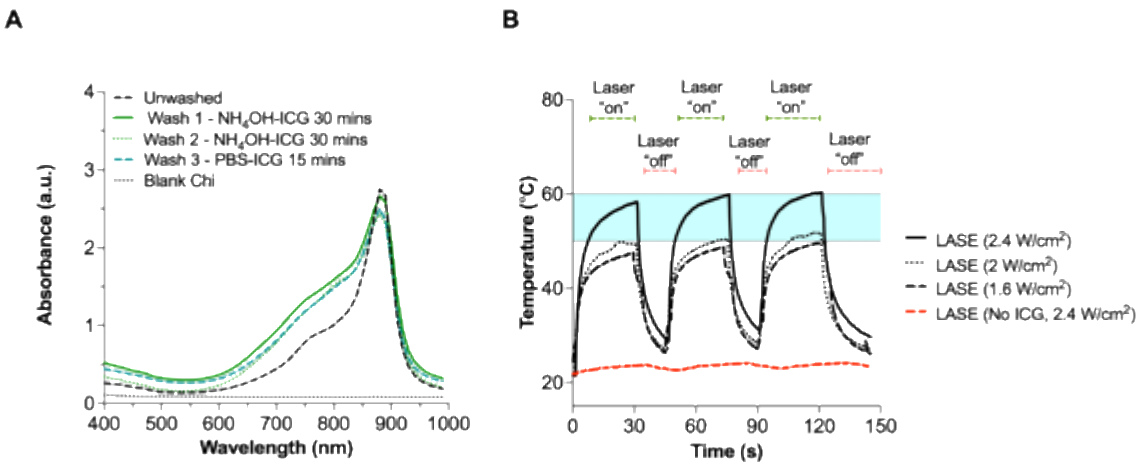

Figure 6-2. Absorbance spectra and photothermal response of LASE.
(A) Absorbance spectra of as-is prepared crosslinked LASE (LASE 4, black dashed line) and processed LASE 4 at different stages of neutralizing and washing. LASE (chitosan and no ICG dye) absorbance is shown using black dotted line. Data shown are mean of n = 2 independent LASE sections. (B) Photothermal response of LASE on *ex vivo* porcine small intestine irradiated using a continuous wave NIR laser tuned to 808 nm at varying laser power density from 1.6 W/cm^2 to 2.4 W/cm^2 in a 30 s "on" and 15 s "off" cycle (3 cycles total). Photothermal response of LASE (with no ICG dye added, red dashed line) to 2.4 W/cm^2 is indicated as baseline. The blue shaded region (50°C to 60°C) indicates the optimal temperature window for laser tissue sealing. Each photothermal response curve is a mean of n = 2 independent experiments.

The ability of LASE to close an intestinal wound was evaluated using modified ASTM F2458-05 test method on ex vivo porcine small intestine tissue (Figure 6-3A). Following sealing of incised incisions (timepoint 0 hours), both uncrosslinked LASE (56.29 ± 5.50 kPa) and crosslinked LASE (LASE 1-4, ranging from 55.82 – 93.86 kPa) following laser irradiation resulted in higher wound closure strength to the tissue compared to control Tachosil (13.24 ± 3.61 kPa). A trend was observed with higher crosslinking resulting in better adhesion and wound closure strength, but no significant differences were observed between the different crosslinked LASE (Figure 6-3B). Wound closure strength of sealed intestine sections was also evaluated at 6 hours and 24 hours following sealing. At 6 hours following laser sealing, crosslinked LASE 4 sealed tissue sections had the highest tensile strength (73.95 ± 13.61 kPa) compared to uncrosslinked (44.25 ± 10.2 kPa) and

other crosslinked LASE (40.01 – 67.19 psi). At 24 hours following sealing and incubation, a reduction in tensile strength of sealed intestine sections was observed compared to 0 hours and 6 hours timepoints. But, crosslinked LASE 4 had significantly higher adhesion (58.56 ± 16.08 kPa) to tissue at this timepoint compared to uncrosslinked LASE (10.38 ± 3.01 kPa) and crosslinked LASE 2 (10.0 ± 4.27 kPa) (Figure 6-3B). Tensile strength of intact intestine section (without wounding) was measured at each timepoint.

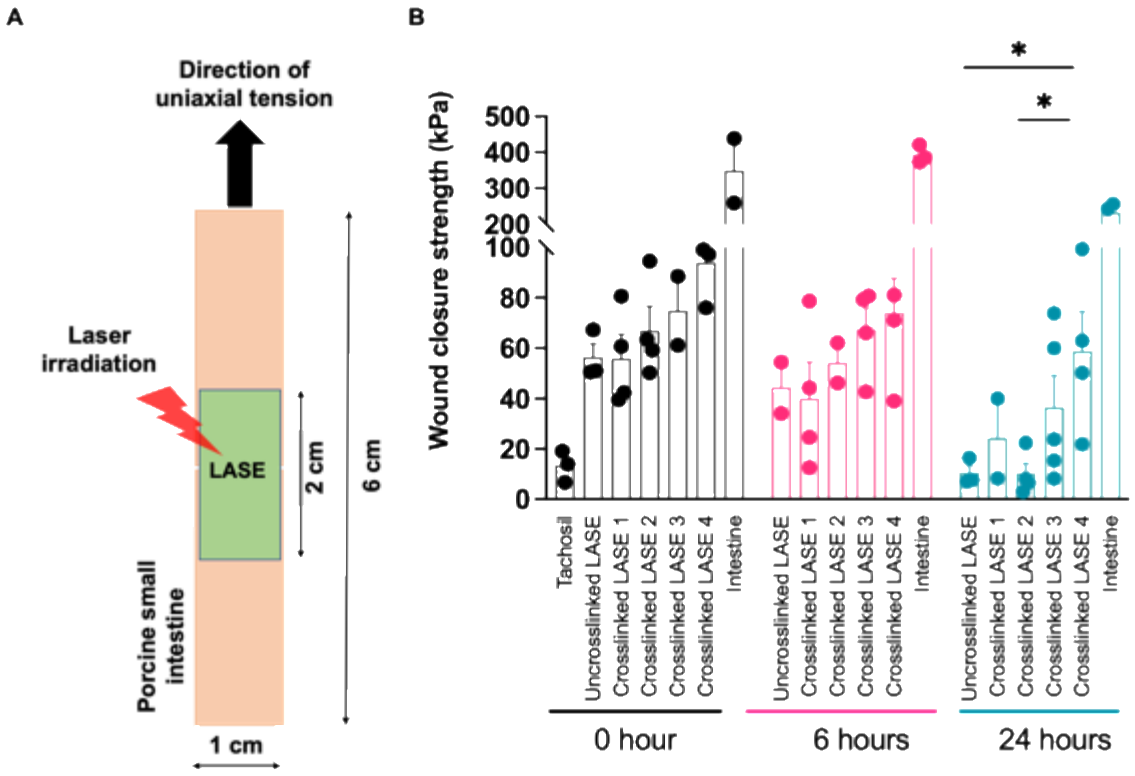

Figure 6-3. Adhesion of LASE to porcine intestine and wound closure strength.
(A) Schematic illustration of tissue dimensions and test set-up for wound closure strength studies according to modified ASTM F2458-05 test. (B) Wound closure strength (in kPa) of uncrosslinked and crosslinked LASE to the serosal surface of ex vivo porcine small intestine at pre-determined timepoints (0, 6, and 24 hours) following laser sealing. Data shown are mean ± standard error of the mean of n = 2 - 4 independent sealed intestine sections. Statistical significance was determined using two-way ANOVA followed by Fisher's LSD test and individual p-values are shown and p-value < 0.05, which was considered statistically significant.

Furthermore, we demonstrated the ability of LASE to seal and prevent luminal leakage using porcine small intestine tissue and measuring the leak pressure from the incision site using a in-house assembled leak pressure monitoring system (Figure 6-4A). A 1-cm full thickness cut was made thorough one wall of the lumen and closed either using sutures or LASE followed by injection of dyed water into the tubular small intestine and measuring leak pressure. The incised intestine (no suture or LASE application) showed leakage from the incision site as soon as dyed water was injected and a leak pressure of 11.78 ± 0.47 psi was recorded. Incised intestine section sutured with four Nylon 4-0 interrupted suture recorded a leak pressure of 19.53 ± 1.2 psi. Suture alone as a wound closure device could achieve ~78% leak pressure recovery compared to intact intestine (no incision, 24.98 ± 0.61 psi). Sealing of incised intestines with uncrosslinked LASE (19.78 ± 0.06 psi) and crosslinked LASE (20.78 – 22.03 psi) tolerated higher pressure compared to suture-closed intestines. Immediately following sealing (0-hour timepoint), crosslinked LASE 4 sealed intestines (22.03 ± 0.55 psi) achieved ~88% recovery of leak pressure compared to that of intact intestine.

Incised, sutured, LASE-sealed, and intact intestine sections were also incubated in a humid environment for 6 hours and subjected to leak pressure studies to evaluate the extended adhesion to the tissue. Incised and sutured intestine sections recorded leak pressure of 10.50 ± 0.49 psi and 17.10 ± 0.52 psi, respectively. Uncrosslinked LASE and crosslinked LASE maintained its adhesion to the tissue and were able to withstand significant pressure (19.37 – 20.91 psi) prior to leakage. Crosslinked LASE 4 which withstood the highest pressure at 0-hour timepoint, still maintained adhesion to tissue and achieved ~84% recovery of leak pressure compared to intact intestine leak pressure at this timepoint (24.84 ± 0.83 psi).

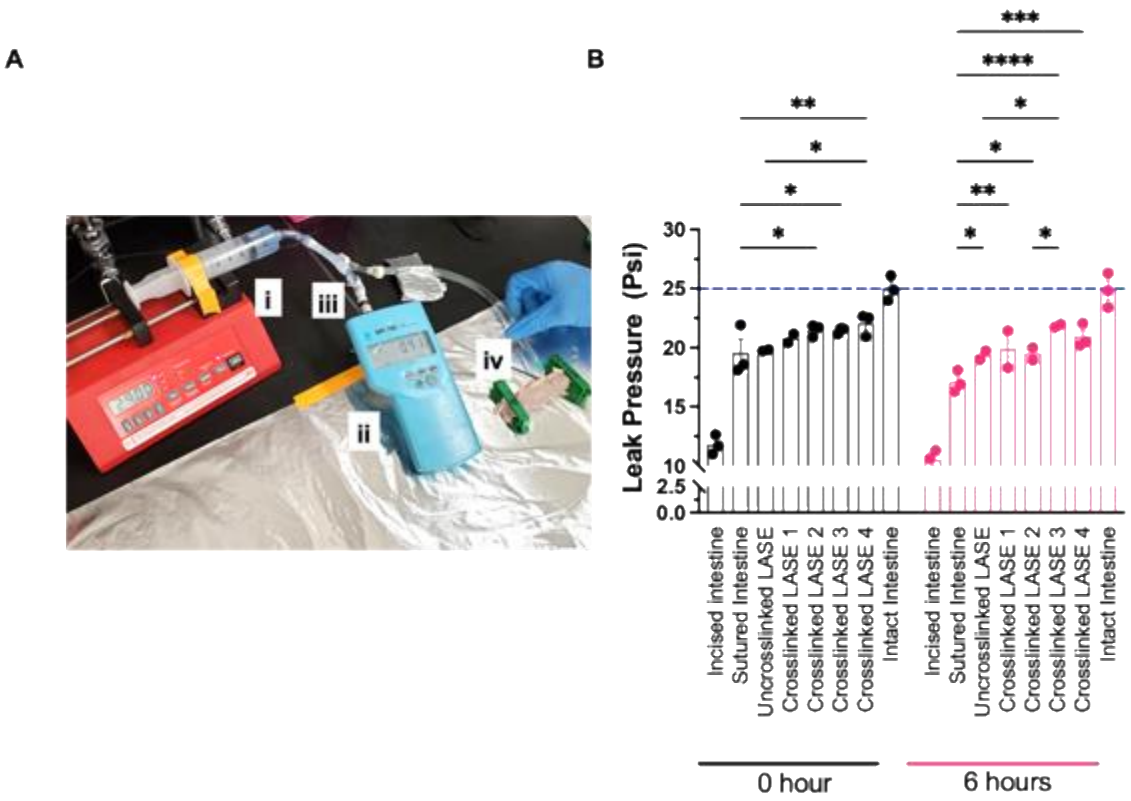

Figure 6- 4. Leak pressure setup and measurements.
(A) Schematic illustration of test set-up for leak pressure studies; (i) 60 mL connected to syringe pump for controlling the dyed water injection rate (ii) a digital pressure indicator for monitoring the leak pressure of test sealed intestines (iii) a Y-shaped connector for connecting the dyed water flow to the digital pressure indicator and the sealed intestine during measurements (iv) a 23G needle used for testing leak pressure of sealed intestine clamped on both ends. (B) Leak pressure (in psi) of incised intestine, sutured intestine, uncrosslinked and crosslinked LASE sealed intestine, and intact intestine at pre-determined timepoints (0 and 6 hours) following suturing or laser sealing. Data shown are mean ± standard error of the mean of n = 2 – 3 independent sealed intestine sections. Statistical significance was determined using two-way ANOVA followed by Fisher's LSD test and individual p-values are shown and p-value < 0.05, which was considered statistically significant.

Taken together the promising wound closure and leak pressure performance of uncrosslinked and crosslinked LASE in porcine small intestine tissue warrants the evaluation of LASE in repair of colorectal defects in an *in vivo* model.

We have also attempted to identify potential limitations of this LASE in its current form for colorectal repair or any other internal organ. The LASE in its current formulation is able to adhere to wet tissues but does not completely contour to the shape of tissue which can lead to potential gaps between the LASE-tissue interface in tortuous part of a tissue (example: bowel tissue). These tiny gaps could be failure points of LASE-tissue adhesion and can lead to sealant removal. LASE, like any other closure device (sutures or glues) could result in post-operative surgical adhesions in the abdomen area with secondary tissues and surface modifications of LASE with hydrophilic polymer or use of approved adhesion barrier (Seprafilm) will help mitigate the issue.

From our few *in vivo*/terminal trials so far, the following protocol was optimized for colorectal defect repair study in rats to evaluate the efficacy of suture-line reinforcement using LASE:

- The lower abdomen was shaved with an electric clipper and prepped using chlorhexidine gluconate and alcohol in series to the surgical site.
- A ~3-cm midline incision was made in the lower abdomen for accessing the colon. The ascending colon (1-cm above the cecum), the intestine tissue was removed from the abdomen and placed over moist gauze to create the defect.
- Prior to making an incisional defect, the area of the defect and surrounding tissue was gently abraded 10-15 times using an eye spear (#40400-8, PVA eye spear, BVI) until the intended area showed visible loss in luster. This can help transiently remove the serosal surface which can help with LASE-tissue adhesion following laser irradiation.
- A 0.5-cm incision was made in transverse direction and the defect was sutured using three interrupted knots of 7-0 Maxon green suture (polyglyconate suture, Medtronic, 18” CV-1 Taper, needle length 9mm, curvature 3/8, esutures.com *#6145-01*). Alternatively, 7-0 Vicryl suture (taper point needle) can also be used for suturing the defect.
- Closing the 0.5-cm defect with three interrupted knots will lead to a “leaky” defect closure to evaluate the efficacy of reinforcement of the suture line using LASE where closing the defect with five or six interrupted knots will be a “non-leaky” anastomosis closure. This

experimental model was developed to study colorectal anastomotic leakage(Komen et al., 2009).

- Note: Following suturing the defect, purge the defect area and the exposed intestine with ample 0.9% saline. Then the suture line and the immediate area was dried using a cotton swab prior to placing LASE over the intended area.
- A LASE section (~1cm * 0.75cm) was placed on the sutured transverse incision enough to cover the suture line and some area around the suture line. After placing the LASE and manually conforming it to the tissue, no additional saline purging was done over the LASE.
- The LASE-tissue was laser irradiated for 5 mins at ~230 mW for 5 mins. The temperature of the irradiated area was closely monitored making sure the temperature ranges between 55-60 °C. Also, the irradiated area was purged with saline at intermediate timepoints to keep the tissue moist and avoid any chances of desiccation.
- Following sealing and reinforcing the suture line with LASE, a section of Seprafilm (Baxter) cut to dimensions larger than the LASE (~1.5 cm * 1cm) will be applied over LASE to prevent/minimize intra-abdominal adhesion(Fazio et al., 2006). Note: the applied Seprafilm will be larger than the size of LASE.
- In case of terminal studies, the efficacy of reinforcement was evaluated by clamping around the defect area and performing leak test by infusing blue dyed water. Intestine defect closed alone with suture (leaky model) was also evaluated separately as control.
- In case of future survival studies, the abdominal incision will be closed using a layer of suture (for closing muscle layer) and then skin staples (for closing the skin layer). The rat will be recovered till pre-determined timepoints and parameters like intra-abdominal adhesion, leak pressure, etc. will be assessed.

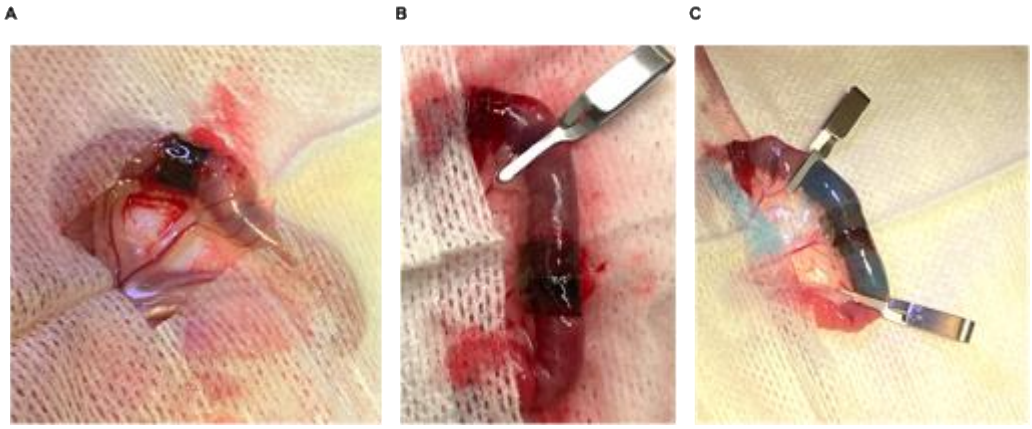

Figure 6-5. Fabrication and physical characterization of light-activated tissue-integrating sutures (LATIS).
Representative image of LASE placed over a 0.5-cm intestine incisional defect sutured using three interrupted knots of 7-0 Maxon suture. (B) Representative image of laser irradiated LASE and prior to leak study (C) Representative image of LASE reinforced sutured intestine holding pressure from infused blue-dyed water.

6.4 CONCLUSION

Anastomotic leakage is one of the most common complications following a colorectal surgery and requires the need for further re-intervention, prolonged hospitalization, and high mortality. In this study, we have developed a chitosan-based light-activated sealant (LASE) which can successfully adhere to wet tissue following laser irradiation of the LASE-tissue interface and can maintain its adhesion to the tissue for an extended period under wet tissue conditions. ICG dye present in the LASE facilitates the generation of photothermal response upon laser irradiation which helps achieve temperature required for adhesion of LASE to the wet tissue surface. Crosslinking of chitosan based LASE matrix with glutaraldehyde further helps in controlling the swelling behavior of this sealant under wet conditions thus reducing the chances of sealant failure. Compared with

sutures and Tachosil (fibrin coated collagen-based patch), LASE demonstrated strong and extended adhesion to tissues resulting in better wound closure strength over a 6 and 24-hour time period. LASE also helped in improved leak pressure tolerance compared to sutures both following sealing and 6-hour incubation which was almost equivalent to ~84% and 88% recovery, respectively compared to intact intestine. However, a further study in an *in vivo* model of colorectal defect will be needed to further assess the efficacy of LASE in sealing and preventing leakage/sealing failure over an extended period of 7 or 21-days. Detailed histological evaluation of sealant mediated inflammation at the defect site, quality of healed tissue at the defect site, and persistence of the sealant around the defect site will need to be examined to assess the suitability of LASE as an alternate closure device. Chitosan which is the primary constituent of the LASE matrix can further be functionalized to load bioactives (drugs, antibacterial agents, small molecules, etc.) which can aid in hemostasis, tissue repair processes, and prevention of any infection at the defect site which could negatively impact healing response. Overall, this “proof-of concept” study suggests that chitosan-based LASE could potentially be a versatile tissue sealant on its own or used in conjugation with sutures to reinforce suture lines for internal tissue repair application.

CHAPTER 7: CONCLUSIONS AND FUTURE PERSECTIVES

7.1 SUMMARY AND INTERPRETATION OF FINDINGS

The efficacy of silk fibroin-based light activated sealants (LASE) has demonstrated improved healing outcomes in sealing murine skin incisional wounds compared to conventional stores and skin glue(Urie, Guo, et al., 2018b). Besides improved biomechanical strength recovery of skin in early stages of healing, LASE loaded with vancomycin and used for closing skin incisions were less susceptible to MRSA infection in a murine model of surgical site infection compared to antibacterial sutures(Urie et al., 2021). This dissertation work focused on further using of LASE for management of incisional and excisional wounds.

The results of Chapter 2 investigate further into use of silk-fibroin based LASE as an alternative incisional wound closure device. The healing outcome of using LASE at intermediate timepoints on day 2, 4, and 7 post-wounding was evaluated in a murine model of dorsal incisional wounds. Intermediate timepoint show that LASE-mediated skin closure resulted in better skin barrier function measured by transepidermal water loss and earlier recovery of recovery of healed skin strength. Further, delivery of a bioactive (histamine) along with LASE improved biomechanical recovery but no effect on barrier function recovery was observed. The persistence of LASE in the wound bed was visualized using fluorescent imaging (LiCor Pearl Impulse) and photoacoustic imaging (Vevo 3100 + LAZR-X, VisualSonics in collaboration with Prof. Russell S. Witte's lab at University of Arizona) during the course of healing. These intermediate timepoint observations were further corroborated with histological and immunohistological staining for epidermal gap, scar area, and immune cell activity.

The results of Chapter 3 and 4 discussed the fabrication of light-activated tissue-integrating sutures (LATIS) which synergizes the benefit of conventional suturing and light-activated sealing intended for closure of incisional wounds. LATIS have demonstrated higher tissue integration post

laser irradiation of suture line compared to commercial control sutures resulting in higher biomechanical skin strength recovery at day 3 post-wounding in murine dorsal skin incision model. The second generation LATIS was loaded with copper ions during the fabrication process. Copper ion can act as an effective chromophore resulting in robust photothermal response and as a bioactive can positively impact the healing process(Borkow et al., 2010; Sen et al., 2002). Burst release of copper ion was observed from LATIS which enhanced healing outcomes by improved healed skin biomechanical property and neovascularization at the wound site. These results indicate that copper-eluting fibers have a role in enhancing wound healing and tissue repair.

The results of Chapter 5 evaluate the use of silk fibroin-based LASE to be used a wound dressing along with bioactives for full-thickness excisional wound repair in murine model of splinted wounds. Delivery of a bioactive (histamine) along with control and LASE dressing improved wound healing kinetics and biomechanical strength also. Further histological evaluating at intermediate timepoints. We also demonstrated delivery of a second therapeutic in a temporal fashion further improved the wound healing outcomes in both acute and diabetic wounds. This is significant, as it may help time the delivery of therapeutic to modulate individual stages of wound healing and minimize need for multiple dosing of therapeutics. Fundamental understanding of tissue repair kinetics and associated temporal delivery of therapeutics can lead to faster healing and improved tissue repair outcomes, thus reducing the propensity for re-opening, progression to intractable phenotypes and surgical site infections, all of which can have remarkable outcomes in the clinic.

7.2 FUTURE PERSPECTIVES

This work establishes a relationship between cation flux, kinase activation and oxidative signaling upstream of the NLRP3 inflammasome. However, there are a number of compelling open questions that warrant further study:

1. **Tracking healing process *in vivo* following skin closure using LASE.** While this work identifies healing outcomes at intermediate timepoints (day 2, 4, and

7 post-wounding) by evaluating TEWL levels at the healing site, biomechanical strength recovery of healed skin, histological evaluation of healed skin, and ultrasound/photoacoustic imaging (US/PAI) of the healing tissue-LASE interface. In this study we have optimized methods for imaging murine skin wound section using US/PAI methods and obtained healing information at intermediate timepoints. The US/PAI results are from different mice at each timepoint due to the nature of the study (*in vivo*/terminal for individual timepoints) and imaging of excised healed skin samples, an *in vivo* study with real-time imaging of the same healing wound during the course of the study will be beneficial. Besides looking at LASE persistence in the incision site from PAI signal, real time PAI signal from wounds can help obtain additional information; neoangiogenesis in the healing region(Ogunlade et al., 2019; Sun et al., 2018), hemoglobin oxygen saturation (Frueh et al., 2018; Petri et al., 2016) which are crucial parameters to monitor progression of healing.

2. **Effect of combining resolvins with LASE for tissue repair.** Efficacy of incisional wound repair using LASE and combining LASE with histamine (a bioactive which modulates early-stage healing processes) have been demonstrated in our studies. However, delivery of resolvins (RvD2, Resolvin D2) as a pro-resolving and an anti-inflammatory bioactive along with LASE for incisional wound healing can be a strategy to improve healing outcomes. RvD2 has been previously reported to be beneficial for skin wound healing by accelerating reepithelialization, improving blood flow, and collagen deposition which are conducive for improved healing(Hellmann et al., 2018; Menon et al., 2017).

3. **Probe specific histamine receptors to elucidate role of histamine in improving healing outcomes in wounds.** The effect of histamine on collagen deposition, keratinocyte migration, and fibroblast proliferation has been reported using Histamine H1 and H2 receptor(Dabrowski & Maśliński, 1981; Kupietzky & Levi-Schaffer, 1996; Masliíski & Olczak, 1977). A broad screen of specific histamine receptor agonists and antagonists that acts on its four receptors; H1R – H4R will be helpful to delineate specific receptors and downstream pathways involved in elucidating the effect of histamine of EMT, immune cell activity, and overall wound healing outcomes.

4. **Reinforcement of suture line in colorectal defect repair with crosslinked chitosan based LASE.** Based on our pilot *in vivo*/terminal trials, we observed eversion of incised edges of small intestine in rats. Our as-is prepared crosslinked chitosan based LASE was able to achieve good adhesion to the intestine tissue following laser sealing procedure but this was not enough to incised tissue edge approximated due to inherent eversion of the underlying tissue. Hence from the next in vivo trials a leakage model; a 5-mm (or longer incision) mechanically held together by 3-simple interrupted knots of 7-0 Vicryl suture will be a useful model in this study. Reinforcing the sub-optimal suture line/leakage model using LASE will help evaluate the efficacy of anastomotic leak prevention using LASE(Slieker et al., 2013).

REFRENCES

Akita, S., Akino, K., & Hirano, A. (2013). Basic fibroblast growth factor in scarless wound healing. *Advances in wound care*, *2*(2), 44-49.

Al-Mubarak, L., & Al-Haddab, M. (2013). Cutaneous wound closure materials: An overview and update. *Journal of Cutaneous and Aesthetic Surgery*, *6*(4), 178-188. https://doi.org/10.4103/0974-2077.123395

Alemdaroğlu, C., Değim, Z., Çelebi, N., Zor, F., Öztürk, S., & Erdoğan, D. (2006). An investigation on burn wound healing in rats with chitosan gel formulation containing epidermal growth factor. *Burns*, *32*(3), 319-327.

Ali, M. R. K., Snyder, B., & El-Sayed, M. A. (2012). Synthesis and optical properties of small Au nanorods using a seedless growth technique. *Langmuir : the ACS journal of surfaces and colloids*, *28*(25), 9807. https://doi.org/10.1021/la301387p

Alvarez-López, C., & Aguirre-Soto, A. (2021). A review on the use of light-initiated crosslinking at biomacromolecular interfaces with Rose Bengal for “Nanosuturing”. *Materials Today: Proceedings*.

Anthis, A. H., Hu, X., Matter, M. T., Neuer, A. L., Wei, K., Schlegel, A. A., . . . Herrmann, I. K. (2021). Chemically Stable, Strongly Adhesive Sealant Patch for Intestinal Anastomotic Leakage Prevention. *Advanced Functional Materials*, *31*(16), 2007099.

Ark, M., Cosman, P. H., Boughton, P., & Dunstan, C. R. (2016). photochemical tissue bonding (PTB) methods for sutureless tissue adhesion. *International Journal of Adhesion and Adhesives*, *71*, 87-98.

Artuc, M., Hermes, B., Stckelings, U., Grützkau, A., & Henz, B. (1999). Mast cells and their mediators in cutaneous wound healing–active participants or innocent bystanders? *Experimental dermatology*, *8*(1), 1-16.

Bairy, K., Rao, C., Ramesh, K., & Kulkarni, D. (1991). Effects of antihistamines on wound healing. *Indian journal of experimental biology*, *29*(4), 398-399.

Bakker, I., Morks, A., Ten Cate Hoedemaker, H., Burgerhof, J., Leuvenink, H., Van Praagh, J., . . . Group, C. C.-s. S. (2017). Randomized clinical trial of biodegradeable intraluminal sheath to prevent anastomotic leak after stapled colorectal anastomosis. *Journal of British Surgery*, *104*(8), 1010-1019.

Barrientos, S., Stojadinovic, O., Golinko, M. S., Brem, H., & Tomic-Canic, M. (2008). Growth factors and cytokines in wound healing. *Wound repair and regeneration*, *16*(5), 585-601.

Batlle, E., Sancho, E., Francí, C., Domínguez, D., Monfar, M., Baulida, J., & De Herreros, A. G. (2000). The transcription factor snail is a repressor of E-cadherin gene expression in epithelial tumour cells. *Nature cell biology*, *2*(2), 84-89.

Begnaud, S., Chen, T., Delacour, D., Mège, R.-M., & Ladoux, B. (2016). Mechanics of epithelial tissues during gap closure. *Current opinion in cell biology*, *42*, 52-62.

Beldon, P. (2010). Basic science of wound healing. *Surgery (Oxford)*, *28*(9), 409-412.

Bellare, A., Epperly, M. W., Greenberger, J. S., Fisher, R., & Glowacki, J. (2018). Development of tensile strength methodology for murine skin wound healing. *MethodsX*, *5*, 337-344.

Berk, W., Osbourne, D., & Taylor, D. (1988). Evaluation of the 'golden period'for wound repair: 204 cases from a Third World emergency department. *Annals of emergency medicine*, *17*(5), 496-500.

Borkow, G., Gabbay, J., Dardik, R., Eidelman, A. I., Lavie, Y., Grunfeld, Y., . . . Marikovsky, M. (2010). Molecular mechanisms of enhanced wound healing by copper oxide-impregnated dressings. *Wound repair and regeneration*, *18*(2), 266-275.

Borkow, G., Gabbay, J., & Zatcoff, R. C. (2008). Could chronic wounds not heal due to too low local copper levels? *Medical hypotheses*, *70*(3), 610-613.

Boyd, J., & Smith, A. (1959). The effect of histamine and a histamine-releasing agent (compound 48/80) on wound healing. *The Journal of pathology and bacteriology*, *78*(2), 379-388.

Bruns, T. B., Simon, H. K., McLario, D. J., Sullivan, K. M., Wood, R. J., & Anand, K. (1996). Laceration repair using a tissue adhesive in a children's emergency department. *Pediatrics*, *98*(4), 673-675.

Bré, L. P., Zheng, Y., Pêgo, A. P., & Wang, W. (2013). Taking tissue adhesives to the future: from traditional synthetic to new biomimetic approaches. *Biomaterials Science*, *1*(3), 239-253.

Campbell, J., & Marks, A. (1985). Suture materials and suturing techniques. *In practice*, *7*(3), 72-75.

Catanzano, O., Acierno, S., Russo, P., Cervasio, M., De Caro, M. D. B., Bolognese, A., . . . Calignano, A. (2014). Melt-spun bioactive sutures containing nanohybrids for local delivery of anti-inflammatory drugs. *Materials Science and Engineering: C*, *43*, 300-309.

Celeste, C., & Stashak, T. S. (2008). *Selection of Suture Materials, Suture Patterns and Drains for Wound Closure: Equine Wound Management*. Wiley-Blackwell Publisher: Iowa.

Champeau, M., Thomassin, J.-M., Tassaing, T., & Jérôme, C. (2017). Current manufacturing processes of drug-eluting sutures. *Expert opinion on drug delivery*, *14*(11), 1293-1303.

Chang, W., Liu, F., Sharif, H. R., Huang, Z., Goff, H. D., & Zhong, F. (2019). Preparation of chitosan films by neutralization for improving their preservation effects on chilled meat. *Food Hydrocolloids*, *90*, 50-61.

Constantinescu, M., Alfieri, A., Mihalache, G., Stuker, F., Ducray, A., Seiler, R., . . . Reinert, M. (2007). Effect of laser soldering irradiation on covalent bonds of pure collagen. *Lasers in Medical Science*, *22*(1), 10-14. https://doi.org/10.1007/s10103-006-0411-0

Costales, A. B., Patil, D., Mulya, A., Kirwan, J. P., & Michener, C. M. (2018). 2-Octylcyanoacrylate for the prevention of anastomotic leak. *Journal of Surgical Research*, *226*, 166-172.

Creighton, J. A., & Eadon, D. G. (1991). Ultraviolet–visible absorption spectra of the colloidal metallic elements. *Journal of the Chemical Society, Faraday Transactions*, *87*(24), 3881-3891.

Currie, L. J., Sharpe, J. R., & Martin, R. (2001). The use of fibrin glue in skin grafts and tissue-engineered skin replacements. *Plast Reconstr Surg*, *108*, 1713-1726.

Dabrowski, R., & Maśliński, C. (1981). The role of histamine in wound healing. II. The effect of antagonists and agonists of histamine receptors (H 1 and H 2) on collagen levels in granulation tissue. *Agents and actions*, *11*(1), 122-124.

Dabrowski, R., Maśliński, C., & Górski, P. (1975). The effects of histamine liberators and exogenous histamine on wound healing in rat. *Agents and actions*, *5*(4), 311-314.

De Hous, N., Lefevre, J., D'Urso, A., Van den Broeck, S., & Komen, N. (2020). Intraluminal bypass devices as an alternative to protective ostomy for prevention of colorectal anastomotic leakage: a systematic review of the literature. *Colorectal Disease*, *22*(11), 1496-1505.

Dini, V., Barbanera, S., & Romanelli, M. (2014). Quantitative evaluation of maceration in venous leg ulcers by transepidermal water loss (TEWL) measurement. *The international journal of lower extremity wounds*, *13*(2), 116-119.

Dong, R. H., Qin, C. C., Qiu, X., Yan, X., Yu, M., Cui, L., . . . Long, Y. Z. (2015). In situ precision electrospinning as an effective delivery technique for cyanoacrylate medical glue with high efficiency and low toxicity. *Nanoscale*, *7*(46), 19468-19475. https://doi.org/10.1039/c5nr05786h

Dubas, S. T., Wacharanad, S., & Potiyaraj, P. (2011). Tunning of the antimicrobial activity of surgical sutures coated with silver nanoparticles. *Colloids and Surfaces A: Physicochemical and Engineering Aspects*, *380*(1-3), 25-28.

Dunn, D. L., & Phillips, J. (2007). Wound closure manual. In. Ethicon.

Eming, S. A., Martin, P., & Tomic-Canic, M. (2014). Wound repair and regeneration: mechanisms, signaling, and translation. *Science translational medicine*, *6*(265), 265sr266-265sr266.

Esposito, G., Rossi, F., Matteini, P., Scerrati, A., Puca, A., Albanese, A., . . . Pini, R. (2013). In vivo laser assisted microvascular repair and end-to-end anastomosis by means of indocyanine green-infused chitosan patches: A pilot study. *Lasers in Surgery and Medicine*, *45*(5), 318-325. https://doi.org/10.1002/lsm.22145

Farokhi, M., Mottaghitalab, F., Fatahi, Y., Khademhosseini, A., & Kaplan, D. L. (2018). Overview of silk fibroin use in wound dressings. *Trends in biotechnology*, *36*(9), 907-922.

Fazio, V. W., Cohen, Z., Fleshman, J. W., Van Goor, H., Bauer, J. J., Wolff, B. G., . . . Becker, J. M. (2006). Reduction in adhesive small-bowel obstruction by Seprafilm® adhesion barrier after intestinal resection. *Diseases of the Colon & rectum*, *49*(1), 1-11.

Fernandes, M. G., da Silva, L. P., & Marques, A. P. (2019). Skin mechanobiology and biomechanics: from homeostasis to wound healing. *Advances in Biomechanics and Tissue Regeneration*, 343-360.

Fluhr, J. W., Feingold, K. R., & Elias, P. M. (2006). Transepidermal water loss reflects permeability barrier status: validation in human and rodent in vivo and ex vivo models. *Experimental dermatology*, *15*(7), 483-492.

Forbrich, A., Heinmiller, A., & Zemp, R. J. (2017). Photoacoustic imaging of lymphatic pumping. *Journal of biomedical optics*, *22*(10), 106003.

Fragonas, E., Valente, M., Pozzi-Mucelli, M., Toffanin, R., Rizzo, R., Silvestri, F., & Vittur, F. (2000). Articular cartilage repair in rabbits by using suspensions of allogenic chondrocytes in alginate. *Biomaterials*, *21*(8), 795-801.

Frick, J. M., Ambrosi, A., Pollo, L. D., & Tessaro, I. C. (2018). Influence of glutaraldehyde crosslinking and alkaline post-treatment on the properties of chitosan-based films. *Journal of Polymers and the Environment*, *26*(7), 2748-2757.

Frueh, F. S., Später, T., Körbel, C., Scheuer, C., Simson, A. C., Lindenblatt, N., . . . Laschke, M. W. (2018). Prevascularization of dermal substitutes with adipose tissue-derived microvascular fragments enhances early skin grafting. *Scientific reports*, *8*(1), 1-9.

Fujie, T., Kinoshita, M., Shono, S., Saito, A., Okamura, Y., Saitoh, D., & Takeoka, S. (2010). Sealing effect of a polysaccharide nanosheet for murine cecal puncture. *Surgery*, *148*(1), 48-58.

Gal, P., Kilik, R., Mokry, M., Vidinsky, B., Vasilenko, T., Mozes, S., . . . Lenhardt, L. (2008). Simple method of open skin wound healing model in corticosteroid-treated and diabetic rats: standardization of semi-quantitative and quantitative histological assessments. *Vet. Med.*, *53*(12), 652-659. https://doi.org/10.17221/1973-VETMED

Galiano, R. D., Michaels, V., Joseph, Dobryansky, M., Levine, J. P., & Gurtner, G. C. (2004). Quantitative and reproducible murine model of excisional wound healing. *Wound repair and regeneration*, *12*(4), 485-492.

Gallo, A. L., Paladini, F., Romano, A., Verri, T., Quattrini, A., Sannino, A., & Pollini, M. (2016). Efficacy of silver coated surgical sutures on bacterial contamination, cellular response and wound healing. *Materials Science and Engineering: C*, *69*, 884-893.

Gatt, D., Quick, C., & Owen-Smith, M. (1985). Staples for wound closure: a controlled trial. *Annals of the Royal College of Surgeons of England*, *67*(5), 318.

George, T., & Simpson, D. (1985). Skin wound closure with staples in the accident and emergency department. *Journal of the Royal College of Surgeons of Edinburgh*, *30*(1), 54-56.

Georgiev-Hristov, T., García-Arranz, M., García-Gómez, I., García-Cabezas, M. A., Trébol, J., Vega-Clemente, L., . . . García-Olmo, D. (2012). Sutures enriched with adipose-derived stem cells decrease the local acute inflammation after tracheal anastomosis in a murine model. *European Journal of Cardio-Thoracic Surgery*, *42*(3), e40-e47.

Ghidoni, I., Chlapanidas, T., Bucco, M., Crovato, F., Marazzi, M., Vigo, D., . . . Faustini, M. (2008). Alginate cell encapsulation: new advances in reproduction and cartilage regenerative medicine. *Cytotechnology*, *58*(1), 49-56.

Ghosh, D., Urie, R., Chang, A., Nitiyanandan, R., Lee, J. K., Kilbourne, J., & Rege, K. (2019). Light-Activated Tissue-Integrating Sutures as Surgical Nanodevices. *Advanced healthcare materials*, 1900084.

Gibble, J., & Ness, P. (1990). Fibrin glue: the perfect operative sealant? *Transfusion*, *30*(8), 741-747.

Gorter, R. W., Butorac, M., & Cobian, E. P. (2004). Examination of the cutaneous absorption of copper after the use of copper-containing ointments. *American journal of therapeutics*, *11*(6), 453-458.

Grace, M., Chand, N., & Bajpai, S. K. (2009). Copper alginate-cotton cellulose (CACC) fibers with excellent antibacterial properties. *Journal of Engineered Fibers and Fabrics*, *4*(3), 155892500900400303.

Grada, A., Mervis, J., & Falanga, V. (2018). Research techniques made simple: animal models of wound healing. *Journal of Investigative Dermatology*, *138*(10), 2095-2105. e2091.

Greenberg, J. A., & Clark, R. M. (2009). Advances in suture material for obstetric and gynecologic surgery. *Reviews in obstetrics & gynecology*, *2*(3), 146.

Grimes, P. E., & Hunt, S. G. (1993). Considerations for cosmetic surgery in the black population. *Clinics in plastic surgery*, *20*(1), 27-34.

Gurtner, G. C., Dauskardt, R. H., Wong, V. W., Bhatt, K. A., Wu, K., Vial, I. N., . . . Longaker, M. T. (2011). Improving cutaneous scar formation by controlling the mechanical environment: large animal and phase I studies. *Annals of surgery*, *254*(2), 217-225.

Habermehl, J., Skopinska, J., Boccafoschi, F., Sionkowska, A., Kaczmarek, H., Laroche, G., & Mantovani, D. (2005). Preparation of Ready-to-use, Stockable and Reconstituted Collagen. *Macromolecular Bioscience*, *5*(9), 821-828. https://doi.org/10.1002/mabi.200500102

Haensel, D., & Dai, X. (2018). Epithelial-to-mesenchymal transition in cutaneous wound healing: Where we are and where we are heading. *Developmental dynamics*, *247*(3), 473-480.

Hall, M. J., Schwartzman, A., Zhang, J., & Liu, X. (2017). Ambulatory surgery data from hospitals and ambulatory surgery centers: United States, 2010. *National health statistics reports*(102), 1-15.

Hammond, J., Lim, S., Wan, Y., Gao, X., & Patkar, A. (2014). The burden of gastrointestinal anastomotic leaks: an evaluation of clinical and economic outcomes. *Journal of Gastrointestinal Surgery*, *18*(6), 1176-1185.

Harvey, C., & Logan, C. H. (1986). A prospective trial of skin staples and sutures in skin closure. *Irish journal of medical science*, *155*(6), 194-196.

Hatamochi, A., Ueki, H., Mauch, C., & Krieg, T. (1991). Effect of histamine on collagen and collagen m-RNA production in human skin fibroblasts. *Journal of dermatological science*, *2*(6), 407-412.

Hellmann, J., Sansbury, B. E., Wong, B., Li, X., Singh, M., Nuutila, K., . . . Spite, M. (2018). Biosynthesis of D-series resolvins in skin provides insights into their role in tissue repair. *Journal of Investigative Dermatology*, *138*(9), 2051-2060.

Hinz, B., Celetta, G., Tomasek, J. J., Gabbiani, G., & Chaponnier, C. (2001). Alpha-smooth muscle actin expression upregulates fibroblast contractile activity. *Molecular biology of the cell*, *12*(9), 2730-2741.

Hoeppner, J., Wassmuth, B., Marjanovic, G., Timme, S., Hopt, U. T., & Keck, T. (2010). Anastomotic sealing by extracellular matrices (ECM) improves healing of colonic anastomoses in the critical early phase. *Journal of Gastrointestinal Surgery*, *14*(6), 977-986.

Hoffman, G. T., States), R.-H. I. o. T. U., Byrd, B. D., States), R.-H. I. o. T. U., Soller, E. C., States), R.-H. I. o. T. U., . . . States), R.-H. I. o. T. U. (2003). Alternative chromophores for use in light-activated surgical adhesives: optimization of parameters for tensile strength and thermal damage profile. Lasers in Surgery: Advanced Characterization, Therapeutics, and Systems XIII,

Hostynek, J. J., & Maibach, H. I. (2006). Copper Hypersensitivity: Dermatologic Aspects—Overview. *Copper and the Skin*, 115.

Hu, J., Song, Y., Zhang, C., Huang, W., Chen, A., He, H., . . . Liu, J. (2020). Highly Aligned Electrospun Collagen/PCL Surgical Sutures with Sustained Release of Growth Factors for Wound Regeneration. *ACS Applied Bio Materials*.

Huang, H.-C., Barua, S., Kay, D. B., & Rege, K. (2009). Simultaneous enhancement of photothermal stability and gene delivery efficacy of gold nanorods using polyelectrolytes. *Acs Nano*, *3*(10), 2941-2952.

Huang, H.-C., Barua, S., Sharma, G., Dey, S. K., & Rege, K. (2011). Inorganic nanoparticles for cancer imaging and therapy. *Journal of controlled Release*, *155*(3), 344-357.

Huang, H.-C., Walker, C. R., Nanda, A., & Rege, K. (2013). Laser welding of ruptured intestinal tissue using plasmonic polypeptide nanocomposite solders. *ACS nano*, *7*(4), 2988. https://doi.org/10.1021/nn303202k

Hudson, L. G., Newkirk, K. M., Chandler, H. L., Choi, C., Fossey, S. L., Parent, A. E., & Kusewitt, D. F. (2009). Cutaneous wound reepithelialization is compromised in mice lacking functional Slug (Snai2). *Journal of dermatological science*, *56*(1), 19-26.

Hussey, M., & Bagg, M. (2011). Principles of Wound Closure. *Operative Techniques in Sports Medicine*, *19*(4), 206-211. https://doi.org/10.1053/j.otsm.2011.10.004

Jain, K., & Gorisch, W. (1979). Repair of small blood vessels with the neodymium-YAG laser: a preliminary report. *Surgery*, *85*(6), 684-688.

Jeon, E. Y., Hwang, B. H., Yang, Y. J., Kim, B. J., Choi, B.-H., Jung, G. Y., & Cha, H. J. (2015). Rapidly light-activated surgical protein glue inspired by mussel adhesion and insect structural crosslinking. *Biomaterials*, *67*, 11-19. https://doi.org/10.1016/j.biomaterials.2015.07.014

Johal, H., & Kreder, H. (2018). Cochrane in CORR®: Negative Pressure Wound Therapy for Skin Grafts and Surgical Wounds Healing by Primary Intention. *Clinical orthopaedics and related research*, *476*(3), 463.

Johnson, K. E., & Wilgus, T. A. (2014). Vascular endothelial growth factor and angiogenesis in the regulation of cutaneous wound repair. *Advances in wound care*, *3*(10), 647-661.

Joseph, B., George, A., Gopi, S., Kalarikkal, N., & Thomas, S. (2017). Polymer sutures for simultaneous wound healing and drug delivery – A review. *International Journal of Pharmaceutics*, *524*(1-2), 454-466. https://doi.org/10.1016/j.ijpharm.2017.03.041

Justinger, C., Moussavian, M. R., Schlueter, C., Kopp, B., Kollmar, O., & Schilling, M. K. (2009). Antibiotic coating of abdominal closure sutures and wound infection. *Surgery*, *145*(3), 330-334.

Kashiwabuchi, F., Parikh, K. S., Omiadze, R., Zhang, S., Luo, L., Patel, H. V., . . . Hanes, J. (2017). Development of absorbable, antibiotic-eluting sutures for ophthalmic surgery. *Translational vision science & technology*, *6*(1), 1-1.

Kato, Y. P., Christiansen, D. L., Hahn, R. A., Shieh, S.-J., Goldstein, J. D., & Silver, F. H. (1989). Mechanical properties of collagen fibres: a comparison of reconstituted and rat tail tendon fibres. *Biomaterials*, *10*(1), 38-42. https://doi.org/10.1016/0142-9612(89)90007-0

Khatri, K. A., Mahoney, D. L., & McCartney, M. J. (2011). Laser scar revision: A review. In (Vol. 13, pp. 54-62): Taylor & Francis.

Kim, K. Y., Anoushiravani, A. A., Long, W. J., Vigdorchik, J. M., Fernandez-Madrid, I., & Schwarzkopf, R. (2017). A meta-analysis and systematic review evaluating skin closure after total knee arthroplasty—What is the best method? *The Journal of arthroplasty*, *32*(9), 2920-2927.

Kim, S. H., Lee, Y. J., Chao, J. R., Sultan, M. T., Lee, H. J., Lee, J. M., . . . Lee, H. (2020). Rapidly photocurable silk fibroin sealant for clinical applications. *NPG Asia Materials*, *12*(1), 1-16.

Komen, N., van der Wal, H.-C., Ditzel, M., Kleinrensink, G.-J., Jeekel, H., & Lange, J. F. (2009). Colorectal anastomotic leakage: a new experimental model. *Journal of Surgical Research*, *155*(1), 7-12.

Komi, D. E. A., Rambasek, T., & Wöhrl, S. (2018). Mastocytosis: from a molecular point of view. *Clinical reviews in allergy & immunology*, *54*(3), 397-411.

Kupietzky, A., & Levi-Schaffer, F. (1996). The role of mast cell-derived histamine in the closure of an in vitro wound. *Inflammation research*, *45*(4), 176-180.

Kuwahara, M., Hatoko, M., Tada, H., & Tanaka, A. (2001). E-cadherin expression in wound healing of mouse skin. *Journal of cutaneous pathology*, *28*(4), 191-199.

Larouche, J., Sheoran, S., Maruyama, K., & Martino, M. M. (2018). Immune regulation of skin wound healing: mechanisms and novel therapeutic targets. *Advances in wound care*, *7*(7), 209-231.

Lauto, A., Stoodley, M., Barton, M., Morley, J. W., Mahns, D. A., Longo, L., & Mawad, D. (2012). Fabrication and application of rose bengal-chitosan films in laser tissue repair. *JoVE (Journal of Visualized Experiments)*(68), e4158.

Lee, K. Y., & Mooney, D. J. (2012). Alginate: properties and biomedical applications. *Progress in polymer science*, *37*(1), 106-126.

Li, C., Huang, J., Wang, K., Liu, Q., & Chen, Z. (2020). Investigation on thermal damage model of skin tissue in vitro by infrared laser welding. *Optics and Lasers in Engineering*, *124*, 105807.

Li, C., & Wang, K. (2021). Effect of welding temperature and protein denaturation on strength of laser biological tissues welding. *Optics & Laser Technology*, *138*, 106862.

Li, J., Zhai, D., Lv, F., Yu, Q., Ma, H., Yin, J., . . . Wu, C. (2016). Preparation of copper-containing bioactive glass/eggshell membrane nanocomposites for improving angiogenesis, antibacterial activity and wound healing. *Acta biomaterialia*, *36*, 254-266.

Li, M., Liu, X., Tan, L., Cui, Z., Yang, X., Li, Z., . . . Wu, S. (2018). Noninvasive rapid bacteria-killing and acceleration of wound healing through photothermal/photodynamic/copper ion synergistic action of a hybrid hydrogel. *Biomaterials science*, *6*(8), 2110-2121.

Lin, J.-C., Tsai, J.-T., Chao, T.-Y., Ma, H.-I., & Liu, W.-H. (2018). The STAT3/Slug axis enhances radiation-induced tumor invasion and cancer stem-like properties in radioresistant glioblastoma. *Cancers*, *10*(12), 512.

Lin, M., Wang, D., Liu, S., Huang, T., Sun, B., Cui, Y., . . . Sun, H. (2015). Cupreous complex-loaded chitosan nanoparticles for photothermal therapy and chemotherapy of oral epithelial carcinoma. *ACS applied materials & interfaces*, *7*(37), 20801-20812.

Liu, Y., Cai, Z., Sheng, L., Ma, M., Xu, Q., & Jin, Y. (2019). Structure-property of crosslinked chitosan/silica composite films modified by genipin and glutaraldehyde under alkaline conditions. *Carbohydrate polymers*, *215*, 348-357.

Lu, M., Liu, Y., Huang, Y.-C., Huang, C.-J., & Tsai, W.-B. (2018). Fabrication of photo-crosslinkable glycol chitosan hydrogel as a tissue adhesive. *Carbohydrate polymers*, *181*, 668-674.

Ma, Y., Yabluchanskiy, A., Iyer, R. P., Cannon, P. L., Flynn, E. R., Jung, M., . . . Lindsey, M. L. (2016). Temporal neutrophil polarization following myocardial infarction. *Cardiovascular research*, *110*(1), 51-61.

Mackey, M. A., Ali, M. R. K., Austin, L. A., Near, R. D., & El-Sayed, M. A. (2014). The most effective gold nanorod size for plasmonic photothermal therapy: theory and in vitro experiments.(Report). *Journal of Physical Chemistry B*, *118*(5), 1319-1326. https://doi.org/10.1021/jp409298f

Makino, T., Jinnin, M., Muchemwa, F., Fukushima, S., Kogushi-Nishi, H., Moriya, C., . . . Ihn, H. (2010). Basic fibroblast growth factor stimulates the proliferation of human dermal fibroblasts via the ERK1/2 and JNK pathways. *British Journal of Dermatology*, *162*(4), 717-723.

Malinda, K. M., Kleinman, H. K., Sidhu, G. S., Mani, H., Banaudha, K., Maheshwari, R. K., & Goldstein, A. L. (1999). Thymosin β4 accelerates wound healing. *Journal of Investigative Dermatology*, *113*(3), 364-368.

Masliíski, C., & Olczak, A. (1977). The role of histamine in wound healing I. The effect of high doses of histamine on collagen and glycosoaminoglycan content in wounds. *Agents and actions*, *7*(2), 219-224.

Matteini, P., Cicchi, R., Ratto, F., Kapsokalyvas, D., Rossi, F., de Angelis, M., . . . Pini, R. (2012). Thermal transitions of fibrillar collagen unveiled by second-harmonic generation microscopy of corneal stroma. *Biophysical journal*, *103*(6), 1179-1187.

Matteini, P., Rossi, F., Menabuoni, L., & Pini, R. (2007). Microscopic characterization of collagen modifications induced by low-temperature diode-laser welding of corneal tissue. *Lasers in Surgery and Medicine*, *39*(7), 597-604. https://doi.org/10.1002/lsm.20532

Matteini, P., Sbrana, F., Tiribilli, B., & Pini, R. (2009). Atomic force microscopy and transmission electron microscopy analyses of low-temperature laser welding of the cornea. *Lasers in Medical Science*, *24*(4), 667-671. https://doi.org/10.1007/s10103-008-0617-4

Menon, R., Krzyszczyk, P., & Berthiaume, F. (2017). Pro-resolution potency of resolvins D1, D2 and E1 on neutrophil migration and in dermal wound healing. *Nano Life*, *7*(01), 1750002.

Michaels, J., Churgin, S. S., Blechman, K. M., Greives, M. R., Aarabi, S., Galiano, R. D., & Gurtner, G. C. (2007). db/db mice exhibit severe wound-healing impairments compared with other murine diabetic strains in a silicone-splinted excisional wound model. *Wound repair and regeneration*, *15*(5), 665-670.

Mikołajczyk, T., & Wołowska-Czapnik, D. (2005). Multifunctional alginate fibres with anti-bacterial properties. *Fibres & Textiles in Eastern Europe*, *13*, 35-40.

Miles, C. A., & Burjanadze, T. V. (2001). Thermal stability of collagen fibers in ethylene glycol. *Biophysical Journal*, *80*(3), 1480-1486. https://doi.org/10.1016/S0006-3495(01)76120-6

Milewski, P., & Thomson, H. (1980). Is a fat stitch necessary? *Journal of British Surgery*, *67*(6), 393-394.

Ming-Che, W., Pins, G. D., & Silver, F. H. (1994). Collagen fibres with improved strength for the repair of soft tissue injuries. *Biomaterials*, *15*(7), 507-512. https://doi.org/10.1016/0142-9612(94)90016-7

Mushaben, M., Urie, R., Flake, T., Jaffe, M., Rege, K., & Heys, J. (2018). Spatiotemporal modeling of laser tissue soldering using photothermal nanocomposites. *Lasers in Surgery and Medicine*, *50*(2), 143-152. https://doi.org/10.1002/lsm.22746

Narayanan, A., Xu, Y., Dhinojwala, A., & Joy, A. (2020). Advances in Photoreactive Tissue Adhesives Derived from Natural Polymers. *ChemEngineering*, *4*(2), 32.

Navneeta, R., Jason, H., Marie-France, C., Charles, J. D., & Diego, M. (2007). Preparation of ready-to-use, storable and reconstituted type I collagen from rat tail tendon for tissue engineering applications. *Nature Protocols*, *1*(6), 2753. https://doi.org/10.1038/nprot.2006.430

Nikoobakht, B., & El-Sayed, M. A. (2003). Preparation and Growth Mechanism of Gold Nanorods (NRs) Using Seed-Mediated Growth Method. *Chemistry of Materials*, *15*(10), 1957-1962. https://doi.org/10.1021/cm020732l

Nordentoft, T., Rømer, J., & Sørensen, M. (2007). Sealing of gastrointestinal anastomoses with a fibrin glue-coated collagen patch: a safety study. *Journal of Investigative Surgery*, *20*(6), 363-369.

Numata, Y., Terui, T., Okuyama, R., Hirasawa, N., Sugiura, Y., Miyoshi, I., . . . Ohtsu, H. (2006). The accelerating effect of histamine on the cutaneous wound-healing process through the action of basic fibroblast growth factor. *Journal of Investigative Dermatology*, *126*(6), 1403-1409.

Ogunlade, O., Ho, J. O., Kalber, T. L., Hynds, R. E., Zhang, E., Janes, S. M., . . . Beard, P. (2019). Monitoring neovascularization and integration of decellularized human scaffolds using photoacoustic imaging. *Photoacoustics*, *13*, 76-84.

Pan, Y., Li, J., Zhang, Y., Wang, N., Liang, H., Liu, Y., . . . Gu, H. (2016). Slug-upregulated miR-221 promotes breast cancer progression through suppressing E-cadherin expression. *Scientific reports*, *6*(1), 1-14.

Panda, S., Connolly, M. P., Ramirez, M. G., & de Heredia, J. B. (2020). Costs Analysis of Fibrin Sealant for Prevention of Anastomotic Leakage in Lower Colorectal Surgery. *Risk management and healthcare policy*, *13*, 5.

Pastar, I., Stojadinovic, O., Yin, N. C., Ramirez, H., Nusbaum, A. G., Sawaya, A., . . . Tomic-Canic, M. (2014). Epithelialization in wound healing: a comprehensive review. *Advances in wound care*, *3*(7), 445-464.

Pasternak, B., Rehn, M., Andersen, L., Ågren, M. S., Heegaard, A.-M., Tengvall, P., & Aspenberg, P. (2008). Doxycycline-coated sutures improve mechanical strength of intestinal anastomoses. *International journal of colorectal disease*, *23*(3), 271-276.

Peiseler, M., & Kubes, P. (2019). More friend than foe: the emerging role of neutrophils in tissue repair. *The Journal of clinical investigation*, *129*(7), 2629-2639.

Petri, M., Stoffels, I., Jose, J., Leyh, J., Schulz, A., Dissemond, J., . . . Klode, J. (2016). Photoacoustic imaging of real-time oxygen changes in chronic leg ulcers after topical application of a haemoglobin spray: a pilot study. *Journal of wound care*, *25*(2), 87-91.

Pommergaard, H.-C., Achiam, M. P., & Rosenberg, J. (2012). External coating of colonic anastomoses: a systematic review. *International journal of colorectal disease*, *27*(10), 1247-1258.

Powers, J. G., Higham, C., Broussard, K., & Phillips, T. J. (2016). Wound healing and treating wounds: Chronic wound care and management. *Journal of the American Academy of Dermatology*, *74*(4), 607-625.

Ratner, D., Nelson, B., & Johnson, T. (1994). Basic suture materials and suturing techniques. Seminars in dermatology,

Ratto, F., Cavigli, L., Borri, C., Centi, S., Magni, G., Mazzoni, M., & Pini, R. (2019). Hybrid organosilicon/polyol phantom for photoacoustic imaging. *Biomedical optics express*, *10*(8), 3719-3730.

Rockwood, D. N., Preda, R. C., Yücel, T., Wang, X., Lovett, M. L., & Kaplan, D. L. (2011). Materials fabrication from Bombyx mori silk fibroin. *Nature protocols*, *6*(10), 1612.

Ruifrok, A. C., & Johnston, D. A. (2001). Quantification of histochemical staining by color deconvolution. *Analytical and quantitative cytology and histology*, *23*(4), 291-299.

Rønø, B., Engelholm, L. H., Lund, L. R., & Hald, A. (2013). Gender affects skin wound healing in plasminogen deficient mice. *PloS one*, *8*(3), e59942.

Sal Salcido, R. (2017). Healing by intention. In: LIPPINCOTT WILLIAMS & WILKINS TWO COMMERCE SQ, 2001 MARKET ST, PHILADELPHIA ….

Sangsanoh, P., & Supaphol, P. (2006). Stability improvement of electrospun chitosan nanofibrous membranes in neutral or weak basic aqueous solutions. *Biomacromolecules*, *7*(10), 2710-2714.

Schiff, A., Roy, S., Pignot, M., Ghosh, S., & Fegelman, E. (2017). Diagnosis and management of intraoperative colorectal anastomotic leaks: A global retrospective patient chart review study. *Surgery research and practice*, *2017*.

Schober, R., Ulrich, F., Sander, T., Durselen, H., & Hessel, S. (1986). Laser-induced alteration of collagen substructure allows microsurgical tissue welding. *Science*, *232*(4756), 1421-1422.

Schrock, T. R., Deveney, C. W., & Dunphy, J. E. (1973). Factor contributing to leakage of colonic anastomoses. *Annals of Surgery*, *177*(5), 513-518.

Sdralis, E., Tzaferai, A., Davakis, S., Syllaios, A., Kordzadeh, A., Lorenzi, B., & Charalabopoulos, A. (2020). Reinforcement of intrathoracic oesophago-gastric anastomosis with fibrin sealant (Tisseel®) in oesophagectomy for cancer: A prospective comparative study. *The American Journal of Surgery*, *219*(1), 123-128.

Selvig, K. A., Biagiotti, G. R., Leknes, K. N., & Wikesjö, U. M. (1998). Oral tissue reactions to suture materials. *International Journal of Periodontics & Restorative Dentistry*, *18*(5).

Sen, C. K., Gordillo, G. M., Roy, S., Kirsner, R., Lambert, L., Hunt, T. K., . . . Longaker, M. T. (2009). Human skin wounds: a major and snowballing threat to public health and the economy. *Wound repair and regeneration*, *17*(6), 763-771.

Sen, C. K., Khanna, S., Venojarvi, M., Trikha, P., Ellison, E. C., Hunt, T. K., & Roy, S. (2002). Copper-induced vascular endothelial growth factor expression and wound healing. *American Journal of Physiology-Heart and Circulatory Physiology*, *282*(5), H1821-H1827.

Shapiro, A. J., Dinsmore, R. C., & North Jr, J. H. (2001). Tensile strength of would closure with cyanoacrylate glue. *The American Surgeon*, *67*(11), 1113.

Shoulders, M. D., & Raines, R. T. (2009). Collagen structure and stability. *Annual review of biochemistry*, *78*, 929. https://doi.org/10.1146/annurev.biochem.77.032207.120833

Singer, A. J., Hollander, J. E., & Quinn, J. V. (1997). Evaluation and management of traumatic lacerations. *New England Journal of Medicine*, *337*(16), 1142-1148.

Singer, A. J., Quinn, J. V., & Hollander, J. E. (2008). The cyanoacrylate topical skin adhesives. *The American journal of emergency medicine*, *26*(4), 490-496.

Singh, J., Ray, A. R., Singhal, J., & Singh, H. (1990). Radiation-induced graft copolymerization of methacrylic acid on to poly (vinyl chloride) films and their thrombogenicity. *Biomaterials*, *11*(7), 473-476.

Skaugrud, Ø., Hagen, A., Borgersen, B., & Dornish, M. (1999). Biomedical and pharmaceutical applications of alginate and chitosan. *Biotechnology and genetic engineering reviews*, *16*(1), 23-40.

Slieker, J. C., Vakalopoulos, K. A., Komen, N. A., Jeekel, J., & Lange, J. F. (2013). Prevention of leakage by sealing colon anastomosis: experimental study in a mouse model. *journal of surgical research*, *184*(2), 819-824.

Snijders, H., Wouters, M., Van Leersum, N., Kolfschoten, N., Henneman, D., De Vries, A., . . . Bonsing, B. (2012). Meta-analysis of the risk for anastomotic leakage, the postoperative mortality caused by leakage in relation to the overall postoperative mortality. *European Journal of Surgical Oncology (EJSO)*, *38*(11), 1013-1019.

Soong, H. K., & Kenyon, K. R. (1984). Adverse reactions to virgin silk sutures in cataract surgery. *Ophthalmology*, *91*(5), 479-483.

Sriramoju, V., & Alfano, R. R. (2011). Management of heat in laser tissue welding using NIR cover window material. *Lasers in Surgery and Medicine*, *43*(10), 991-997. https://doi.org/10.1002/lsm.21143

Steinstraesser, L., Wehner, M., Trust, G., Sorkin, M., Bao, D., Hirsch, T., . . . Jacobsen, F. (2010). Laser-mediated fixation of collagen-based scaffolds to dermal wounds. *Lasers in Surgery and Medicine*, *42*(2), 141-149. https://doi.org/10.1002/lsm.20901

Sugiura, S., Oda, T., Izumida, Y., Aoyagi, Y., Satake, M., Ochiai, A., . . . Nakajima, M. (2005). Size control of calcium alginate beads containing living cells using micro-nozzle array. *Biomaterials*, *26*(16), 3327-3331.

Sun, N., Ning, B., Hansson, K. M., Bruce, A. C., Seaman, S. A., Zhang, C., . . . Wågberg, M. (2018). Modified VEGF-A mRNA induces sustained multifaceted microvascular response and accelerates diabetic wound healing. *Scientific reports*, *8*(1), 1-11.

Szekalska, M., Puciłowska, A., Szymańska, E., Ciosek, P., & Winnicka, K. (2016). Alginate: current use and future perspectives in pharmaceutical and biomedical applications. *International Journal of Polymer Science*, *2016*.

Taboada, G. M., Yang, K., Pereira, M. J., Liu, S. S., Hu, Y., Karp, J. M., . . . Lee, Y. (2020). Overcoming the translational barriers of tissue adhesives. *Nature Reviews Materials*, *5*(4), 310-329.

Tajirian, A. L., & Goldberg, D. J. (2010). A review of sutures and other skin closure materials. *Journal of Cosmetic and Laser Therapy*, *12*(6), 296-302.

Tan, W. H., & Takeuchi, S. (2007). Monodisperse alginate hydrogel microbeads for cell encapsulation. *Advanced materials*, *19*(18), 2696-2701.

Tenaud, I., Sainte-Marie, I., Jumbou, O., Litoux, P., & Dreno, B. (1999). In vitro modulation of keratinocyte wound healing integrins by zinc, copper and manganese. *The British journal of dermatology*, *140*(1), 26-34.

Topol, B. M., Lewis Jr, V. L., & Benveniste, K. (1981). The use of antihistamine to retard the growth of fibroblasts derived from human skin, scar, and keloid. *Plastic and reconstructive surgery*, *68*(2), 227-232.

Trautmann, A., Toksoy, A., Engelhardt, E., Bröcker, E. B., & Gillitzer, R. (2000). Mast cell involvement in normal human skin wound healing: expression of monocyte chemoattractant protein-1 is correlated with recruitment of mast cells which synthesize interleukin-4 in vivo. *The Journal of pathology*, *190*(1), 100-106.

Urie, R., Ghosh, D., Ridha, I., & Rege, K. (2018). Inorganic nanomaterials for soft tissue repair and regeneration. *Annual review of biomedical engineering*, *20*, 353-374.

Urie, R., Guo, C., Ghosh, D., Thelakkaden, M., Wong, V., Lee, J. K., . . . Rege, K. (2018a). Rapid Soft Tissue Approximation and Repair Using Laser-Activated Silk Nanosealants. *Advanced functional materials*, *28*(42), 1802874. https://doi.org/doi:10.1002/adfm.201802874

Urie, R., Guo, C., Ghosh, D., Thelakkaden, M., Wong, V., Lee, J. K., . . . Rege, K. (2018b). Rapid Soft Tissue Approximation and Repair Using Laser-Activated Silk Nanosealants. *Advanced Functional Materials*, *28*(42), 1802874.

Urie, R., McBride, M., Ghosh, D., Fattahi, A., Nitiyanandan, R., Popovich, J., . . . Rege, K. (2021). Antimicrobial laser-activated sealants for combating surgical site infections. *Biomaterials science*, *9*(10), 3791-3803.

Urie, R., Quraishi, S., Jaffe, M., & Rege, K. (2015). Gold Nanorod-Collagen Nanocomposites as Photothermal Nanosolders for Laser Welding of Ruptured Porcine Intestines. *ACS Biomaterials Science & Engineering*, *1*(9), 805-815. https://doi.org/10.1021/acsbiomaterials.5b00174

Urie, R., Quraishi, S., Jaffe, M., & Rege, K. (2015). Gold Nanorod-Collagen Nanocomposites as Photothermal Nanosolders for Laser Welding of Ruptured Porcine Intestines. *ACS Biomaterials Science and Engineering*, *1*(9), 805-815. https://doi.org/10.1021/acsbiomaterials.5b00174

Urie, R., & Rege, K. (2015). Nanoscale inorganic scaffolds as therapeutics and delivery vehicles. *Current Opinion in Chemical Engineering*, *7*, 120-128. https://doi.org/10.1016/j.coche.2014.12.004

Wallin, R. F., & Arscott, E. (1998). A practical guide to ISO 10993-5: Cytotoxicity. *Medical Device and Diagnostic Industry*, *20*, 96-98.

Wang, J., Witte, F., Xi, T., Zheng, Y., Yang, K., Yang, Y., . . . Li, W. (2015). Recommendation for modifying current cytotoxicity testing standards for biodegradable magnesium-based materials. *Acta biomaterialia*, *21*, 237-249.

Wang, Q., Zhang, N., Hu, X., Yang, J., & Du, Y. (2007). Alginate/polyethylene glycol blend fibers and their properties for drug controlled release. *Journal of biomedical materials research Part A*, *82*(1), 122-128.

Wang, X., Lv, F., Li, T., Han, Y., Yi, Z., Liu, M., . . . Wu, C. (2017). Electrospun micropatterned nanocomposites incorporated with Cu2S nanoflowers for skin tumor therapy and wound healing. *ACS nano*, *11*(11), 11337-11349.

Weber, M., Steinle, H., Golombek, S., Hann, L., Schlensak, C., Wendel, H. P., & Avci-Adali, M. (2018). Blood-Contacting Biomaterials: In vitro evaluation of the hemocompatibility. *Frontiers in Bioengineering and Biotechnology*, *6*.

White, R. A., Kopchok, G. E., Donayre, C. E., Peng, S. K., Fujitani, R. M., White, G. H., & Uitto, J. (1988). Mechanism of tissue fusion in argon laser-welded vein-artery anastomoses. *Lasers in surgery and medicine*, *8*(1), 83-89.

Wilgus, T. A., Matthies, A. M., Radek, K. A., Dovi, J. V., Burns, A. L., Shankar, R., & DiPietro, L. A. (2005). Novel function for vascular endothelial growth factor receptor-1 on epidermal keratinocytes. *The American journal of pathology*, *167*(5), 1257-1266.

Wulff, B. C., & Wilgus, T. A. (2013). Mast cell activity in the healing wound: more than meets the eye? *Experimental dermatology*, *22*(8), 507-510.

Xiao, J., Chen, S., Yi, J., Zhang, H. F., & Ameer, G. A. (2017). A Cooperative Copper Metal–Organic Framework-Hydrogel System Improves Wound Healing in Diabetes. *Advanced functional materials*, *27*(1), 1604872.

Xu, N., Yao, M., Farinelli, W., Hajjarian, Z., Wang, Y., Redmond, R. W., & Kochevar, I. E. (2015). Light-activated sealing of skin wounds. *Lasers in surgery and medicine*, *47*(1), 17-29.

Xu, X., Zhao, Y., Xue, X., Huo, S., Chen, F., Zou, G., & Liang, X.-j. (2014). Seedless synthesis of high aspect ratio gold nanorods with high yield. *J. Mater. Chem. A*, *2*(10), 3528-3535. https://doi.org/10.1039/c3ta13905k

Yaltirik, M., Dedeoglu, K., Bilgic, B., Koray, M., Ersev, H., Issever, H., . . . Soley, S. (2003). Comparison of four different suture materials in soft tissues of rats. *Oral diseases*, *9*(6), 284-286.

Yang, N., Wang, R., Rao, P., Yan, L., Zhang, W., Wang, J., & Chai, F. (2019). The Fabrication of Calcium Alginate Beads as a Green Sorbent for Selective Recovery of Cu (Ⅱ) from Metal Mixtures. *Crystals*, *9*(5), 255.

Yang, P., Yao, M., DeMartelaere, S. L., Redmond, R. W., & Kochevar, I. E. (2012). Light-activated sutureless closure of wounds in thin skin. *Lasers in surgery and medicine*, *44*(2), 163-167.

Yao, R., Tan, T., Tee, J. W., & Street, J. (2018). Prophylaxis of surgical site infection in adult spine surgery: A systematic review. *Journal of Clinical Neuroscience*, *52*, 5-25. https://doi.org/https://doi.org/10.1016/j.jocn.2018.03.023

Yaron, J. R., Zhang, L., Guo, Q., Awo, E. A., Burgin, M., Schutz, L. N., . . . Lowe, K. M. (2020). Recombinant myxoma virus-derived immune modulator M-T7 accelerates cutaneous wound healing and improves tissue remodeling. *Pharmaceutics*, *12*(11), 1003.

Yeboah, A., Cohen, R. I., Faulknor, R., Schloss, R., Yarmush, M. L., & Berthiaume, F. (2016). The development and characterization of SDF1α-elastin-like-peptide nanoparticles for wound healing. *Journal of Controlled Release*, *232*, 238-247.

Yeboah, A., Maguire, T., Schloss, R., Berthiaume, F., & Yarmush, M. L. (2017). Stromal cell-derived growth factor-1 alpha-elastin like peptide fusion protein promotes cell migration and

revascularization of experimental wounds in diabetic mice. *Advances in wound care*, *6*(1), 10-22.

Yeung, A. M., Faraj, L. A., Mcintosh, O. D., Dhillon, V. K., & Dua, H. S. (2016). Fibrin glue inhibits migration of ocular surface epithelial cells. *Eye*, *30*(10). https://doi.org/10.1038/eye.2016.127

Yilmaz, E., Blecher, R., Moisi, M., Ankush, C., O'Lynnger, T. M., Abdul-Jabbar, A., . . . Oskouian, R. J. (2018). Is There an Optimal Wound Closure Technique for Major Posterior Spine Surgery? A Systematic Review. *Global spine journal*, *8*(5), 535-544. https://doi.org/10.1177/2192568218774323

Younesi, M., Donmez, B. O., Islam, A., & Akkus, O. (2016). Heparinized collagen sutures for sustained delivery of PDGF-BB: delivery profile and effects on tendon-derived cells in-vitro. *Acta biomaterialia*, *41*, 100-109.

Zehtabchi, S., Tan, A., Yadav, K., Badawy, A., & Lucchesi, M. (2012). The impact of wound age on the infection rate of simple lacerations repaired in the emergency department. *Injury*, *43*(11), 1793-1798.

Zeugolis, D. I., Paul, R. G., & Attenburrow, G. (2008). Extruded collagen-polyethylene glycol fibers for tissue engineering applications. *Journal of Biomedical Materials Research Part B: Applied Biomaterials*, *85*(2), 343-352. https://doi.org/10.1002/jbm.b.30952

Zeugolis, D. I., & Raghunath, M. (2010). The physiological relevance of wet versus dry differential scanning calorimetry for biomaterial evaluation: a technical note. *Polym. Int.*, *59*(10), 1403-1407. https://doi.org/10.1002/pi.2882

Zhang, W., Chen, L., Chen, J., Wang, L., Gui, X., Ran, J., . . . Ji, J. (2017). Silk fibroin biomaterial shows safe and effective wound healing in animal models and a randomized controlled clinical trial. *Advanced healthcare materials*, *6*(10), 1700121.

Zhao, S., Li, L., Wang, H., Zhang, Y., Cheng, X., Zhou, N., . . . Zhang, C. (2015). Wound dressings composed of copper-doped borate bioactive glass microfibers stimulate angiogenesis and heal full-thickness skin defects in a rodent model. *Biomaterials*, *53*, 379-391.

Zhou, W., Tan, P., Chen, X., Cen, Y., You, C., Tan, L., . . . Tian, M. (2019). Berberine-incorporated shape memory fiber applied as a novel surgical suture. *Frontiers in Pharmacology*, *10*, 1506.

Zhou, Y. L., Yang, Q. Q., Yan, Y. Y., Zhang, L., Wang, Q. H., Ju, F., & Tang, J. B. (2019). Gene-Loaded Nanoparticle-Coated Sutures Provide Effective Gene Delivery to Enhance Tendon Healing. *Molecular Therapy*, *27*(9), 1534-1546.

APPENDIX A

SELECTED STEP-WISE PROTOCOLS

Protocol 1: Tissue processing for histology

Materials:

- Tissue cassettes (Slotted cassettes, Electron Microscopy Sciences, #700071-B)
- Tissue biopsy pads (Electron Microscopy Sciences, #62326)
- 10% neutral buffered formalin (Millipore Sigma, #HT501128)
- Forceps

Procedure:

1. Following euthanasia, excise skin samples with the intended wound area and surrounding tissue.
2. Transfer excised tissue to pre-labelled tissue cassette and place it over a biopsy pad. Quickly flatten the tissue to prevent folding during tissue fixing and processing steps.
3. Once the skin sample is flattened place another biopsy pad over the tissue, close the cassette, and transfer it to 10% neutral buffered formalin. Make sure the cassette is completely submerged in the formalin solution.
4. Continue to incubate tissue cassettes in formalin solution for at least 5-7 days at room temperature.
5. Following the formalin tissue fixation step, continue with the tissue processing steps as tabulated below with intermittent stirring of the solution jar every ~10 mins during the incubation steps.
6. Post completion of the tissue processing steps, tissue cassettes were stored at room temperature until further processing (embedding, sectioning, etc.)

Step	Solution	Incubation time (in mins)	Temperature (in °C)
1	1x PBS wash (to wash off excess formalin)	15	RT
2	1x PBS wash (to wash off excess formalin)	15	RT
3	40% Reagent Alcohol	45	RT
4	70% Reagent Alcohol	45	RT
5	70% Reagent Alcohol	60	RT
6	90% Reagent Alcohol	60	RT
7	90% Reagent Alcohol	60	RT
8	100% Reagent Alcohol	60	RT
9	100% Reagent Alcohol	60	RT
10	Xylene	60	RT
11	Xylene	60	RT
12	Xylene	60	RT
13	Xylene: Paraffin (1:1)	30	60 °C
14	Paraffin	45	60 °C
15	Paraffin	45	60 °C
16	Paraffin	45	60 °C